polymers

Review

Polymeric and Polymer-Functionalized Drug Delivery Vectors: From Molecular Architecture and Elasticity to Cellular Uptake

Thorsten Auth

Theoretical Physics of Living Matter, Institute for Advanced Simulation, Forschungszentrum Jülich, 52425 Jülich, Germany; t.auth@fz-juelich.de

Abstract

Polymers and polymer composites offer versatile possibilities for engineering the physico-chemical properties of materials on micro- and macroscopic scales. This review provides an overview of polymeric and polymer-decorated particles that can serve as drug-delivery vectors: linear polymers, star polymers, diblock-copolymer micelles, polymer-grafted nanoparticles, polymersomes, stealth liposomes, microgels, and biomolecular condensates. The physico-chemical interactions between the delivery vectors and biological cells range from chemical interactions on the molecular scale to deformation energies on the particle scale. The focus of this review is on the structure and elastic properties of these particles, as well as their circulation in blood and cellular uptake. Furthermore, the effects of polymer decoration in vivo (e.g., of glycosylated plasma membranes, cortical cytoskeletal networks, and naturally occurring condensates) on drug delivery are discussed.

Keywords: linear chains; star polymers; polymer-grafted nanoparticles; hairy nanoparticles; stealth liposomes; nanogels; microgels; biomolecular condensates; circulation times; cellular uptake; translocation; passive endocytosis; drug delivery

Academic Editor: Ranjit De

Received: 11 June 2025
Revised: 8 August 2025
Accepted: 12 August 2025
Published: 19 August 2025

Citation: Auth, T. Polymeric and Polymer-Functionalized Drug Delivery Vectors: From Molecular Architecture and Elasticity to Cellular Uptake. *Polymers* **2025**, *17*, 2243. https://doi.org/10.3390/polym17162243

1. Introduction

Polymeric materials are very versatile with regard to their elastic properties and surface functionalization. They can be readily produced at the laboratory scale, but the processes can be scaled up to the industrial level. Furthermore, polymers are routinely used to functionalize surfaces and equip them with the desired properties. Because of their versatility, polymer materials and composites are also important candidates for engineering vectors for targeted drug delivery. Synthetic polymeric molecules and particles for drug delivery can come in very different flavors: as linear chains, star polymers, diblock-copolymer micelles, polymer-grafted nanoparticles, polymer-decorated vesicles, polymersomes, nano- and microgels, and biomolecular condensates. Two further polymeric architectures used for drug delivery, capsules and dendrimers, are not discussed in the following but have been reviewed recently in specialized articles [1–3].

Each architecture of polymeric drug-delivery vectors comes with specific structural and elastic properties. For example, linear chains in a good solvent have, on average, an elongated shape and experience strong shape fluctuations. In contrast, stars with high functionalities, micelles, hairy particles with a high polymer density, and microgels can be thought of as spherical soft colloids (see Figure 1). Typical sizes of linear chains and star polymers for drug delivery are in the range of tens of nanometers, whereas biomolecular condensates, stealth liposomes, polymersomes, and microgels can reach sizes of a micrometer and more (see Table 1). Consequently, the interactions between particles with different architectures and biological cells can be fundamentally different. Whereas linear chains with suitable hydrophilic and hydrophobic properties translocate through lipid-bilayer membranes, soft-spherical colloids are likely to be wrapped by the membranes. Elasticity, a key parameter to characterize polymeric materials, has also been identified as a key parameter for the cellular uptake of particles [4–7].

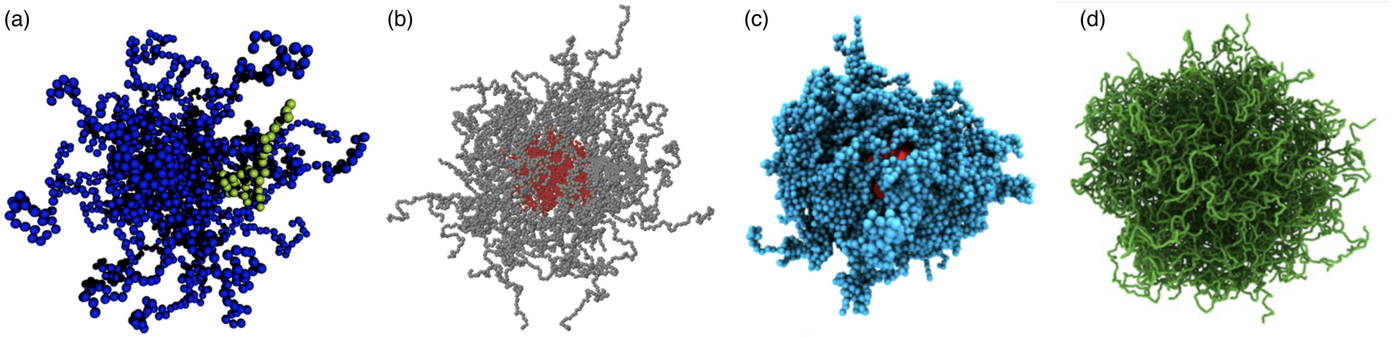

Figure 1. Simulation snapshots of polymeric particles. (**a**) Star polymer with $f = 35$ arms and $N_s = 50$ monomers (dark, blue beads) per chain and a linear chain with $N_c = 40$ monomers (bright, green beads) at a center-to-center distance of ten times the bead radius. Reprinted with permission from Ref. [8]. Copyright 2007 American Chemical Society. (**b**) Diblock-copolymer micelle. Reprinted with permission from Ref. [9]. Copyright 2006 American Chemical Society. (**c**) Polymer-grafted nanoparticle. Reprinted with permission from Ref. [10]. Copyright 2020 American Chemical Society. (**d**) Swollen microgel particle with a uniform crosslink distribution. Reprinted with permission from Ref. [11].

Table 1. Typical sizes of polymeric and polymer-functionalized particles.

Particle	Particle Size R_p	References
star polymers	3–40 nm	[12–15]
diblock-copolymer micelles	25–100 nm	[16,17]
biomolecular condensates	5 nm–5 µm	[18–20]
nanogels	10–100 nm	[21]
polymer-grafted nanoparticles	20–500 nm	[22–25]
polymersomes [1]	20 nm–200 µm	[26]
DNA and RNA origami particles	30–400 nm	[27–30]
stealth liposomes	200 nm–1 µm	[31]
microgels [1]	100 nm–100 µm	[21,32]

[1] Although polymersomes and microgels with sizes of the order of 100 µm are reported in the literature, for drug delivery by cellular uptake, only particles small enough to be taken up by biological cells are relevant.

For larger polymeric particles, an atomistic resolution is not the appropriate approach to capture the relevant physics and chemistry. Beyond the scale of single monomers, linear polymers are often described as (semi-)flexible chains with persistence length ℓ_p (see Table 2). The persistence length characterizes the decay of the orientational correlation function $\langle \mathbf{e}(s) \cdot \mathbf{e}(s + \Delta s)\rangle = \exp\left[-\Delta s/\ell_p\right]$ along the chain, where $\mathbf{e}$ is a tangential unit vector and s a coordinate along the contour. From a calculation point of view, also the model of freely hinged chains is convenient, where N straight rod-like segments with Kuhn length ℓ_K are linked to each other at vertices to form a polymer with total contour length $\ell_c = N\ell_K$. Both, persistence and Kuhn length, characterize the stiffness of linear polymer chains and are closely related, $\ell_K = 2\ell_p$ [33]. Whole-chain properties, such as the chain's root mean square end-to-end distance

$$R_e = \sqrt{\langle R_{e2e}^2 \rangle} = \ell_K N^{1/2} \tag{1}$$

with $R_{\mathrm{e2e}} = |\mathbf{r}_N - \mathbf{r}_0|$ the difference between the position vectors of the last and the first vertices, and the root mean square radius of gyration

$$R_{\mathrm{g}} = \sqrt{\left\langle R_{\mathrm{gyr}}^2 \right\rangle} = \frac{R_{\mathrm{e}}}{\sqrt{6}} \tag{2}$$

with $R_{\mathrm{gyr}}^2 = (1/N)\sum_{i=0}^{N}(\mathbf{r}_i - \langle \mathbf{r}_i \rangle)^2 = (1/(2N^2))\sum_{i=0}^{N}\sum_{j=0}^{N}(\mathbf{r}_i - \mathbf{r}_j)^2$, here for freely-hinged chains, fluctuate subject to thermal fluctuations of the polymer conformations. Synthetic polymers are often very flexible with persistence lengths in the nanometer range. Linear polymers with $N \gg 1$ act as entropic springs with a spring constant

$$k_{\mathrm{sp}} = \frac{3k_{\mathrm{B}}T}{R_{\mathrm{e}}^2} \tag{3}$$

and can exert an entropic pressure leading to an increase of the free energy, e.g.,

$$F_{\mathrm{conf}} = k_{\mathrm{B}}TN\left(\frac{\ell_{\mathrm{K}}}{d}\right)^{5/3} \tag{4}$$

if polymers in good solvent are confined to a tube of diameter d [34]. The bulk modulus of many polymeric delivery vectors consisting of flexible chains at low densities is therefore of the order of a few $k_{\mathrm{B}}T/(100\,\mathrm{nm})^3 \approx (10-100)$ Pa. Cytoskeletal filaments, on the contrary, have persistence lengths in the micrometer range and above, and thus form strong scaffolds for biological cells.

Table 2. Persistence lengths of polymers in water.

Polymer	Persistence Length ℓ_{p}	References
polyethylene oxide (PEO)	0.37–0.48 nm	[35,36]
polyethylene glycol (PEG)	0.38 nm	[36]
poly(N-isopropylacrylamide) (PNIPAM)	0.25–1.5 nm	[37,38]
single-stranded RNA and DNA	1–3 nm	[39,40]
spectrin tetramers	7.5 nm	[41]
double-stranded RNA and DNA [1]	50–65 nm	[42,43]
collagen	14–180 nm	[44]
intermediate filaments	0.5–2 µm	[45]
filamentous actin	17.7 µm	[46]
microtubules [2]	80–5000 µm	[47]

[1] Persistence length measured under physiological conditions. [2] Microtubules show a length-dependent persistence length [47].

Lipid-bilayer membranes, often supported by a cortical cytoskeleton, are the barriers and communication interfaces that separate the interior of biological cells from their environment. Thus, understanding the interaction of elastic particles with lipid-bilayer membranes is crucial for designing drug-delivery vectors. Using polymeric materials and polymer composites, not only can the molecular architectures, sizes, shapes, and elasticities be conveniently engineered, but also the molecular properties such as hydrophobicity/hydrophilicity, electrical charge, and surface functionalization with ligands. For example, the hydrophobic–hydrophilic sequence of their monomers affects the interaction of polymers with the hydrophilic headgroups and the hydrophobic tails of the lipids in bilayers. Additionally, a surface functionalization with polymers that contain charged or zwitterionic groups can significantly alter the interaction of delivery vectors with lipid-bilayer membranes (e.g., positively charged monomers are attracted to typically negatively charged cell plasma membranes [48,49]). Whereas hydrophobic and electrostatic interactions can mediate attraction between polymers and lipids, the steric interaction between polymer-functionalized surfaces induces repulsion [50–52]. The molecular properties of polymeric and polymer-functionalized delivery vectors can also be used to control the attachment of a protein corona when they are exposed to biological fluids. Controlling the formation of a corona is key for engineering the interactions of the vectors with lipids, proteins, and ligands in the plasma membranes of cells [53,54].

Polymers sensitive to external stimuli, such as temperature, pH, and light, may undergo externally triggered transitions that can be exploited for both drug loading and release. For example, polymers that change their solubility depending on the pH value of the buffer may disrupt lysosomes upon acidification and deliver their cargo to the cytosol [55]. Polymers with protonatable groups may promote endosomal escape via a proton sponge effect [56].

Linear polymers deliver drugs across plasma membranes when their design balances key physicochemical attributes. For example, a moderate cationic charge density facilitates membrane binding and cellular uptake when distributed evenly along the polymer chain [57]. However, depending on the number and arrangement of cations, positively charged polymers can also induce cytotoxicity [58,59]. Hydrophobic modifications have been found to enhance interactions with lipid bilayers and allow polymers to translocate through membranes [60–63]. However, hydrophobic polymers can lead to pore formation in bilayers and may thus induce cytotoxicity [64]. Therefore, effective drug delivery by linear polymers relies on molecular fine-tuning of the (i) molecular weight, (ii) backbone persistence length, (iii) hydrophobic modifications, and (iv) charges.

Star polymers with optimized physico-chemical properties can cross plasma membranes effectively; multifunctional star polymers are delivered to cells in vitro in less than 15 min [65]. Star polymers have been successfully applied for the non-viral delivery siRNA that forms a complex with the arms of the star [66,67]. Furthermore, star polymers are taken up using dynamin-dependent clathrin-mediated endocytosis by cancerous cells [68]. Star polymers can also be used for retarded drug delivery: nanostars that accumulate in endosomes of spinal neurons have been shown to release a drug against pain over a period of 24 h [69].

Diblock-copolymer micelles can incorporate hydrophilic cargo, such as siRNA, in their outer shells [70], and hydrophobic drugs, such as doxorubicin, in their cores [71]; pH sensitivity can help to release the drugs [72]. At higher concentrations, multi-micellar aggregates may co-exist with single micelles. Single micelles and aggregates can interact differently with biological cells because of their size difference [73–75]. For diblock-copolymer micelles, tuning the molecular architecture has a two-fold role: optimizing and targeting cellular uptake and drug loading. An appropriately tuned hydrophilic–hydrophobic balance and suitable lengths of the hydrophobic and hydrophilic blocks are key from the point of view of drug loading.

Polymer-grafted (“hairy”) nanoparticles (PGNs) are particles that are decorated with densely grafted linear polymers. This includes particles with low-functionality stars self-assembled around cargo, similar to the self-assembly of diblock-copolymer micelles [71,72]. A polymer coat can add surface functionalization and drug storage to magnetic nanoparticles [76], and can equip mesoporous silica nanoparticles with ultrasound-responsive drug-release properties [77]. Furthermore, thanks to the particle core, polymer-grafted nanoparticles enable us to synthesise delivery vectors with a wide range of sizes. PGNs can be engineered with small sizes of tens of nanometers suitable for clathrin-mediated endocytosis [78], but also with sizes of several micrometers suitable for phagocytic uptake [79,80]. Particles functionalized with polymers can show prolonged circulation times in the blood compared with bare particles [81]. For PEG-coated gold nanoparticles, it has been shown that an increased molecular weight of the PEG can increase the circulation time by an order of magnitude [82].

Polymersomes often consist of diblock-copolymer bilayers, analogously to liposomes consisting of lipid bilayers [83]. However, their membranes are usually significantly thicker and thus more rigid and stable than their lipid-bilayer counterparts. Therefore, conventional polymersomes have a low permeability of their membranes [84]. More recently, advanced polymersomes with membrane thicknesses similar to those of liposomes show higher permeabilities [85]; this also applies to polyion complex vesicles that consist of an electrostatically complexed shell of charged polyelectrolytes [86]. In conventional polymersomes, hydrophilic drugs can be incorporated in the aqueous core [87], and hydrophobic drugs in the hydrophobic layer of the membrane [88]. Recently, thermoplasmonic polymersomes containing small gold nanoparticles have been shown to induce death of cancer cells in vitro through collective heating [89].

Stealth liposomes are liposomes coated with polymers that lead to prolonged circulation times and reduced macrophage uptake. The liposomes are traditionally modified using PEG. In addition to the steric repulsion, the polymer layer can also lead to measurable differences in surface charge [90] and hydrophilicity [91]. An increased molecular weight of the PEG molecules used for surface modification can increase the hydrodynamic thickness of the polymer coat of the liposomes and decrease their zeta potential [92]. Furthermore, a PEG coating of liposomes can lead to a decreased drug-release rate [93].

Nano- and microgels have emerged as versatile materials for biological applications, ranging from drug delivery to tissue engineering [94]. Their physicochemical properties are tunable with respect to a wide range of materials, sizes, shapes, and elastic moduli. Nano- and microgels have the ability to encapsulate both hydrophilic and hydrophobic drugs [95,96]. Microgels can be designed to interact with peptides and proteins, making them suitable for macromolecular drug delivery [97]. Injectable microgel–hydrogel composites have shown prolonged small-molecule drug release [93]. The 3D crosslinked polymer networks of the gels allow us to engineer microgels with homogeneous elasticity, but also with core-shell or hollow architectures [98]. Polymeric gels are also used as cores for lipid nanoparticles to modify the liposome elasticity [99–101]. Recently, ultralow-crosslinked (ULC) microgels have received increased attention due to their special elastic and flow properties. When solubilized in a droplet that dries at room temperature, swollen ULC microgels do not show a coffee-ring effect [102], and in flow they behave as hard or soft objects depending on their concentration [103]. ULC microgels can pass through capillaries smaller than their diameter [104], can be incorporated within a fibrin network without restricting cell motility [105], and have been shown to collapse on a fibrin network mimicking behavior known from platelets in blood clotting in vivo [106].

Biomolecular condensates, also referred to as coacervates, can accommodate small molecules, proteins, nucleic acids, enzymes, and substrates. Synthetic condensates, inspired by their in vivo counterparts, have thus been recognized as drug reservoirs and developed to serve as drug-delivery vectors. They can deliver both hydrophilic drugs, such as antibodies, which individually do not easily cross the hydrophobic core of the cell membrane [107], and hydrophobic drugs that are not easily solubilized in water [108]. Condensation occurs below an upper or above a lower critical solution temperature (UCST, LCST) [109,110]; condensate sizes range from tens of nanometers to hundreds of micrometers and can be tuned by, for example, temperature [111] and pH [70]. The stimulus sensitivity of biomolecular condensates can be exploited, e.g., for endosomal escape. Cellular uptake processes for biomolecular condensates include active cellular uptake by macropinocytosis and phagocytosis [112], as well as direct cytosolic delivery [113–115], such that condensates used for drug delivery as large as $\approx 1\ \mu\text{m}$ can be taken up by cells in the presence of endocytosis inhibitors [112,114]. The properties of biomolecular condensates can be engineered by polymer concentration and chain length, but also by the chemical properties of the polymers and the cargo. Condensates can be coated with lipids to modify their interactions with lipid-bilayer membranes [107,116].

In the following, the structural and elastic properties, circulation times in the blood, and cellular uptake of polymeric and polymer-functionalized drug-delivery vectors will be discussed in more detail. Three main cellular uptake mechanisms, translocation, passive endocytosis, and active uptake, will be reviewed. Finally, a summary and an outlook will be provided.

2. Structural and Elastic Characterization

The architecture of polymeric and polymer-functionalized materials depends both on the type of polymeric material and its molecular architecture. Here, the long-standing history of polymer research offers a range of modeling approaches, spanning from Flory theory and blob models to more recent analytical methods. The models for structure and deformation energy presented below allow us to characterize the deformability of the polymeric particles, which is key to calculating their elastic deformations upon interaction with the plasma membranes of cells and for constructing models for cellular uptake.

2.1. Linear Polymers

Linear polymers are the basic building blocks of many polymeric materials (see Figure 2). On the atomic scale, the detailed chemical structure best defines the interactions within and between molecules; on the scale of the entire molecule, persistence length (discussed earlier) and solvent quality are often the appropriate concepts to characterize the properties of linear chains. If chains with contour lengths much larger than the persistence length are considered, three states can be distinguished depending on the solvent quality: (i) in bad solvents, the polymer collapses and forms a compact globule; (ii) in so-called "theta solvent," the polymer behaves like an ideal random walk; and (iii) in good solvents, the polymer swells beyond the ideal random walk and typically has an elongated shape [117]. In bad solvents, the monomers are densely packed, and the interactions are dominated by the attractive and the excluded-volume interactions between the monomers. Consequently, the size of the polymer globule scales as $N^{1/3}$ with the number of monomers. So-called theta solvents are defined such that the properties of linear chains are described by Equations (1)–(3). In good solvents, the root mean square end-to-end distance of linear chains has been shown to scale as

$$R_\mathrm{e} \propto N^{\nu}\,, \tag{5}$$

where ν is the Flory exponent, which has been estimated analytically to be $\nu = 3/5$ and numerically to be $\nu = 0.588$ [118].

Whereas many properties of ideal random walks for linear polymers in theta solvents can be accurately calculated analytically, self-avoiding linear chains are often studied using computer simulations (see Figure 2a). One simulation model is the freely hinged chain with Gaussian bond-length distribution and Lennard–Jones beads at the vertices that ensure self-avoidance. If the ratio of the bead size σ to the equilibrium bond length ℓ_K is carefully chosen, it allows the formation of a liquid state at low temperatures [119,120]. For potential depth ϵ, the attractive interaction potential between the beads leads to a collapsed liquid-like globular conformation of the polymer chain for temperatures $T \lesssim 2\epsilon/k_\mathrm{B}$ and a to random coil for $T \gtrsim 2\epsilon/k_\mathrm{B}$. At the transition, the radius of gyration R_g increases sharply, and the specific heat, characterized by the mean-squared deviation of the total energy from its average $\tilde{C} = \left[\langle E_\mathrm{int}^2\rangle - \langle E_\mathrm{int}\rangle^2\right]/(N^2\epsilon^2)$, shows a peak (see Figure 2d).

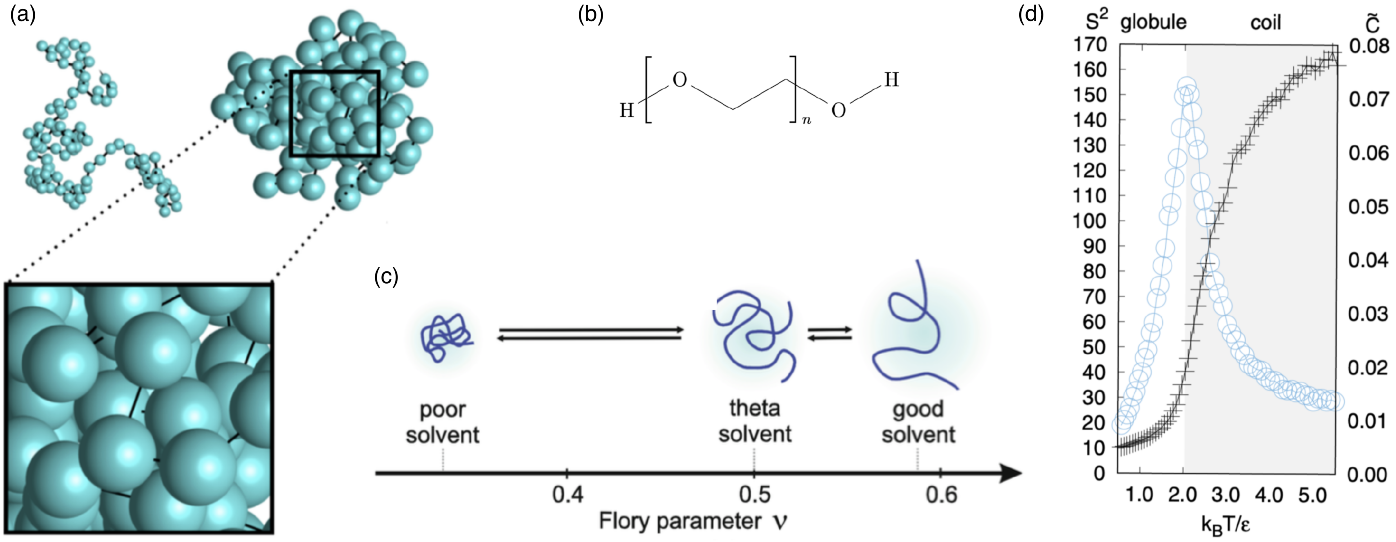

Figure 2. Linear polymers. (**a**) Typical configurations of a linear chain with $N = 102$ monomers in the coil state and a liquid-like globular state. Reprinted with permission from Ref. [119]. Copyright 2017 by the American Physical Society. (**b**) Chemical structure of polyethylene glycol (PEG). (**c**) Shapes and Flory parameters ν of polymer chains in different solvent qualities. The three dotted lines denote the theoretical values of ν for different solvent qualities. Reproduced from Ref. [121] with permission from Springer Nature. (**d**) Reduced mean square radius of gyration $S^2 = (R_g/\ell_K)^2$ (plus symbols in the left scale) and mean-squared deviation of the total energy from its average $\tilde{C}$ (proportional to the specific heat; circles in the right scale) as functions of the reduced temperature $k_B T/\epsilon$, determined from the Monte Carlo simulations of Gaussian chains for $N = 102$. Reprinted with permission from Ref. [119]. Copyright 2017 by the American Physical Society.

2.2. Star Polymers

Star polymers consist of f linear chains attached to each other at their ends to form a star, where f is the functionality of the star. Stars with low functionality are dominated by the nature of the linear chains, which is also seen by the smeared-out scattering intensity (see Figure 3a), while stars with high functionality resemble spherical soft colloids. In the liquid drop model for star polymers, the arms are considered fluid because they can readily interchange their positions. The free energy of the star polymer reads [122]

$$F = \chi_T^{-1}\left(V - V_0 - V_0 \ln \frac{V}{V_0}\right) + \gamma_F A_F + \frac{1}{2}\gamma_C A_C\,, \tag{6}$$

with χ_T being the isothermal compressibility at the reference volume V_0 at which the pressure in the drop vanishes, V the actual drop volume, γ_F the tension of the drop–solvent interface, and A_F the drop–solvent interface area. For star-polymer aggregates, the terms with interfacial tension $\gamma_C \neq \gamma_F$ at the contact zones, the contact area A_C between stars, and the accordingly reduced drop–solvent interface area A_F are taken into account for aggregate formation. For calculating the total contact area in star-polymer aggregates, the interfacial area is the area shared by two drops and should be considered only once.

Because the tension of the drop–solvent interface compresses a free star polymer, its equilibrium volume $V_* < V_0$ is smaller than the reference volume; the resting volume $V_* < V_0$ is found by minimizing the energy of an isolated drop. To the lowest order, the relative volume decrease of free stars is given by the product $\Pi_L \chi_T$, where

$$\Pi_L = \frac{2\gamma_F}{R_0} \tag{7}$$

is the osmotic pressure for the resting drop radius $R_* < R_0 = (3V_0/4\pi)^{1/3}$. The compressibility χ_T is determined via the Egelstaff–Widom length

$$\Psi = \frac{2\gamma_F \chi_T}{R_0}, \tag{8}$$

below which molecular physics is required to model liquids and above which macroscopic laws can be employed [123]. At high f, the liquid drops are incompressible and their equilibrium volumes are similar to the resting volume, $V_* \approx V_0$, which corresponds to $\Psi \to 0$. If the equilibrium volume V_* is much smaller than the resting volume V_0, then $\Psi \gg 1$. For deformations of the star smaller than the Egelstaff–Widom length, the liquid drop model allows predicting the lateral extension and the deformation energy upon compresssion between two parallel walls (see Figure 3b); the deformation energy change is orders of magnitude larger than the thermal energy $k_B T$.

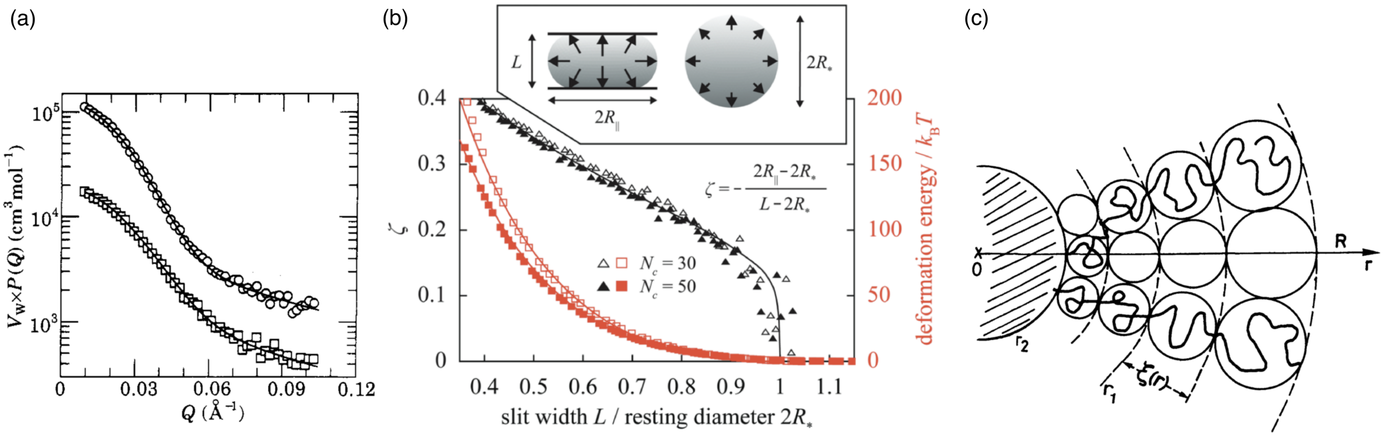

Figure 3. Star polymers. (**a**) Form factors and corresponding fits (solid lines) of the 8-arm (squares) and 18-arm (circles) polyisoprene stars (8-arm data are multiplied by a factor of 0.3 for visibility). Figure reproduced from Ref. [124]. Published under licence by IOP Publishing Ltd. (**b**) Liquid-drop model. Reduced central lateral extension ζ of a diametrically compressed spherical polymer brush with $f = 60$ arms containing $N_c = 30$ and 50 monomers plotted against slit width L (black datapoints/curve). The datapoints are obtained using molecular dynamics simulations, and the curve is the liquid drop model fit for the reduced Egelstaff–Widom length $\Psi = 0.6$ (see Equation (8)). The deformation energies for these two cases, together with the fits (red datapoints/curves), are also shown. The inset illustrates the diametral-compression geometry, with arrows representing hydrostatic pressure, and contains the definition of ζ. Figure reproduced from Ref. [122]. CC BY-NC 3.0. (**c**) A representation of the Daoud–Cotton model: every branch is made of a succession of blobs with a size ξ increasing from the centre of the star to the outside. From outside to inside, r_1 indicates the transition between the swollen and the unswollen region, and r_2 the transition between the unswollen region and the core. The terms swollen, unswollen, and core refer to regions with increasing monomer concentration. Figure reprinted from Ref. [125].

Star polymers can alternatively be modeled using a blob model [125] (see Figure 3c). Each arm of the star is subdivided into blobs with energy $\approx k_B T$ each, whose sizes are determined by the sterical hindrance by monomers from the other arms. Therefore, the blob diameter $\xi(r) \propto r f^{-1/2}$ increases linearly with the distance r from the center of the star. The confinement of the arm motion requires smaller blobs near the center and larger blobs towards the surface of the star. The total energy is the sum of the elastic energy

$$F_{el} \propto \frac{R_s^2}{N_f f^{1/2} \ell_K^2} k_B T, \tag{9}$$

and the interaction energy

$$F_{\text{int}} \propto (N_{\text{f}} f^{1/2})^2 \frac{v f^{-1/2}}{R_{\text{s}}^3} k_{\text{B}} T \tag{10}$$

over all arms of the star, $F_{\text{star}} = \sum_{i=1}^{f} (F_{\text{el}} + F_{\text{int}})$. Here, R_{s} is the radius of the star polymer, N_{f} the number of segments per arm, and v is the excluded volume associated with a segment.

2.3. Polymer-Grafted Nanoparticles

Polymer-grafted nanoparticles (PGNs) are spherical hard particles decorated with a dense layer of linear, end-grafted polymer chains (see Figure 4a). In melts, the two-layer model assumes that polymeric chains of neighbouring polymer-grafted nanoparticles interpenetrate in an outer layer of thickness h_{inter} and are expelled by the chains of the grafted nanoparticle in an inner layer of thickness h_{dry} (see Figure 4b,c). For calculating the interaction energy between two PGNs, the analytical model developed to calculate h_{inter} and h_{dry} in polymer melts agrees well with the computer simulations. The model may also be applied to estimate the deformation energy for single PGNs in solution [10], although in this case a more rigorous approach is the blob model for a brush on a hard core similar to the model discussed for star polymers. In the two-layer model, the height of the polymer brush is

$$h = \left(R_{\text{core}}^3 + \frac{3ZN_{\text{c}}}{4\pi\rho} \right)^{1/3} - R_{\text{core}} \tag{11}$$

for a core radius R_{core}, grafting density ρ_{g} and number $Z = 4\pi R_{\text{c}}^2 \rho_{\text{g}}$, and the segment volume number density ρ. This leads to the chain extension free energy

$$E_{\text{ext}} = \frac{3k_{\text{B}}Th^2}{2N_{\text{c}}\ell_{\text{K}}^2} = \frac{3k_{\text{B}}T}{2N_{\text{c}}\ell_{\text{K}}^2} \left[\left(R_{\text{core}}^3 + \frac{3ZN_{\text{c}}}{4\pi\rho} \right)^{1/3} - R_{\text{core}} \right]^2 . \tag{12}$$

The energy simplifies in the limit of a large core to the energy

$$E_{\text{ext}}^{\text{pln}} \approx \frac{3k_{\text{B}}T}{2} \left(\frac{Z}{4\pi\rho R_{\text{core}}^2 \ell_{\text{K}}} \right)^2 N \tag{13}$$

for a brush anchored to a planar substrate, and in the 'star-polymer' limit of a small core to

$$E_{\text{ext}}^{\text{sph}} \approx \frac{3k_{\text{B}}T}{2} \left(\frac{3Z}{4\pi\rho\ell_{\text{K}}^3} \right)^{2/3} N^{-1/3} . \tag{14}$$

2.4. Polymersomes and Stealth Liposomes

Polymersomes and stealth liposomes are built using polymer-decorated membranes. Polymer functionalization of membranes is a common motif both in vivo and for synthetic drug-delivery vectors, used to regulate the interaction with their environments (see Figure 5). Prominent examples are chondrocytes that produce a thick coat of hyaluronan [126], and polymer-coated stealth liposomes with improved circulation times in blood flow [127]. At sparse coverage, the linear polymers end-grafted to membranes assume mushroom shapes, which act as spacers that induce steric repulsion [128] and locally deform the membranes [129–132]. Because of the entropic repulsion between the polymer chains and the membranes, despite being in the mushroom regime, polymer-decorated membranes are stiffer than bare membranes [133–136]. However, for drug-delivery applications, a dense polymer coat is more effective to prevent a vector from interacting with other surfaces than sparsely distributed polymer mushrooms. Beyond stealth liposomes, many conventional polymersomes can be rationalized as formed by a polymer-brush-coated elastic surface [137], although some recent polymersomes, and also dendrimersomes, have thin membranes similar to lipid bilayers [85,138].

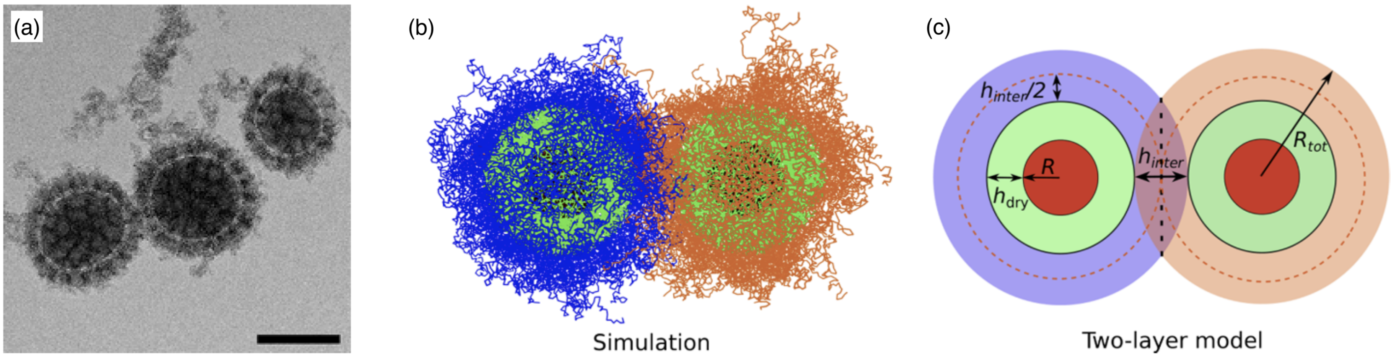

Figure 4. Polymer-grafted nanoparticles. (**a**) Cryo-electron micrograph of mixed poly(acrylic acid)/polystyrene brush-grafted silica nanoparticles in water. The scale bar corresponds to 100 nm. Reprinted with permission from Ref. [22]. Copyright 2015 American Chemical Society. (**b**,**c**) Simulation snapshot and schematic representation of the two-layer model. Indicated are the nanoparticle radius R, the total radius of the polymer-grafted nanoparticle R_{tot}, and the thicknesses of the dry and interpenetration layers, h_{dry} and h_{inter}, respectively. Reprinted with permission from Ref. [10]. Copyright 2020 American Chemical Society.

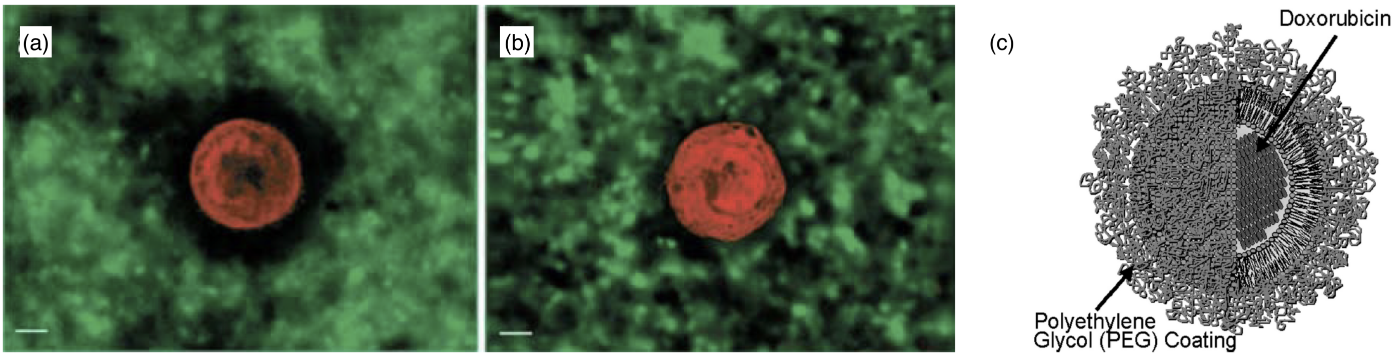

Figure 5. Polymer-decorated membranes. 3D reconstruction of the pericellular hyaluronan coat by particle exclusion assay. (**a**,**b**) Fluorescence micrographs of rhodamine-labeled chondrocytes immersed in a medium containing fluorescein isothiocyanate (FITC)-labeled silica beads. Cells were allowed to adhere to glass coverslips for 25 min before fixation and labeled with tetramethyl rhodamine isothiocyanate (red). They were then incubated with FITC-labeled 0.4 µm silica beads (green). Micrographs were taken with a digital microscope (DeltaVision) able to generate 3D images by image reconstruction from a series of z-sections at 0.5 µm resolution. The excluded volume is dark. Untreated cells have a 5 to 6 µm wide excluded zone around them (**a**), whereas beads reach up to the surface of hyaluronidase-treated cells (**b**). The scale bars correspond to 5 µm. Reprinted from Ref. [126], with permission from the Biophysical Society. (**c**) Pegylated liposomal doxorubicin. Reprinted from Ref. [127], Copyright 2004, with permission from Elsevier.

The steric repulsion due to the polymer coat of stealth liposomes and polymersomes may be modeled similarly to PGNs. The effective curvature-elastic properties of polymer-decorated membranes can be rationalized using a continuum-membrane model [139],

$$\mathcal{E}_{\text{def}} = \int dS \left[2\kappa (H - c_0)^2 + \bar{\kappa} K \right] , \tag{15}$$

with the integral calculated over the total membrane area S. Here, the membrane shape in each point is described by the mean curvature H and the Gaussian curvature K. The curvature-elastic parameters describe the membrane's material properties, with κ the bending rigidity, c_0 the spontaneous curvature, and $\bar{\kappa}$ the Gaussian saddle-splay modulus. The effective curvature-elastic constants of polymer-decorated membranes can be considered through a modification of their values for bare membranes $\kappa_{\text{eff}} = \kappa + \Delta\kappa$, $c_{0,\text{eff}} = c_0 + \Delta c_0$, and $\bar{\kappa}_{\text{eff}} = \bar{\kappa} + \Delta\bar{\kappa}$. For sparse polymer decoration, in the mushroom regime [133–136],

$$\frac{\Delta\kappa}{k_{\text{B}}T} = a_\kappa \sigma_{\text{p}} R_{\text{e}}^2 \qquad \frac{\kappa_{\text{eff}}}{k_{\text{B}}T}\Delta c_0 = a_{\text{sp}} \sigma_{\text{p}} R_{\text{e}} \qquad \frac{\Delta\bar{\kappa}}{k_{\text{B}}T} = \bar{a}_\kappa \sigma_{\text{p}} R_{\text{e}}^2 \tag{16}$$

for surface density σ_{p} of end-grafted linear, ideal polymer chains, $a_\kappa = 0.21$, $a_{\text{sp}} = 0.18$, and $\bar{a}_\kappa = -0.17$. In the brush regime, the curvature-elastic constants of polymer-decorated membranes are dominated by the polymer brush [136],

$$\begin{aligned} \frac{\Delta\kappa}{k_{\text{B}}T} &= \frac{\nu+2}{12\nu^2} R_{\text{e}}^6 \ell_{\text{K}}^{3\nu-6} \sigma_{\text{p}}^{3\nu/2} \\ \frac{\kappa_{\text{eff}}}{k_{\text{B}}T}\Delta c_0 &= \frac{1}{8\nu} R_{\text{e}}^4 \ell_{\text{K}}^{2/\nu-4} \sigma_{\text{p}}^{(2+\nu)/(2\nu)} \\ \frac{\Delta\bar{\kappa}}{k_{\text{B}}T} &= -\frac{1}{6\nu} R_{\text{e}}^6 \ell_{\text{K}}^{3\nu-6} \sigma_{\text{p}}^{3\nu/2}, \end{aligned} \tag{17}$$

with $\nu = 3/5$.

2.5. Nano- and Microgels

Nano- and microgels are polymeric particles with a 3D network whose architecture can be controlled during synthesis. The gels have fixed connections between their building blocks and thus a finite shear modulus. Many microgels are stimuli-responsive microparticles that swell and collapse depending on the temperature and/or pH [140,141], which considerably changes both their sizes and elastic properties (see Figures 6 and 7). If the temperature of a PNIPAM microgel is increased above the volume phase transition temperature (VPTT) ≈ 34 °C of the microgel, which for PNIPAM is similar to the lower critical solution temperature (LCST) ≈ 32 °C of the linear polymers, the microgels collapse due to the removal of the hydration layer surrounding the polymer chains and the formation of polymer–polymer contacts. Typical swelling ratios for PNIPAM are between 2 and 4, depending on the type of the crosslinkers [142]. Using scattering experiments and computer simulations, the fuzzy sphere model with a radially symmetrical density [140,143–145]

$$\frac{\rho(r)}{\rho_0} = \begin{cases} 1 & \text{if } r < R_{\text{c}} \\ 1 - \frac{(r-R'+2\sigma_{\text{surf}})^2}{8\sigma_{\text{surf}}^2} & \text{if } R_{\text{c}} \le r < R' \\ \frac{(R'-r+2\sigma_{\text{surf}})^2}{8\sigma_{\text{surf}}^2} & \text{if } R' \le r < R'' \\ 0 & \text{if } r \ge R'' \end{cases} \tag{18}$$

has been developed, which is capable of describing the normalized radial polymer density profile of stimuli-sensitive microgels at various temperatures. Here, ρ_0 is the polymer density in the inner core, and the smearing parameter σ_{surf} corresponds to about half the thickness of the fuzzy shell; $R_{\text{c}} = R' - 2\sigma_{\text{surf}}$ is the radius of the inner sphere of the microgel with a constant monomer density, R' is usually referred to as the core radius, and $R'' = R' + 2\sigma_{\text{surf}}$ is the total radius including the fuzzy shell.

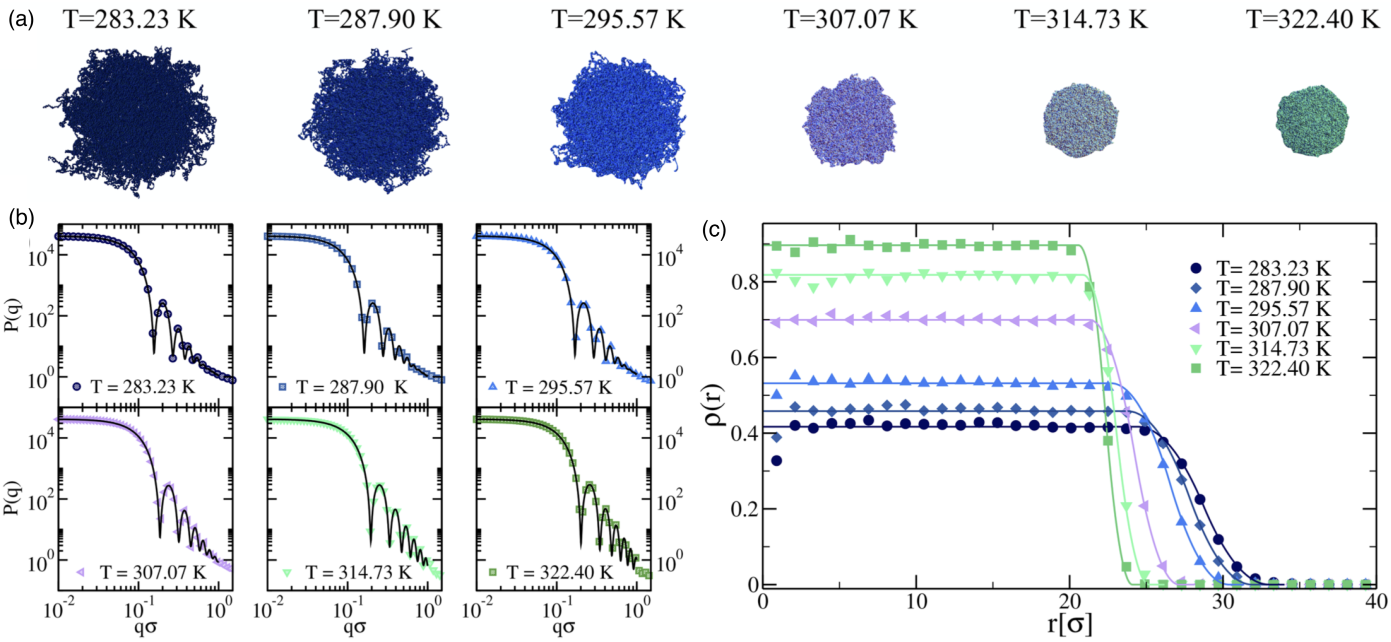

Figure 6. Microgel collapse: in silico modeling and scattering experiments. (**a**) Snapshots of a microgel particle, consisting of crosslinked linear chains with beads that interact using the Weeks–Chandler–Andersen (WCA) potential for 'bead size' σ, exhibiting the typical volume phase transition from swollen to compact. (**b**) Numerical form factors, averaged over four different realizations, for microgels with $N \approx 41{,}000$ monomers and $c = 3.2\%$ of crosslinkers generated in a sphere of radius $Z = 30\sigma$ (symbols) for various solvent qualities (corresponding to temperatures). Solid lines are fits of the curves using the fuzzy sphere model of Equation (18). (**c**) Averaged density profiles obtained from molecular dynamics (MD) simulations of a microgel with $N \approx 41{,}000$, $c = 3.2\%$, and $Z = 30\sigma$ (symbols) and from the fit of the form factors using the fuzzy sphere model (solid lines). Reprinted with permission from Ref. [140].

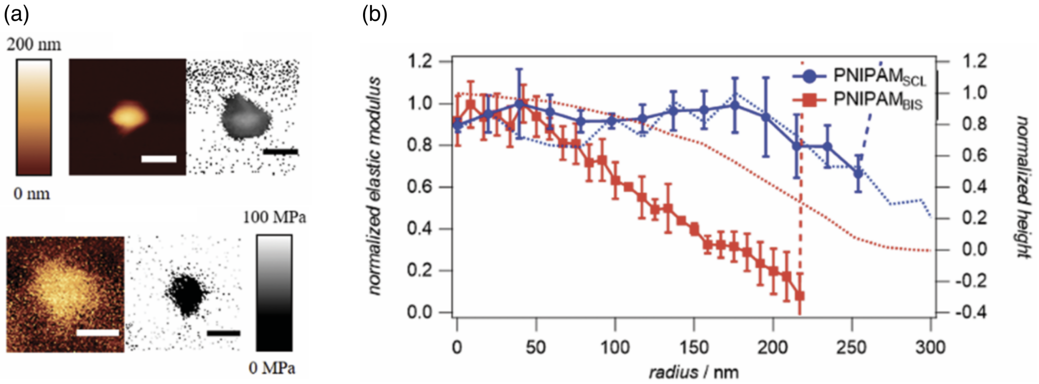

Figure 7. The elastic moduli of deposited PNIPAM$_{BIS}$ microgels that are crosslinked using N,N′-methylenebis(acrylamide) (BIS) and of PNIPAM$_{SCL}$ self-crosslinked microgels as a function of the radial position. (**a**) Typical topography and elastic modulus images of a single PNIPAM microgel (top: BIS, bottom: SCL). Scale bars: 200 nm. (**b**) Plot of the elastic modulus normalized by the elastic modulus at the centre, $Y_c = 340 \pm 10$ kPa for PNIPAM$_{BIS}$ and $Y_c = 13 \pm 3$ kPa for PNIPAM$_{SCL}$, vs. the radial position calculated from at least five microgels using high-resolution elastic modulus mapping and the height trace (dashed lines) reconstructed from vertical tip position during force map acquisition. Reprinted from Ref. [142]. CC BY 3.0.

The elastic moduli of microgels can be routinely determined using atomic force microscopy (AFM) for surface-adhered microgels [32,146,147] (see Figure 7); various other techniques for characterizing the mechanical properties of polymeric particles have been recently reviewed in Ref. [148]. Radial stiffness measurements for microgels adsorbed to a planar substrate using AFM show an increasing Young's modulus toward the center/apex of the gels [32,142]. The decrease of the measured elasticities towards the rim of the microgel is usually interpreted as higher polymer and crosslinker densities in the core and lower densities in the outer shell [140]. Therefore, microgels have been proposed to mutually interact in a brush-like manner with a polymeric corona surrounding a dense core [149]. Table 3 shows the wide range of elastic moduli that have been measured in the center of microgels with radii relevant to drug-delivery applications, which can be engineered during synthesis [150]; ultra-low crosslinked microgels have very small elastic moduli and do not show a radial stiffness gradient [142,151,152]. Swollen microgels in good solvents are often modeled as homogeneous elastic spherical particles with Young's moduli Y proportional to the number of crosslinks, and can be simulated using networks of harmonic springs [153]. The Poisson's ratio of swollen microgels is $\nu_\mathrm{P} = 0.25$, due to the central forces between the crosslinks [154]. An increase in temperature leads to a decrease in solvent quality and therefore to a collapse of the microgel [32]. In the collapsed state, computer simulations using bead-spring models for the polymers show that with increasing temperature, the Poisson's ratio initially decreases with decreasing solvent quality and finally assumes values $0.4 < \nu_\mathrm{P} < 0.5$ in the collapsed state [155]. A microgel in the collapsed state has a significantly higher Young's modulus compared with the swollen state (see Table 3) and may thus in some systems also be modeled as a spherical hard particle [156,157].

Table 3. Elastic moduli of nano- and microgels [1].

Microgel	Young's Modulus Y (Swollen)	Y (Collapsed)	References
$\mathrm{PAAm}_\mathrm{BIS}$	6.5 ± 1.6 kPa	n/a	[146]
POx-HASH	7.1 ± 2.5 kPa	n/a	[146]
$\mathrm{PNIPAM}_\mathrm{SCL}$	13 ± 3 kPa	n/a	[142]
$\mathrm{P(OEGMA_{300})_{SCL}}$	123 ± 6 kPa	n/a	[142]
PNIPAM with 20% AAc	≈150 kPa	≈400 kPa	[158]
PNIPAM with BIS [2]	0–1000 kPa	20 times increased	[159]
PNIPAM with BIS and DMA [2]	0–1000 kPa	>100 times increased	[159]
$\mathrm{P(MEO_2MA}\text{-}co\text{-}OEGMA_{300})_{SCL}$	292 ± 2 kPa	n/a	[142]
$\mathrm{P(MEO_2MA}\text{-}co\text{-}OEGMA_{500})_{SCL}$	850 ± 6 kPa	n/a	[142]
$\mathrm{P(MEO_2MA}\text{-}co\text{-}OEGMA_{500})_{EGDMA}$	$63{,}000 \pm 500$ kPa	n/a	[142]

[1] The microgels with Young's moduli $Y > 10$ kPa have radii in the range $200\,\mathrm{nm} \leq R_\mathrm{mg} \leq 600\,\mathrm{nm}$, relevant to drug delivery, wguke those with $Y < 10$ kPa have radii $12\,\mu\mathrm{m} \leq R_\mathrm{mg} \leq 15\,\mu\mathrm{m}$. [2] Data for various concentrations of the crosslinker BIS and the cononomer DMA.

Ultra-low crosslinked (ULC) ultrasoft microgels were first reported in 1993 for PNIPAM [160] (see Figure 8). Subsequently, the effect of self-crosslinking has been studied—expanding on the previous understanding of the phase behaviour of PNIPAM [161,162]—to understand the origin of the stability of these self-crosslinked (SCL) microgels that form without additional crosslinkers [163–166]. The size of ULC microgels can be controlled, e.g., by the addition of a surfactant during precipitation polymerization [167]. In their swollen state, ULC microgels have homogeneous Young's moduli ≈ 10 kPa. Because of their softness, they easily attach and spread on substrates [104,152,168,169]. ULC PNIPAM microgels with radii of more than 200 nm have been found to easily translocate through pores with radii of 50 nm [104]. In peak-force tapping mode, sharp AFM tips experience very low forces of the order of 100 pN, and the microgels become invisible to the AFM [170]. Upon collapse, deswelling can lead—depending on size, ionic, and electrostatic interactions—to internal microphase separation [171,172]. Compared with microgels of similar collapsed radii ≈150 nm and synthesized at finite crosslinker concentrations, which have hydrodynamic radii of 300–350 nm in their swollen states, ULC microgels swell to 400–550 nm [151].

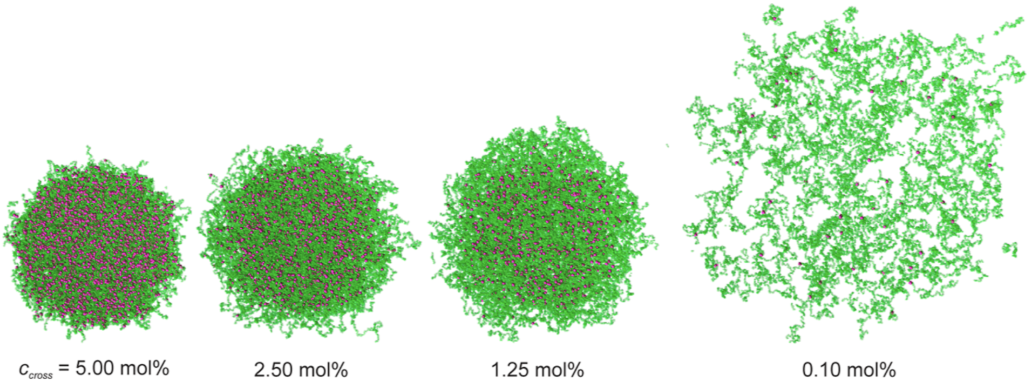

Figure 8. Representative snapshots of in silico microgels down to ultra-low crosslinked for microgels with $N \approx 336{,}000$ monomers interacting via the WCA potential for 'bead size' σ in good solvent conditions, mimicking $T = 20\,^\circ\mathrm{C}$ in experiments. To improve the visualization, all the plots represent a slice of the microgels of width 30σ. Monomers are reported in green, while crosslinkers are in red. For ultra-low crosslinked (ULC) microgels, we use $c_{\mathrm{cross}} = 0.1\%$, which agrees well with the experimental data in terms of swelling ratio and form factors. Reprinted with permission from Ref. [151]. Copyright 2023 American Chemical Society.

The 3D network architecture makes microgels an especially versatile class of polymeric particles. Variations of conventionally crosslinked microgels with an approximately homogeneous distribution of polymers include core-shell microgels [173], core-double-shell microgels [174], core-shell microgels with anisotropic shapes [175], and hollow microgels [176]. Microgels with several shells may have several temperatures for swollen–collapsed transitions [174]. Hollow, pH-sensitive microgels can, for example, serve as stimuli-responsive nanocontainers for hydrophilic drugs [176]. Ultra-low crosslinked microgels can be synthesized by penetrating and enclosing a core formed by a conventionally crosslinked microgel [177–179].

2.6. Biomolecular Condensates

Biomolecular condensates are lyophilic colloids formed by the condensation of macromolecules via liquid–liquid phase separation (LLPS), which is often driven by electrostatic interactions [180]. An equilibrium mean-field theory approach for the gelation of associative polymers that interact via "stickers" (e.g., ionic or hydrophobic groups) via reversible junctions is always accompanied by a tendency of the system to phase-separate [181]. Because the condensates lack a lipid-bilayer membrane bounding them, such gel-like colloids are sometimes also referred to as membrane-less organelles or droplets [182]. Condensates are often small, with sizes between a few and a few hundred nanometers in living cells [18], and can reach micrometer sizes outside cells. In vivo, the condensates form and dissolve depending on their environment and dynamically structure the cytoplasm, as also shown in the seminal study on *C. elegans* [183]; the physical processes determining the sizes of the condensates are often still unclear. An exponential size distribution has been found for nuclear speckles whose growth is determined by initially fast and then gradual coalescence, whereas Huntingtin aggregates with a continuous material production are power-law distributed [184]. In vitro, the size distribution of the condensates can be controlled, e.g., by the polymer concentration in the systems in which the condensates are formed and the temperature [111], or by the composition in multi-component condensates [185].

Biomolecular condensates are unique as potential drug-delivery vectors because they can accommodate a wide variety of molecules and help deliver them to cells. Partitioning small molecules into condensates with folded domains has recently been studied for ≈1700 biologically relevant small molecules, including ≈200 metabolite compounds and ≈1500 drug compounds approved by the US Food and Drug Administration (FDA), complemented by ≈100,000 randomly chosen biologically acrive small molecules from the ChEMBL database [186]. The pharmacokinetic, physicochemical, and chemical properties have been predicted computationally, and a dimension reduction technique showed that the selection of the biologically relevant molecules is distributed evenly across the chemical space of the random components (see Figure 9a). The partition coefficients span a range of 10^6, from exclusion to enrichment in the condensates (see Figure 9b). The results suggest that physical properties, such as hydrophobicity, are more important for the partitioning than specific chemical structures. More diverse condensate systems remain to be tested.

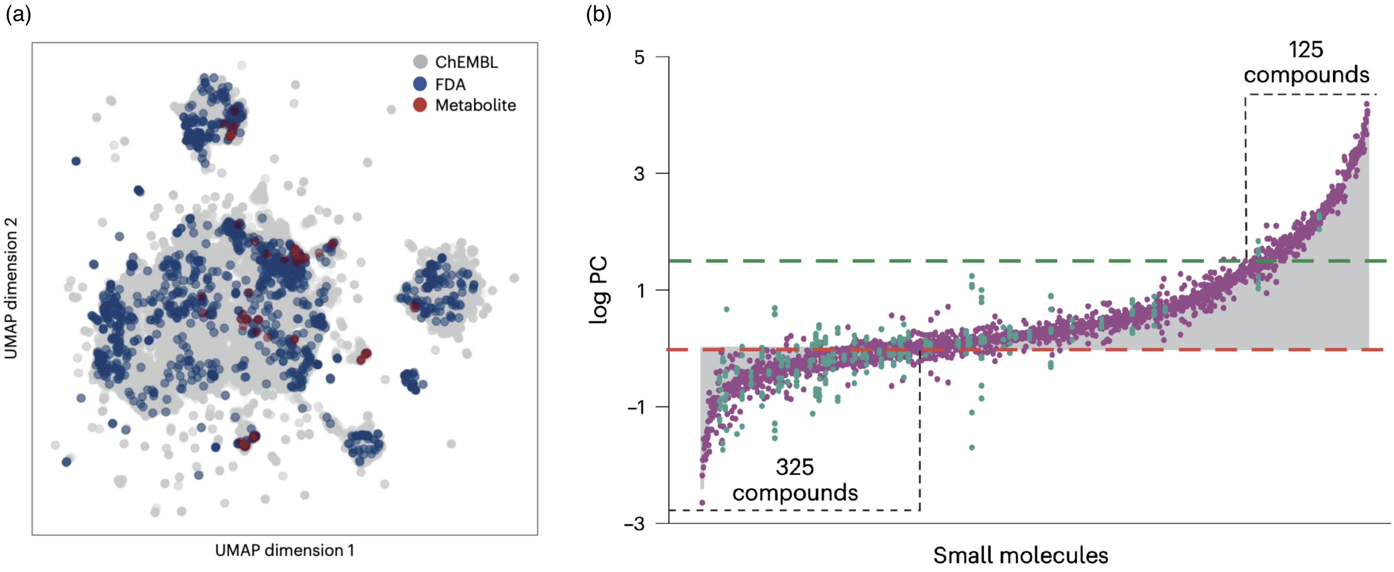

Figure 9. Biomolecular condensates for delivering small molecules. (**a**) Uniform manifold approximation and projection (UMAP) representation of 1700 small molecules used in the analysis [187], which is based on physical features generated in QikProp [188]. (**b**) Partition coefficients (PC) determined using mass spectrometry vary over nearly six orders of magnitude. Bar chart of PC values, ordered from smallest to largest, for the partitioning of 1037 compounds into the SUMOSIM condensate (composed of polySUMO and polySUMO-interaction motif (SIM) proteins [189]). Red and green dashed lines indicate $\log \mathrm{PC} = 0$ and $\log \mathrm{PC}_{\mathrm{SUMOSIM}} = 1.77$, respectively. The numbers of compounds with $\log \mathrm{PC} < 0$ and $\log \mathrm{PC} > \log \mathrm{PC}_{\mathrm{SUMOSIM}}$ are indicated. The grey-coloured areas represent the bar plots for the mean values of the data, and green and purple dots represent metabolites and drug compounds, respectively. Reprinted from Ref. [186]. CC BY 4.0.

In a "stickers" picture, for proteins, DNA, and RNA, specific chemical interactions may serve as stickers, with the chemical nature of the spacer region in-between changing the behavior of a condensate from fluid to solid. Understanding the rules that govern the interactions between small molecules and the biomolecules within the condensates is also referred to as "chemical grammar" [190]. DNA itself can serve as a base material to hierarchically design condensates for delivering cargo to cells [191]. A partitioning of large cargo into condensates can also be achieved through specific interactions, as demonstrated for biotin-functionalized beads [192]; moreover, beads with a specific surface chemistry can be incorporated into immiscible condensates. Intrinsically disordered regions of proteins are often involved in binding to other molecules and inducing the formation of a condensate [193,194] (see Figure 10a). Using hybrid-resolution computer simulations that consider local structural motifs, the importance of β-sheet structures for interactions has been predicted [194]. However, an overall charge can also drive the partitioning of larger molecules into biomolecular condensates [192,195,196], with specific binding between their amino or nucleic acids and other components of the condensate only modulating a multiphase condensation [189,197]. Intriguingly, engineered biomolecular condensates containing enzymes or other chemically active components are non-equilibrium systems that can show internal flows and active regulation of their sizes [198,199]. Such non-equilibrium processes have been studied using large condensates (see Figure 10b) but may also be relevant for the smaller condensate sizes relevant to drug delivery. Interestingly, biomolecular condensates readily exchange molecules with their environment even in the presence of lipid coating—unlike vesicles whose intact lipid-bilayer membranes are impenetrable to many components (see Figure 10c,d).

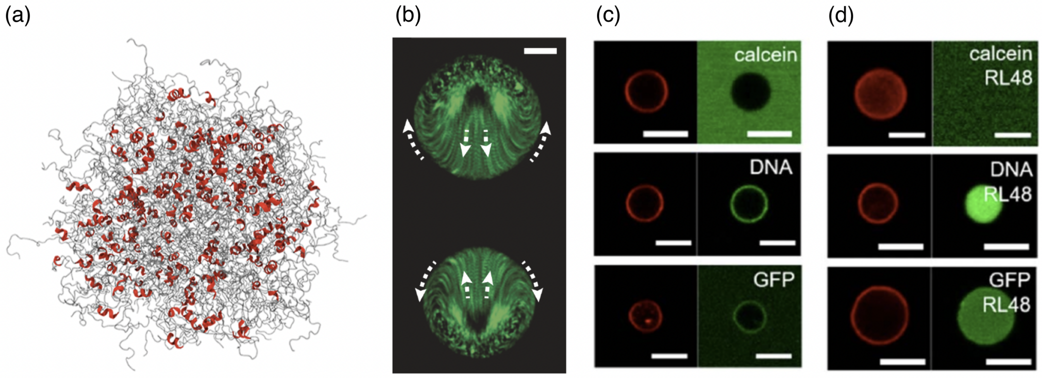

Figure 10. Biomolecular condensates containing proteins. (**a**) Intrinsically disordered proteins (IDPs) mediate phase separation that underlies the formation of a biomolecular condensate. Reprinted with permission from Ref. [194]. Copyright 2024 American Chemical Society. (**b**) Two chemically active protein condensates, pinned to a planar glass substrate functionalized with polyethylene glycol diacrylate with $M_n = 700$ (PEGDA 700) at a distance compared to the protein diameter, show internal flows induced by the presence of the other condensate. Time projection over 1 min of fluorescent particles inside two adjacent chemically active protein droplets catalyzing the urea-urease reaction (overall enzyme concentration $c_e = 0.6\ \mu\text{M}$, substrate concentration $c_{s=100\,\text{mM}}$). Arrows indicate the internal flow direction. The scale bar corresponds to 10 µm. Reprinted from Ref. [199]. CC BY 4.0. (**c**,**d**) Permeability of giant unilamellar vesicles (GUV) and lipid-coated protein condensates (RL48 protocells). A dye compound, calcein (20 µM), 21 base pair DNA (0.5 µM), and green fluorescent protein (GFP) are treated to (**c**) GUV and (**d**) RL48 protocells for 10 min before confocal analysis. Lipid coatings (red) and dye-labeled external materials (green) are imaged. The scale bars correspond to 5 µm. Reprinted from Ref. [116]. CC BY-NC 3.0.

The mechanical properties of colloids can range from fluid to solid-like [200]. For fluid condensates, typical interface tensions between the condensates and water/cytosol are usually small, in the range between 1 and 100 µN/m, and in some cases they can also reach 1 mN/m (see Table 4). A tension of the order of 1 µN/m has also been predicted theoretically for colloid–polymer mixtures [201]. For comparison, oil–water and air–water interface tensions are of the order of 10–100 mN/m. Experimentally, the interface tensions can be determined using a variety of techniques, including sessile-drop measurements [202], micropipette aspiration [203], and fluctuation spectroscopy [204]. The fluctuation-spectroscopy measurements require, in addition to tension, also bending rigidity to describe the curvature-elastic parameters of the interfaces of biomolecular condensates [204] (see Table 4). Computer simulations predict the physiologically relevant range of biomolecular condensation to lie close to the critical point marking the highest temperature for phase coexistence, such that the interface tension can be expected to follow the scaling laws characterized by the critical exponents [109]. Because electrostatic interactions are often important, the addition of salt can decrease the interface tension [205,206] (see Table 4), which has been found using optical traps to apply to the viscoelasticity as well [206]. An increased fraction of uncharged, highly branched polymers in the buffer surrounding the condensate can increase the interfacial tension [207].

Table 4. Interface tensions and bending rigidities of biomolecular condensates.

Condensate	**Interface Tension γ**	**Bending Rigidity κ**	**References**
clotrimazole	0.627 μN/m	2.05 k_BT	[204]
FXR1 overexpression and sodium arsenide	0.741 μN/m	1.36 k_BT	[204]
sodium arsenite	1.26 μN/m	2.08 k_BT	[204]
PGL-3 proteins at various KCl concentrations [1]	1–5 μN/m	n/a	[208]
nucleoli in HeLa cell nuclei	1.5 ± 0.5 μN/m	n/a	[209]
Ddx4^N 1–231 in aqueous buffer	38 ± 3 μN/m	n/a	[202]
ELF3 proteins	49 ± 9 μN/m	n/a	[210]
polylysine:heparin mixture and Ficoll70 [2]	70–125 μN/m	n/a	[207]
Ddx4^N 1–229 in aqueous buffer	82 ± 10 μN/m	n/a	[202]
LAF-1 RGG	159 ± 10 μN/m	n/a	[203]
[RGRGG]$_5$-dT40 at various NaCl concentrations [1]	0.5–1.6 mN/m	n/a	[205]

[1] Higher surface tensions are measured at lower salt concentrations. [2] Equimolar mixture of polylysine and heparin, for various Ficoll70 concentrations.

Working on biomolecular condensates relevant for drug delivery can also still mean learning from nature, in particular, because the research on condensates in vivo is a very active research field as well. Condensates of different macromolecules have been found to colocalize in some cases, which may allow for an exchange of molecules (see Figure 11a). Time-lapse movies of coalescence show the droplet nature of biomolecular condensates [209], e.g., for the coalescence of nucleoli (see Figure 11b). Furthermore, their fusion and surface fluctuations allow us to measure the rheological properties of the droplet and the surrounding fluid. The viscosities of biomolecular condensates range from 100 mPas to 1 kPas [203]; the viscosity of nuclear speckles and nucleoli is of the order of 1–10 kPas and thus three to four orders of magnitude higher than the viscosities of many other in vitro condensates and water droplets [211]. Aging condensates have been observed to decrease in size. In parallel, their elastic modulus varies only weakly, but the viscosity increases strongly [206]. Whereas fluorescence recovery after photobleaching in PGL-3 occurs in less than a minute if the condensate is younger than 30 min, the half-life time is ≈50 min for 46-hour-old condensates. Similarly, coalescence right after formation takes place in 10 s, whereas it takes tens of minutes for 46-hour-old condensates.

Interfacial protein clusters that adsorb to the surface of the condensates during LLPS have been shown to change their interfacial properties [20] (see Figure 11c). Although this is reminiscent of classical Pickering emulsions [212], the energy gain for the protein clusters to be located at the interface of a condensate is much smaller than typical energies of particles at an oil–water interface because of the smaller size of the protein clusters and the small interface tension. Therefore, although the protein clusters lower the effective interface tension and slow down coarsening as expected for classical Pickering emulsions, a condensate-cytoplasmic exchange of the clusters can be expected to lead to an equilibrium of bound ‘particles’ at the interface instead of irreversible binding. Protein cages attached to the interface of condensates can thus be used to precisely control the condensate radii [213]. Similarly, although not leading to monodisperse condensates, the binding of RNA molecules to the surface has been shown to decrease the condensate size [19].

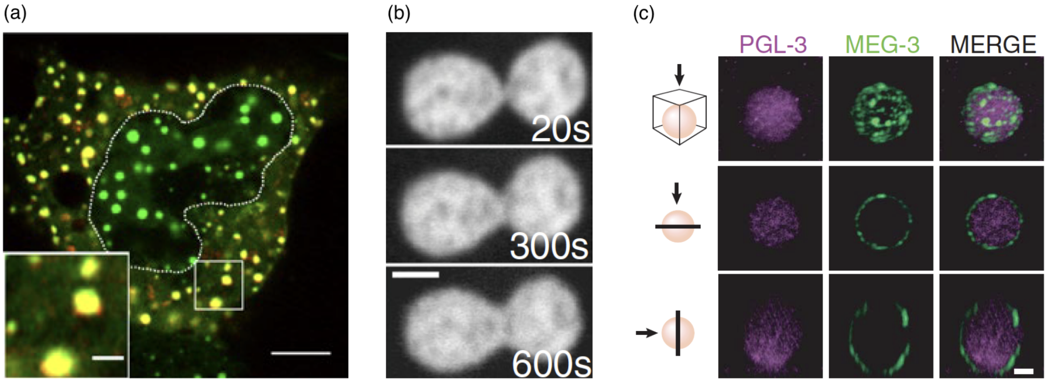

Figure 11. Biomolecular condensates: colocalization, coalescence, and interface decoration by protein clusters. (**a**) Cytoplasmic enhanced green fluorescent protein (EGFP)–yes-associated protein (YAP) selectively enriches different proteins. Live-cell image showing the colocalization of EGFP–YAP (green) condensates with mCherry–Dcp1a (red) condensates in the cytoplasm of HEK293T cells after hyperosmotic stress that induced condensate formation, 20 s after sorbitol treatment. The dotted line indicates the nucleus, green fluorescence EGFP-YAP condensates, red mCherry-Dcp1a condensates, and yellow colocalization. The scale bars correspond to 5 µm (whole-cell image) and 1 µm (magnified view of the boxed region). Reproduced from Ref. [214] with permission from Springer Nature. (**b**) Time-lapse of nucleolar coalescence after the nucleolar signal at $t = 0$ s in the nucleus of a live HeLa cell. The frames show the progress of the nucleolar fusion. The scale bar corresponds to 2 µm. Reprinted with permission from Ref. [209]. Copyright 2018 by the American Physical Society. (**c**) MEG-3 forms low-dynamic clusters that adsorb to the surface of PGL-3 condensates. Photomicrographs of a P granule reconstituted in vitro with purified PGL-3 and MEG-3 trace-labeled with Dylight 488 and Alexa 647, respectively. The scale bar corresponds to 3 mm and applies to all images in the set. The top panels are a maximum projection of a z-stack through the granule. The middle panels are a single x-y plane through the middle of the same granule. The lower panels are a single z-x plane through the middle of the same granule. Reproduced from Ref. [20], AAAS.

3. Circulation Times

The concentration of drug-delivery vectors in the blood circulation system decreases with increasing time after the administration. For small drug molecules, a characteristic time for the distribution of the drugs by permeation through the vascular wall and a significantly longer time for the elimination of the drug are distinguished. The fast and slow decrease of the concentration are also referred to as α and β phase, respectively [215]; the α phase is often found up to 1h after the administration. For polymer-based delivery vectors, the strategies to prolong the blood circulation time are versatile [216]. The elimination of the delivery vectors from the blood circulation is usually achieved by the mononuclear phagocyte system (MPS), also referred to as the reticuloendothelial system (RES). For drug-delivery vectors, often only the elimination from the circulation is characterized. A prolonged circulation time for delivery vectors without a detectable α phase is referred to as the stealth effect, whereas a prolonged characteristic time for the concentration decrease in the β phase for systems with a detectable α phase is referred to as the pseudo-stealth effect; more than 85% of stealth nanomaterials have been reported to show an α phase [215]. The half-life times of lipid–polymer hybrid nanoparticles with sizes between 100 and 200 nm in the blood of mice, calculated from the measured concentration decays, can be prolonged by polymer functionalization by up to two orders of magnitude [217] (see Table 5). The half-life times of PEG-coated gold nanoparticles have been shown to increase with both increasing PEG molecular weight and decreasing gold nanoparticle size [81,82] (see Figure 12a). Studies on PEG gels with diameters of 2 to 3 µm show that the circulation times increase with decreasing gel stiffness (see Figure 12b).

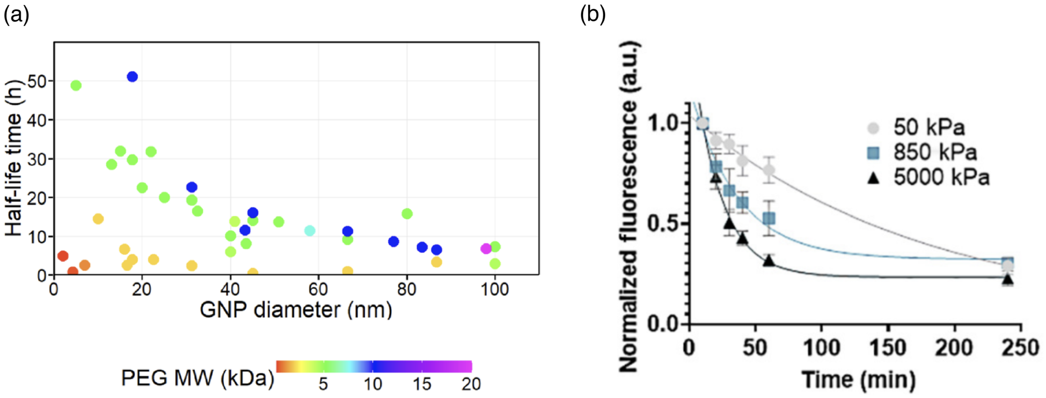

Figure 12. Circulation times. (**a**) Circulation half-life times of gold nanoparticles (GNP) with various diameters and PEG coatings of various molecular weights (MW). The color of the data points corresponds to the MW of the PEG coating. Adapted from Ref. [82]. CC BY 3.0. (**b**) Clearance profiles of PEG particles with diameters between 2 and 3 µm and elastic moduli of 50, 850, and 5000 kPa after intravenously injecting them into mice. Reproduced from Ref. [218] with permission from Springer Nature.

Table 5. Elimination half-life times of bare and coated liposomes and metallic (nano-)particles [1].

Particle	Surface Properties	Hydrodyn. Diam.	Half-Life Time $t_{1/2}$	References
lipid nanoparticles	bare	142 nm	0.3 h	[217]
lipid nanoparticles	HEP	164 nm	1.49 h	[217]
lipid nanoparticles	PEG	128 nm	2.73 h	[217]
lipid nanoparticles	PEG/HEP	132 nm	72.6 h	[217]
liposomes, first dose	bare	98.7 nm	12.0 h	[219]
liposomes, second dose	bare	98.7 nm	12.3 h	[219]
liposomes, first dose	PEG	107.7 nm	33.6 h	[219]
liposomes, second dose	PEG	107.7 nm	1.66 h	[219]
liposomes, first dose	HPMA	110.0 nm	16.0 h	[219]
liposomes, second dose	HPMA	110.0 nm	15.5 h	[219]
gold nanoparticles, 17 nm diameter	2 kDa PEG	25.2 nm	4.0 h	[81]
gold nanoparticles, 17 nm diameter	10 kDa PEG	63.5 nm	51.1 h	[81]
gold nanoparticles, 87 nm diameter	10 kDa PEG	118.9 nm	6.6 h	[81]

[1] Experiments performed using mice.

The physicochemical properties of drug-delivery vectors are not the only parameters important for the circulation time, but also the immunological response of the organism to which the vector is applied. Bare lipid nanoparticles, liposomes, and gold nanoparticles can be eliminated from the blood circulation of mice within a few hours; polymer functionalization can extend the circulation half-life times to several days (see Table 5). However, a PEG coating can induce the production of antibodies against PEG, which significantly shortens the circulation times after a first dose has been applied. The antibodies lead to accelerated blood clearance in the liver and the spleen for follow-up applications of the vector [219–222]. Intriguingly, measurements of the half-life times of liposomes with diameters of ≈100 nm in rats showed marked differences between the first and the second dose, applied 6-8 days later, for PEG-coated liposomes. Whereas the PEG–lipid hybrid nanoparticles showed a half-life time prolonged by almost a factor of three compared with bare liposomes after the first dose, the half-life time was reduced by more than 80% compared with bare liposomes after the application of the second dose [219]. Polymers other than PEG do not induce an immunological response and thus show more promise for translation into clinical practice. For example, a difference between the half-life times after the first and second dose has not been observed for liposomes coated with, e.g., poly(vinylpyrrolidone)

(PVP), poly(N,N-dimethylacrylamide) (PDMA), N-(2-Hydroxypropyl)methacrylamide (HPMA), and poly(N-acryloyl morpholine) (PAcM) [219]. Polysarcosines also show a low antigenicity [220].

For polymer-functionalized drug-delivery vectors, the functionalization changes the chemical surface properties, as well as size and elasticity. It has been shown using particle-based mesoscale hydrodynamic simulations that the size and shape of particles affect their radial distribution in capillaries, i.e., their margination at the capillary walls [223,224]. Polymer gels enable us to study the effect of elasticity on the circulation time for delivery vectors with otherwise similar physico-chemical properties and, in particular, without a need to consider the core. The longer half-life times measured for soft compared with stiff hydrogels qualitatively confirm the observed prolonged half-life times for polymer-grafted nanoparticles that are softer (and larger) than the bare particles. For PEG-based hydrogel nanoparticles with hydrodynamic radii ≈100 nm, soft particles with a bulk modulus of ≈10 kPa show an (α-phase) circulation half-life time of ≈2 h, whereas stiff particles with a bulk modulus ≈3 MPa are cleared from the circulating blood of mice within minutes [225]. However, the difference between the circulation times of both particles nearly disappears for times larger than 4 h. Similarly, the organ distribution of the particles is significantly different at short times, but the differences nearly disappear after 12 h when the vast majority of the particles are found in the liver and the spleen. A faster clearance of stiffer gels from the blood circulation has also been reported for PEG-based nanogels with hydrodynamic radii of ≈100 nm and elastic moduli of 37 kPa and 93 kPa in mice, which has been hinted to be caused by the measured faster uptake of the stiffer gels by monocytes and macrophages [226]. Similarly, polyion complex vesicles with their permeable and presumably flexible polyelectrolyte shell also show long circulation times [86,227].

4. Cellular Uptake Mechanisms

In vivo, erythrocytes remain in the circulation system for ≈120 days. An increased rigidity is believed to be a key factor for the elimination of old erythrocytes from the circulation. Therefore, particles to be injected into the bloodstream have been engineered with sizes, shapes, and elasticities akin to those of healthy erythrocytes, aiming to maximize the circulation time [228–230]. (Cargo can also be attached to erythrocytes in order to increase its circulation time [231].) Accordingly, the dependence of phagocytosis on erythrocyte stiffness has also been studied [232]. After a short discussion on measuring cellular uptake and drug release, and the role of a protein corona and polymer functionalization of drug-delivery vectors, the three main uptake mechanisms of (i) membrane translocation, (ii) passive endocytosis and fusion, and (iii) active cellular uptake processes will be discussed. Membrane translocation is particularly interesting for the delivery of proteins to cells, because it avoids endosomal trapping and allows the delivery of vectors directly to the cytosol [233,234]. Whereas endocytosis is generally considered in biology as an energy-consuming process, the term "passive endocytosis" may have been coined in chemistry or physics and is often used when the effects of particle elasticity, shape, and size, and particle–membrane adhesion for the interaction of particles with lipid-bilayer membranes are studied [235,236]. Although most cellular uptake processes do require metabolic energy, insights gained from passive endocytosis provide valuable mechanical insights that are also believed to be relevant to active uptake processes and are, therefore, also discussed in review articles on cellular uptake [237]. However, a complete mechanistic understanding of cellular uptake requires a consideration of active uptake processes also on the level of model systems.

4.1. Characterizing Cellular Uptake

Cellular uptake of drug-delivery vectors can be characterized in vitro using fluorescence microscopy. For example, by fitting the fluorescence intensity of HEK293T cells that are exposed to NIPAM-MAA-5S microgels with an exponential function, a characteristic timescale for cellular uptake between seconds and minutes has been found (see Figure 13a–c). Small and less crosslinked microgels are taken up faster than larger microgels and microgels with a higher degree of crosslinking [238]. However, not only the kinetics of the uptake process but also the total uptake within a specific time window is of interest for characterizing the cellular uptake of a drug. Furthermore, eventually the availability of the drug to the cell is key for therapeutic applications. Two different time scales thus have to be distinguished: for the delivery of the drug-delivery vector and for the delivery of the drug; both are determined by the vector's structural and chemical properties, and the latter can take significantly longer [239]. Controlled in situ formation of condensates can even be used as reservoirs for therapeutics in cells [240]. However, loading and release kinetics will not be discussed in detail here.

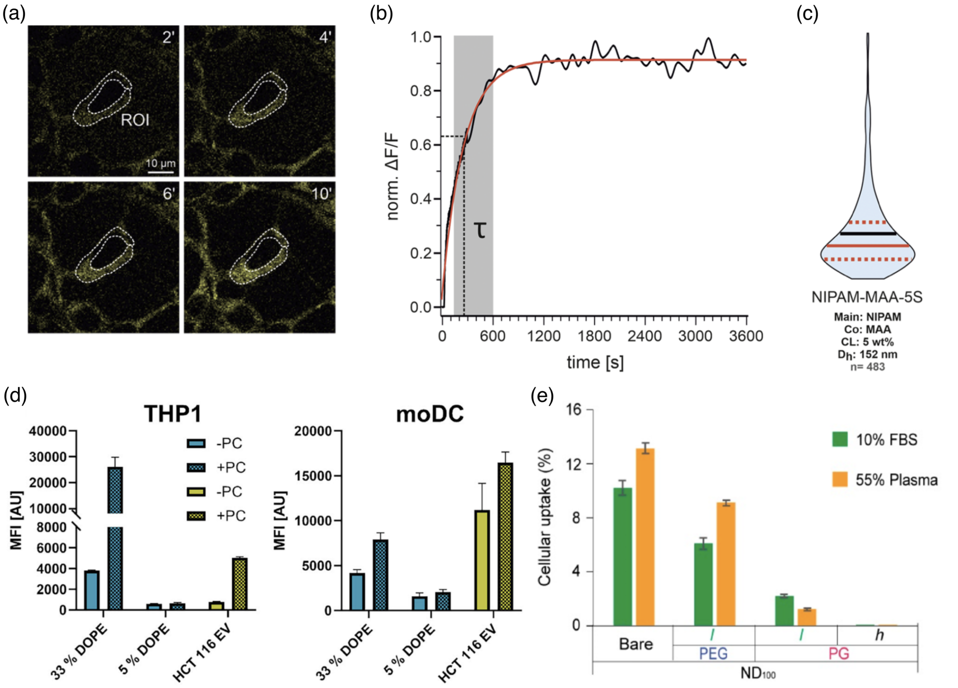

Figure 13. Cellular uptake. (**a**–**c**) Uptake kinetics for NIPAM-MAA-5S microgels by HEK293T cells. (**a**) Fluorescence confocal images 2, 4, 6, and 10 min after microgel application. A donut-shaped region-of-interest (ROI) demarks the cytosolic area of a representative cell. (**b**) Increase in the fluorescence in the ROI marked in (**a**). Normalized intensity changes ($\Delta F/f_0$) as a function of time (black trace) and as a monoexponential fit (red), used to calculate the cell-specific time constant τ. The gray background marks the experimental period represented in (**a**). (**c**) Violin plot for the distribution of time constants, starting at $\tau \approx 0$ s. Solid horizontal lines indicate the mean (black) and median (red) values, and the upper and lower quartiles (dashed lines). Adapted with permission from Ref. [238]. Copyright 2020 American Chemical Society. (**d**) Uptake of liposomes (blue) and extracellular vesicles (green) with and without protein corona (PC), determined using flow cytometry to measure the mean fluorescent intensities characterizing the uptake of the particles into THP1 and moDC cells after 16 h. Mean values and standard deviations of median fluorescence intensities are shown ($n = 3$). Reprinted from Ref. [53]. CC BY 4.0. (**e**) Quantification of nanodiamonds taken up by macrophages after 12 h incubation time, determined using extinction spectroscopy. The data are represented as the mean value ± standard deviation of three independent replicates. Reprinted with permission from Ref. [54]. Copyright 2020 American Chemical Society.

In biological fluids, the formation of a protein corona around drug-delivery vectors is a crucial factor for cellular uptake. A study for the uptake of synthetic and extracellular vesicles with diameters of $\approx 100\,\mathrm{nm}$ with and without a protein corona showed that the uptake can be significantly increased in the presence of the corona [53] (see Figure 13d). For phagocytic THP1 cells, the presence of a corona can increase cellular uptake by almost up to an order of magnitude, and for monocyte-derived moDC cells, by up to a factor of 1.5–2. Phagocytic uptake by U937 cells in fetal bovine serum (FBS) and plasma is suppressed by about 50% using a polyethylene glycol (PEG) coating and, to a much higher percentage, using a polypropylene glycol (PG) coating [54] (see Figure 13e). Polymer functionalization not only changes the sizes, shapes, and elastic properties of drug-delivery vectors but also influences the formation of a protein corona. Thus, the chemical surface properties of the delivery vectors are also crucial for understanding their uptake [54].

4.2. Lipid-Bilayer Translocation

Linear polymer chains with suitable hydrophobic/hydrophilic properties have been shown to translocate through lipid bilayers (see Figure 14). Here, a balanced hydrophobicity of each monomer or an appropriately designed sequence of hydrophilic and hydrophobic monomers allows the polymer to experience the lipid-bilayer membrane as a small perturbation to a flat potential-energy landscape, such that the polymers translocate through the membrane almost freely [63,64]. The translocation is accompanied by an increase in the permeability of the membrane to solvent, which is maximal in a finite distance in the plane of the membrane from the center of the polymer. Very hydrophobic polymers aggregate in the core of the bilayer along with the tails of the lipid molecules, whereas hydrophilic polymers cannot enter the hydrophobic core and experience the membrane as confinement [63,64].

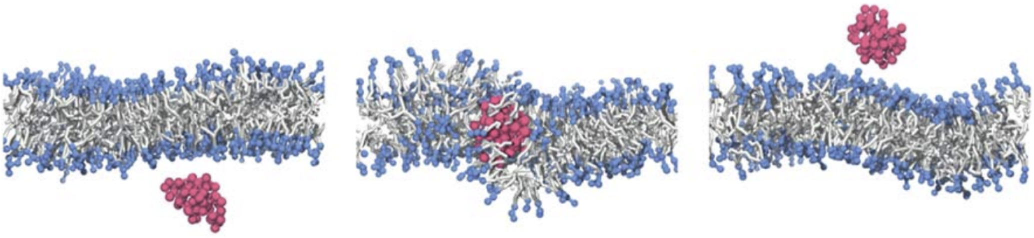

Figure 14. Simulation snapshots of a linear polymer chain with intermediate hydrophobicity translocating through a lipid-bilayer membrane. Used with permission of the Royal Society of Chemistry, from Ref. [63]; permission conveyed through Copyright Clearance Center, Inc.

The translocation rates for linear copolymers with a balanced periodic sequence of hydrophobic and hydrophilic monomers that repeats at distances below the thickness of the lipid bilayer are independent of the polymer chain length. In contrast, the translocation rates for random copolymers with an overall balanced hydrophobicity decrease exponentially with increasing chain length [62]. Polymer translocation may be influenced by membrane shape. Simulations using a dumbbell model for the lipid molecules in bilayers predicted asymmetric polymer transport, because of a lipid-entropy difference due to a curvature-induced difference in lipid fluctuations in the two monolayers [241]. Similarly, using a chain-like lipid model, it has been predicted that for polymers being partitioned in the hydrophobic core of the membrane, a higher concentration of polymers is expected to be found in the outer monolayer of a curved bilayer. Although the membrane-curvature dependence of polymer translocation has not yet been studied using more recent lipid models, it can be expected to be observed also for the more sophisticated coarse-grained modeling approaches that are currently used.

Alternating amphiphilic copolymers have been synthesized, and their interaction with giant unilamellar vesicles (GUVs) has been studied using fluorescence microscopy [60]. The GUVs were initially devoid of polymers. Using kinetic modeling, a fast saturation of the membrane with polymers and a slow release of the polymers to the interior of the vesicle have been predicted. The translocation rate has been shown to decrease with increasing lipid chain length and bilayer thickness, both of which suggest the presence of an increased free-energy barrier. The experimentally observed translocation of polymers through lipid bilayers is thus similar to predictions from analytical and computer-simulation studies on the translocation of linear polymers through holes/pores [242], where the free-energy barrier for translocation results from the reduced entropy of the polymer chain. Brownian Dynamics simulations demonstrated an increased free-energy barrier for pore translocation with increasing pore length [243]. Synthetic polymers with alternating hydrophilic and hydrophobic units for lipid-bilayer translocation, which can be used as drug carrier systems for targeted and controlled delivery, have been patented [61].

A translocation-like integration into the lipid-bilayer membrane without wrapping has, using computer simulations, also been observed beyond linear chains for nanogels [244]. However, in the latter case, the translocation process did not take place because, after attachment, the gels no longer detached from the membranes. Lipid-bilayer penetration has been experimentally suggested for polymer-coated nanoparticles [115] and has been directly observed for biomolecular condensates. It allows for a direct delivery of drugs to the cytosol without envelopment of the delivery vector by the lipid-bilayer membrane [113], as shown for condensates of oligo-arginine and DNA in Figure 15a. Electrostatic attraction, which can be tuned by the ζ potential of the condensate, mediates an attraction between the condensate and the bilayer and leads to either wetting of the membrane, endocytosis, or—for optimal values of the partitioning coefficient—membrane translocation (see Figure 15b). A decrease in the vesicle size after translocation shows that some lipids remain within the condensate. For smaller condensates, translocation has been observed for higher zeta potentials compared to the large condensate. Condensates have also been shown to enter cells [113]. Micrometre-sized pH and redox-responsive condensates have been reported to deliver small peptides, enzymes, and messenger RNAs directly to the cytosol [114].

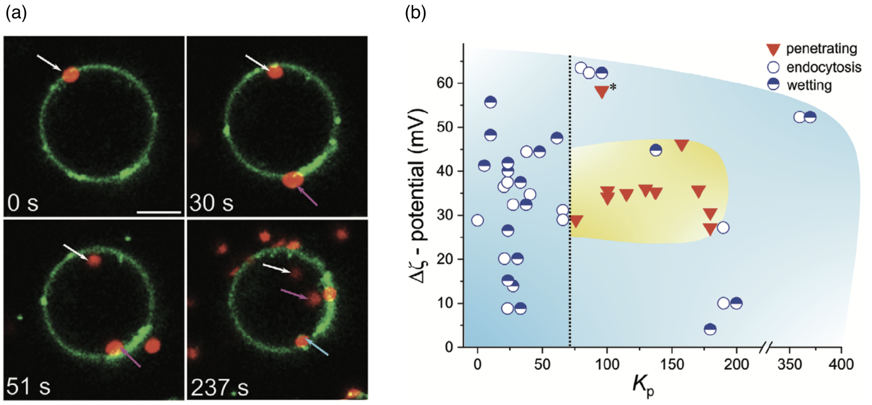

Figure 15. Wetting, endocytosis, and lipid-bilayer translocation of condensates at liposomes. (**a**) Translocation of condensates composed or oligoarginine (R_{10}, 2.7 kDa) and torula yeast RNA (tyRNA) (red, labelled with DNA polyA$_{15}$-$Cy5$ oligonucleotides, marked with arrows) at liposomes consisting of POPC$_{0.4}$/cholesterol$_{0.1}$/POPG$_{0.5}$ (green), labelled with DOPE-AttO 488. The scale bar corresponds to 10 µm. (**b**) Morphological state diagram of the interplay between complex condensates and liposomes as a function of their absolute ζ-potential difference $\Delta\zeta$ and the condensate's lipid partition coefficient K_p. * Denotes a special case of R_{40}/polyA condensates that were significantly smaller (average diameter < 1 µm) than most other condensate samples and were found to penetrate the liposome membrane despite a strong surface attraction. Reprinted from Ref. [113]. CC BY 4.0.

4.3. Passive Endocytosis

Passive endocytosis is cellular uptake by membrane wrapping of the delivery vector. It requires the adhesion of the vector to the membrane, which—due to the elasticity of the material—involves a deformation of both the polymeric delivery vector and the lipid-bilayer membrane. Adhesion of initially spherical microgels to planar substrates can result in oblate, fried-egg microgel shapes and a significant decrease of both volume and surface area [245] (see Figure 16); the microgel deformation increases with increasing adhesion strength. Using computer simulations, we showed that such strong microgel deformations can be expected for initially spherical ultra-soft microgels of radius 200 nm with Young's modulus $Y \approx 5\,\mathrm{kPa}$ attached to lipid-bilayer membranes with bending rigidity $50\,k_BT$, for receptor-ligand adhesion strengths orders of magnitude below those measured for a spherical agarose bead interacting with a planar glass substrate [246,247]. Micro- and nanogel deformations when adhering to lipid-bilayer membranes are more likely to occur the smaller the gel is. Fried-egg shapes are also observed using computer simulations for the adsorption of PGNs to substrates (see Figure 17). Comparing planar and curved substrates, the simulation results show that the adhesion energy gain for identical PGNs adhering to a planar substrate is higher than on the inside or outside of spherical caps [248]. This finding assumes a homogeneous adhesion strength between the grafted linear chains and the substrate, which may not apply to all PGNs. For nano- and microgels, a homogeneous adhesion may describe the interaction of very soft gels with lipid-bilayer membranes [226]. Various other microgels, however, have also been reported to interact with substrates via discrete adhesion sites, such as dangling chains that insert into the tail region of the lipid bilayer [249], dopamine methacrylamide crosslinkers [250], and screened electrostatic interactions at physiological salt concentrations [251].

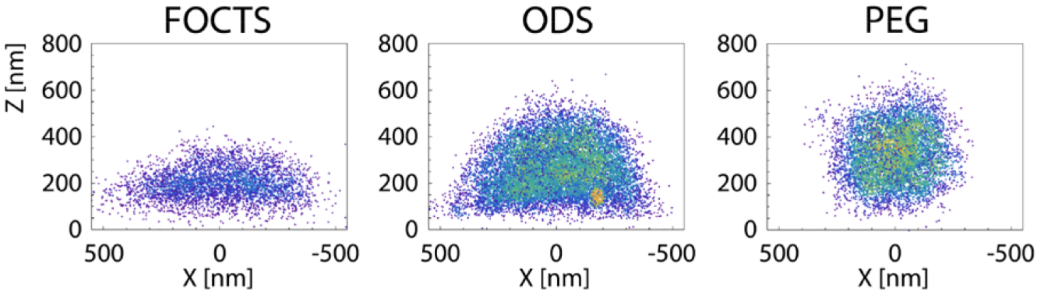

Figure 16. Images of direct stochastic optical reconstruction microscopy measurements of adsorbed PNIPMAM microgels at surfaces of different functionalization. The microgel conformation changes from a fried egg shape at hydrophobic surfaces coated with trichloro(1H,1H,2H,2H-perfluorooctyl)silane (FOCTS) or n-octadecyltrimethoxysilane (ODS) to a spherical shape at hydrophilic surfaces coated with PEG. The solid–liquid interfaces are placed at $z = 0$. Reprinted with permission from Ref. [245]. Copyright 2019 American Chemical Society.

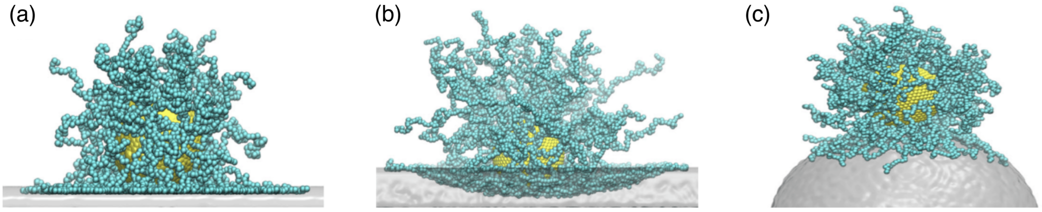

Figure 17. Snapshots of three systems of a PGN interacting with attractive substrates having: (**a**) zero (flat), (**b**) positive (hole/concave), and (**c**) negative (bump/convex) curvatures. Reprinted from Ref. [248]. CC BY 4.0.

Because the wrapping of polymeric particles usually involves a deformation of the particles in partial-wrapped states, insights on wrapping deformable particles may be gained from studies of wrapping non-spherical hard particles (see Figure 18). Here, highly curved regions of the particle surface correspond to wrapping-energy barriers. This leads to an increased stability of partial-wrapped states for non-spherical compared with spherical hard particles. For example, cube-like particles experience particularly stable partial-wrapped states if the wrapping of additional edges can be avoided [252]. Oblate ellipsoidal hard particles adhere to membranes with their flat side at weaker adhesion strengths than spherical particles with the same surface area, but wrapping the highly curved rim constitutes an energy barrier [253]. Only results of a few studies on model systems are available for wrapping of polymeric particles, including studies for stiff microgels at GUVs [157,249], capsules [254], and small nanogels [255]. So far, state-of-the-art theoretical and simulation studies on the wrapping of elastic particles use vesicles and vesicle-like particles, where the 2D shells determine the elastic properties, as a generic model system [254,256–261]. For initially spherical vesicles and capsules, shape transitions from spherical via oblate with the flat side attached to the membrane, prolate with the long axis perpendicular to the membrane, and back to spherical have been predicted [254,261]. Wrapping of initially prolate vesicles involves a change from a stable submarine to a stable rocket orientation as predicted for hard particles [252], in addition to a deformation of partially wrapped vesicles [256]. A shape change has also been experimentally observed for the cellular uptake of 200 nm sized initially spherical elastic silica nanocapsules with Young's moduli between 500 kPa and 1.18 kPa [262].

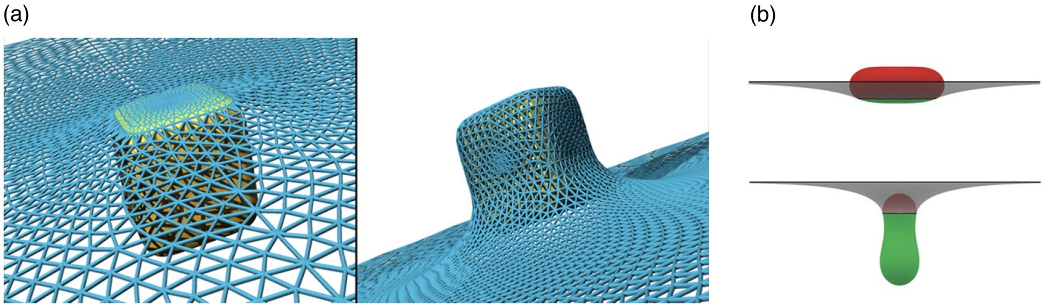

Figure 18. Wrapping of non-spherical particles. (**a**) Shallow- and deep-wrapped states of a cube at a triangulated membrane. Reprinted with permission from Ref. [252]. Copyright 2014 American Chemical Society. (**b**) Shallow- and deep-wrapped states of prolate vesicles: attached (green) and free (red) vesicle membrane area. Reprinted from Ref. [256]. CC BY 4.0.

In general, from a mechanical point of view, the wrapping of hard particles at lipid-bilayer membranes is well understood [263,264]. Synthetic model systems [231,265–267], as well as theory and computer simulations [235,252,253,268–272] have helped to rationalize both the wrapping process and the membrane-mediated interactions between partially wrapped nano- and microparticles at membranes. Spherical hard particles at tensionless membranes directly transition from the non-wrapped to the complete-wrapped state beyond the threshold adhesion strength $w = 2\kappa/(\pi R^2)$, where κ is the bending rigidity of the membrane and R the particle radius [271,272]. Systematic calculations for particle wrapping show that a finite membrane tension stabilizes partial-wrapped states (see Figure 19a). If such a continuum membrane model is used for the calculations, often dimensionless parameters like the reduced adhesion strength $\tilde{w} = wA_{\mathrm{p}}/(2\pi\kappa)$ and the reduced membrane tension $\tilde{\sigma} = \sigma A_{\mathrm{p}}^2/(\pi\kappa)$ for a spherical particle help to make the numerical predictions transferable to experimental systems with various particle surface areas A_{p}. For prolate vesicles, calculations of wrapping states using a continuum membrane model predict a dominance of vesicle shape for high bending rigidity ratios $\kappa_{\mathrm{v}}/\kappa_{\mathrm{p}}$ between the vesicle membrane and the membrane the vesicles attach to, and a dominance of vesicle deformability leading to a strongly enlarged regime of stable partial-wrapped states for highly deformable vesicles and small $\kappa_\mathrm{v}/\kappa_\mathrm{p}$ (see Figure 19b).

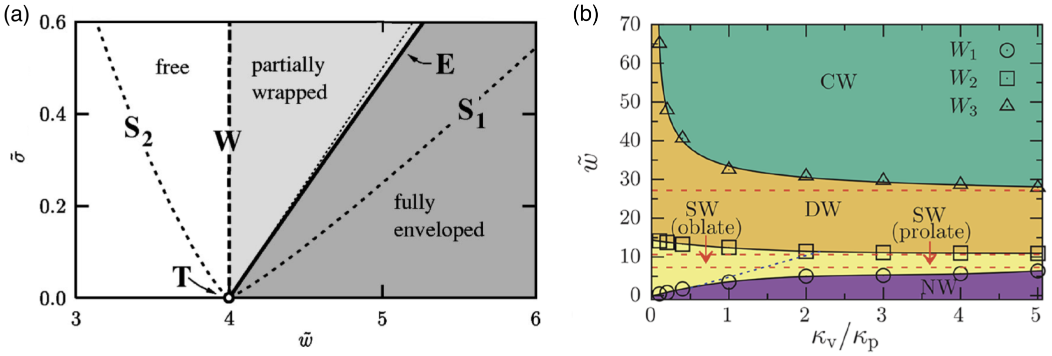

Figure 19. Wrapping diagrams for particles at initially planar membranes. (**a**) Diagram for a hard spherical particle in the plane of reduced adhesion strength $\tilde{w}$ and reduced membrane tension $\tilde{\sigma}$ close to the triple point T. The dashed line "W" marks the continuous transition at which partial wrapping sets in, the bold solid line "E" indicates the discontinuous transition between partially wrapped and fully enveloped, and the short dashed lines "S_1" and "S_2" are the spinodals belonging to "E". The fine dotted line $\tilde{w} = 4 + 2\tilde{\sigma}$ close to E indicates where the fully wrapped state has zero energy. Figure adapted with permission from Ref. [272]. Copyrighted by the American Physical Society. (**b**) Diagram for a prolate elastic particle modeled by a vesicle with reduced volume $v = 0.8$ at a membrane with reduced tension $\tilde{\sigma} = 0.5$ in the $\kappa_\mathrm{v}/\kappa_\mathrm{p}$-$\tilde{w}$-plane. Here, κ_v is the bending rigidity of the vesicle membrane and κ_p the bending rigidity of the initially planar membrane. The binding transition W_1 separates the non-wrapped (NW) from the shallow-wrapped (SW) regime, the transition W_2 the SW from the deep-wrapped (DW) regime, and the envelopment transition W_2 the DW from the complete-wrapped (CW) regime. The red-dashed lines indicate the wrapping transitions for a hard particle with reduced volume $v = 0.8$. Reprinted from Ref. [256]. CC BY 4.0.

For wrapping fluid biomolecular condensates, wrapping of a droplet may be a suitable model system. This system has been studied using aqueous phases of polymer solutions in vesicles, for which the importance of the difference between an intrinsic contact angle between the phases and an extrinsic contact angle observed in microscopy has been pointed out [273,274]. More recently, it has been shown that not only the condensate composition but also solution salinity [275] and membrane composition [276], such as the cholesterol content, affect the condensate–membrane interaction. The observed states are not limited to almost spherical and lens-shaped partial-wrapped condensates, but also include complete wetting of the membrane by the condensate [275,277].

4.4. Active Cellular Uptake Processes

Biological cells possess the machinery to take up drug-delivery vectors using active, metabolically driven processes. For example, cargo with sizes of ≈100 nm diameter can be taken up using clathrin-mediated endocytosis [278,279] (see Figure 20). Here, the binding of a clathrin coat assists the budding of the cell's plasma membrane and, therefore, cellular uptake. For cargo with sizes larger than ≈500 nm, active cellular uptake is mainly driven by active cytoskeletal processes [280,281], reported as early as 1967, where it was observed for the uptake of clusters of latex beads by Acanthamoeba [282]. For single particles, cytoskeleton-driven cellular uptake is most efficient for particle sizes of 2–3 µm diameter [79,80]. Phagocytosis—by phagocytes that are specialized for this process (e.g., macrophages and neutrophils)—is usually associated with solid, stiffer cargo [7,283–285]. Macropinocytosis, via macropinocytic cups, is not tied to a specific cell type and is usually associated with fluid cargo [286]. Recently, the uptake of micrometer-sized viscoelastic, glassy biomolecular condensates has been observed to integrate features of macropinocytosis and phagocytosis [112] (see Figure 21). The condensates have been shown not to translocate through the lipid bilayer using GUVs, and molecular inhibitors confirmed the role of active cytoskeletal remodeling in cellular uptake. After an incubation time of 15 min, some HB*pep* condensates were already attached to HeLa cells and surrounded by filopodia, whereas HB*pep*-SB condensates were almost completely engulfed . Furthermore, condensates "sinking" into the cells have been observed.

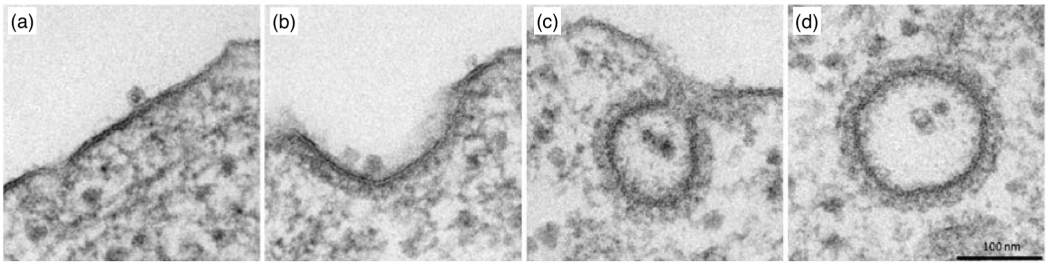

Figure 20. The endocytosis of the oncologic H-1 parovirus (H-1PV) is clathrin-dependent. HeLa cells were infected with H-1PV for 1 h at 4 °C to allow H-1PV cell surface attachment but not entry. Cells were then shifted to 37 °C to allow H-1PV cell internalization. The cells were collected every 5 min for a total of 30 min and processed for EM analysis. (**a**) At 4 °C, H-1PV particles are found attached to electro-dense (clathrin-rich) regions on the plasma membrane. (**b**) In the first 5 min after release at 37 °C, H-1PV particles are detected in early-forming clathrin-coated pits. (**c**) From 10 to 30 min, H-1PV particles moved into the cells within deeply invaginated clathrin-coated pits that were still connected to the plasma membrane, forming an hourglass-like membrane neck. (**d**) Later in the infection (10–30 min at 37 °C), H-1PV particles are seen being trafficked within the cell inside clathrin-coated vesicles. Reprinted from Ref. [278]. CC BY 4.0.

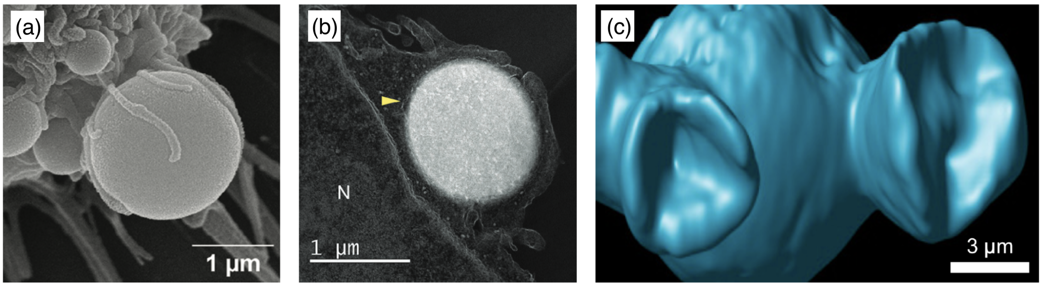

Figure 21. Cytoskeleton-driven active uptake processes. (**a**,**b**) Uptake of short histidine-rich, pH-responsive beak peptide (HB*pep*) coacervates by HeLa cells. (**a**) Filopodial capture visualized using scanning electron microscopy and (**b**) almost entirely engulfed HB*pep*-SP coacervates with an additional lysine residue, visualized via ultrathin sections of fixed and resin-embedded cells 15 min after incubation. The yellow arrow indicates the membrane around the condensate, and N the nucleus. Reprinted from Ref. [112]. CC BY 4.0. (**c**) Macropinocytic cups of dictyostelium obtained from a 3D-rendered fluorescent image. Reprinted from Ref. [286]. CC BY 4.0.

Data for several phagocytic cells suggest that stiffer particles are taken up faster, with a threshold Young's modulus beyond which cells recognize particles as hard [287]. Neutrophils, as a special case, have been found to effectively phagocytose elastic particles with a wide range of stiffnesses [288]. However, particle elasticity also affects other active cellular uptake pathways and may even be a decisive factor in determining which uptake pathway a cell uses. For example, hard hydrogel nanoparticles have been observed to be taken up by clathrin-mediated endocytosis, soft ones by macropinocytosis [6]. A different study shows that hard 100 nm particles are taken up by clathrin and caveolae-mediated endocytosis, while soft ones are taken up—much faster—by caveolae-mediated endocytosis and non-receptor-mediated endocytosis [289]. For tumor cells, a greater uptake of soft nanolipogels ($Y < 1.6\,\mathrm{MPa}$) over hard nanolipogels ($Y > 13.8\,\mathrm{MPa}$) has been reported, leading to the soft gels being deposited in the tumor and hard gels in the liver [99]. However, for polymeric drug-delivery vectors, the interactions with cells in vitro have been found to differ both by the elasticity of the carrier and the cell type, as shown in Ref. [290]. Whereas circulation times have consistently been found to be prolonged with increasing particle deformability, ambiguous results are reported for the dependence of cellular uptake by immune cells, cancer cells, and endothelial cells.

Active cellular uptake involves complex biological signalling and regulation, a detailed discussion of which is beyond the scope of this review article. Unlike for several passive uptake mechanisms, the mechanistic details of the active cellular uptake processes are often not yet well understood. A more detailed discussion of active cellular uptake processes can be found in Ref. [291] for clathrin-mediated endocytosis, in Ref. [292] for caveolae-mediated endocytosis, in Ref. [293–295] for phagocytosis, and in Ref. [293,296–298] for macropinocytosis.

5. Polymers In Vivo Relevant to Drug Delivery

Polymeric materials are not only used for designing synthetic drug-delivery vectors. Upon cellular uptake, the drug-delivery vectors and the drugs themselves interact with both the lipid-bilayer membranes and the polymeric materials in vivo, which affect cellular uptake and drug delivery. Examples include polymeric layers that act as barriers, such as the mucus in the lung [299], the mucous layer in the eye [300], the pericellular coat of chondrocytes [126], and the spectrin cytoskeleton of erythrocytes [301]. This may hinder cellular uptake. Biomolecular condensates, on the contrary, may serve as natural intracellular reservoirs for drugs. For example, it has been shown in vitro that antineoplastic drugs accumulate in specific condensates driven by physicochemical mechanisms independent of the drug target [302]. However, the subcellular distribution of small molecules in cells is condensate- and also cell-state-dependent; the drug sunitinib, which is used for cancer treatment, concentrates in nucleoli in interphase cells and in condensed chromatin during mitosis [303]. Therefore, in vivo, polymeric materials can act as barriers hindering the drug delivery, but in the form of intracellular biomolecular condensates, they can also directly regulate the concentration and activity of the drugs that have already been delivered to cells.

6. Summary

Polymeric materials are highly versatile and have been extensively studied both experimentally and theoretically. Plasma membranes of biological cells are lipid bilayers that serve as communication interfaces, allowing cells to exchange signals and materials with their environment. For applications as drug-delivery vectors, the polymeric materials have to cross the plasma membranes. In vivo and in vitro experiments quantify key observables, such as the circulation time and cellular uptake. Computer simulations help us to connect the molecular structures of delivery vectors with appropriate models on the scale of entire vectors. Here, coarse-grained and continuum models focusing on the key parameters that describe the elastic properties of polymeric drug-delivery vectors are more appropriate for building a systematic understanding of the relationship between delivery vectors and membranes than—usually computationally also unfeasible on the relevant scales—atomistic models.

Prominent architectures of polymeric and polymer composite drug-delivery vectors are linear chains, star polymers, polymer-grafted nanoparticles, polymersomes and stealth liposomes, nano- and microgels, and biomolecular condensates. Whereas linear polymer chains in good solvents have elongated shapes, star polymers, polymer-grafted nanoparticles, polymersomes, stealth liposomes, and nano- and microgels are often spherical colloids. The origins of their elastic properties are fundamentally different for the various architectures. For example, star polymers can be considered as fluid droplets because the arms can freely reorient; this fluidity is decreased for polymer-grafted nanoparticles, particularly for large core sizes and short polymers. Microgels have a finite shear modulus and can be modeled using continuum models with 3D elastic moduli. Fluid condensates can be modeled as droplets with an interface tension and bending rigidity determining their elasticity. Intriguingly, polymeric materials can be engineered to change size, shape, and elastic properties upon exposure to external stimuli, such as changes in temperature and pH.

Using vesicles as elastic model particles, the effects of particle deformability on wrapping and passive endocytosis have been systematically predicted. However, the complex molecular interactions between polymeric drug-delivery vectors and lipid-bilayer membranes are not entirely captured by such generic elastic-particle models. For example, the deformation energy of a gel with 3D elasticity scales differently with the particle size than an elastic shell with 2D elasticity. Furthermore, for linear chains, the importance of having appropriate hydrophobic–hydrophilic properties to allow them to translocate through lipid bilayers has been demonstrated. Therefore, considering the various specific structural and chemical properties—and, in particular, the origin of the elasticity—is required to understand the cellular uptake of polymeric delivery vectors.

7. Outlook

Combining information on the structural and elastic properties of drug-delivery vectors with quantitative experimental data on cellular uptake may in the future lead to an improved physico-chemical-informed design of polymeric and polymer-functionalized vectors. Polymer functionalization of materials also helps us to control their interactions with biological fluids, the formation of a protein corona, and thus the molecular interactions between drug-delivery vectors and biological cells.

The elastic properties of polymeric and polymer-functionalized materials can be tuned in a wide range of elasticities that are comparable to the elasticities of eukaryotic cells [304]. However, from the modeling point of view, our understanding of specific properties of polymeric materials in general is much more advanced than our understanding of their cellular uptake. For example, even for the passive wrapping of polymeric colloids with different architectures at lipid-bilayer membranes, such as microgels and star polymers, extensive mechanistic studies are missing. Another specific example is composite materials, such as condensates, which can encapsulate and deliver a large variety of cargo to cells. Cytoskeletal remodeling has been shown to be crucial for their active cellular uptake, and stiffer particles are usually taken up more readily. Furthermore, direct cytosolic delivery has been reported. Although the cellular uptake of microgels can be hypothesized as the wrapping of a soft particle with 3D elasticity, the observation that small and less crosslinked microgels are taken up significantly faster may also hint at translocation as a potential alternative uptake pathway [238]. Only very few mechanistic models address active cellular uptake mechanisms. A thorough understanding of several passive and most active uptake pathways—and what determines which uptake pathway is dominant—is thus still lacking for most delivery vectors. Systematic studies of specific delivery mechanisms for specific vectors may help to more effectively design polymeric drug-delivery vectors in the future.

Polymeric drug delivery vectors are unique because they can change their physicochemical properties upon exposure to external stimuli. Magnetically responsive condensates, for example, can be utilized in an alternating magnetic field for both controlled drug delivery and local heating [305]. Stimulus sensitivity can also help recruit and release drugs, as shown, e.g., for cargo recruitment by condensates triggered by temperature, pH, and ionic strength [306]. For drug loading, various methods including laser-induced phase transitions are available [307]. Within a cell, mainly a chemical sensitivity to pH or small molecules, such as condensate-modifying drugs [308], can be exploited to trigger drug release [309,310]. The stimulus sensitivity of physicochemical properties may also be important for modulating the vector–membrane interaction and, thus, cellular uptake. Furthermore, apart from direct cytosolic delivery, it is crucial to enable the drugs to escape from endosomes and lysosomes to the cytosol and make them available to the cells. Endosomal and lysosomal escape can be triggered by exploiting the pH responsiveness of polymeric materials [311–313]; for example, delivery vectors can swell or disintegrate in the acidic conditions found in lysosomes [312]. Condensates that lead to lysosome enlargement and permeability can even assemble only intracellularly [314]. Currently, the large variety of exciting possibilities that the stimulus-sensitivity of polymeric materials offers for applications in drug delivery awaits further characterization.

Finally, so far, most systematic mechanistic studies of model systems assume an interaction of drug-delivery vectors with lipid-bilayer membranes only. Although this provides important insights on vectors crossing the plasma membrane, in vivo, plasma membranes may have a polymer coat and be supported by a cortical cytoskeleton. Nuclear pore complexes, a gateway for macromolecules to the cell's nuclei, are decorated with polymeric nucleoporin structures. The implications of the interplay of these in vivo polymeric structures with polymeric drug-delivery vectors also require a systematic and quantitative bottom-up characterization.

Funding: This research received no external funding.

Data Availability Statement: No new data were created or analyzed in this study.

Conflicts of Interest: The author declares no conflicts of interest.

Abbreviations

The following abbreviations are used in this manuscript:

AFM	Atomic force microscopy
BIS	N,N′-methylenebis(acrylamide)
DMA	Dopamine methacrylamide
DNA	Deoxyribonucleic acid
DOPE	1,2-Dioleoyl-sn-glycero-3-phosphoethanolamine
FOCTS	Trichloro(1H,1H,2H,2H-perfluorooctyl)silane
GNP	Gold nanoparticles
GUV	Giant unilamellar vesicle
HEP	Heparin
HPMA	N-(2-Hydroxypropyl)methacrylamide (HPMA)
LCST	Lower critical solution temperature
LLPS	Liquid–liquid phase separation
MPS	Mononuclear phagocyte system
ODS	N-octadecyltrimethoxysilane
PAcM	Poly(N-acryloyl morpholine)
PDMA	Poly(N,N-dimethylacrylamide)
PEG	Polyethylene glycol
PEO	Polyethylene oxide
PG	Polypropylene glycol
PGN	Polymer-grafted (hairy) (nano-)particles
PNIPAM	Poly(N-isopropylacrylamide)

PNIPMAM	Poly(N-isopropylmethacrylamide)
POPC	1-palmitoyl-2-oleoyl-sn-glycero-3-phosphocholine
POPG	1-Palmitoyl-2-oleoyl-sn-glycero-3-phosphoglycerol
PVP	Poly(vinylpyrrolidone)
RES	Reticuloendothelial system
RNA	Ribonucleic acid
SCL	Self-crosslinked
UCST	Upper critical solution temperature
ULC	Ultra-low crosslinked
VPTT	Volume phase transition temperature
WCA	Weeks–Chandler–Andersen

References

1. Nifontova, G.; Tsoi, T.; Karaulov, A.; Nabiev, I.; Sukhanova, A. Structure–function relationships in polymeric multilayer capsules designed for cancer drug delivery. *Biomater. Sci.* **2022**, *10*, 5092–5115. [CrossRef] [PubMed]
2. Pérez-Ferreiro, M.; Abelairas, A.M.; Criado, A.; Gómez, I.J.; Mosquera, J. Dendrimers: Exploring Their Wide Structural Variety and Applications. *Polymers* **2023**, *15*, 4369. [CrossRef]
3. Chauhan, A.S. Dendrimers for Drug Delivery. *Molecules* **2018**, *23*, 938. [CrossRef] [PubMed]
4. Sun, J.; Zhang, L.; Wang, J.; Feng, Q.; Liu, D.; Yin, Q.; Xu, D.; Wei, Y.; Ding, B.; Shi, X.; et al. Tunable Rigidity of (Polymeric Core)–(Lipid Shell) Nanoparticles for Regulated Cellular Uptake. *Adv. Mater.* **2015**, *27*, 1402–1407. [CrossRef] [PubMed]
5. Liu, W.; Zhou, X.; Mao, Z.; Yu, D.; Wang, B.; Gao, C. Uptake of hydrogel particles with different stiffness and its influence on HepG2 cell functions. *Soft Matter* **2012**, *8*, 9235. [CrossRef]
6. Banquy, X.; Suarez, F.; Argaw, A.; Rabanel, J.M.; Grutter, P.; Bouchard, J.F.; Hildgen, P.; Giasson, S. Effect of mechanical properties of hydrogel nanoparticles on macrophage cell uptake. *Soft Matter* **2009**, *5*, 3984. [CrossRef]
7. Beningo, K.A.; Wang, Y.L. Fc-receptor-mediated phagocytosis is regulated by mechanical properties of the target. *J. Cell Sci.* **2002**, *115*, 849–856. [CrossRef]
8. Mayer, C.; Likos, C.N. A Coarse-Grained Description of Star-Linear Polymer Mixtures. *Macromolecules* **2007**, *40*, 1196–1206. [CrossRef]
9. Bedrov, D.; Ayyagari, C.; Smith, G.D. Multiscale Modeling of Poly(ethylene oxide)-Poly(propylene oxide)-Poly(ethylene oxide) Triblock Copolymer Micelles in Aqueous Solution. *J. Chem. Theory Comput.* **2006**, *2*, 598–606. [CrossRef]
10. Midya, J.; Rubinstein, M.; Kumar, S.K.; Nikoubashman, A. Structure of Polymer-Grafted Nanoparticle Melts. *ACS Nano* **2020**, *14*, 15505–15516. [CrossRef]
11. Nikolov, S.V.; Fernandez-Nieves, A.; Alexeev, A. Behavior and mechanics of dense microgel suspensions. *Proc. Natl. Acad. Sci. USA* **2020**, *117*, 27096–27103. [CrossRef]
12. Zhang, Y.; Fu, L.; Li, S.; Yan, J.; Sun, M.; Giraldo, J.P.; Matyjaszewski, K.; Tilton, R.D.; Lowry, G.V. Star Polymer Size, Charge Content, and Hydrophobicity Affect their Leaf Uptake and Translocation in Plants. *Environ. Sci. Technol.* **2021**, *55*, 10758–10768. [CrossRef]
13. Chen, Y.; Lord, M.S.; Piloni, A.; Stenzel, M.H. Correlation between Molecular Weight and Branch Structure of Glycopolymers Stars and Their Binding to Lectins. *Macromolecules* **2015**, *48*, 346–357. [CrossRef]
14. Georgiou, T.K.; Vamvakaki, M.; Patrickios, C.S.; Yamasaki, E.N.; Phylactou, L.A. Nanoscopic Cationic Methacrylate Star Homopolymers: Synthesis by Group Transfer Polymerization, Characterization and Evaluation as Transfection Reagents. *Biomacromolecules* **2004**, *5*, 2221–2229. [CrossRef] [PubMed]
15. Hedden, R.C.; Bauer, B.J. Structure and Dimensions of PAMAM/PEG Dendrimer-Star Polymers. *Macromolecules* **2003**, *36*, 1829–1835. [CrossRef]
16. Bagheri, M.; Bresseleers, J.; Varela-Moreira, A.; Sandre, O.; Meeuwissen, S.A.; Schiffelers, R.M.; Metselaar, J.M.; Van Nostrum, C.F.; Van Hest, J.C.M.; Hennink, W.E. Effect of Formulation and Processing Parameters on the Size of mPEG-*b*-p(HPMA-Bz) Polymeric Micelles. *Langmuir* **2018**, *34*, 15495–15506. [CrossRef]
17. Zinn, T.; Willner, L.; Lund, R.; Pipich, V.; Richter, D. Equilibrium exchange kinetics in n-alkyl–PEO polymeric micelles: Single exponential relaxation and chain length dependence. *Soft Matter* **2012**, *8*, 623–626. [CrossRef]
18. Forman-Kay, J.D.; Ditlev, J.A.; Nosella, M.L.; Lee, H.O. What are the distinguishing features and size requirements of biomolecular condensates and their implications for RNA-containing condensates? *RNA* **2022**, *28*, 36–47. [CrossRef]
19. Cochard, A.; Garcia-Jove Navarro, M.; Piroska, L.; Kashida, S.; Kress, M.; Weil, D.; Gueroui, Z. RNA at the surface of phase-separated condensates impacts their size and number. *Biophys. J.* **2022**, *121*, 1675–1690. [CrossRef]

20. Folkmann, A.W.; Putnam, A.; Lee, C.F.; Seydoux, G. Regulation of biomolecular condensates by interfacial protein clusters. *Science* **2021**, *373*, 1218–1224. [CrossRef]
21. Bonham, J.A.; Faers, M.A.; Van Duijneveldt, J.S. Non-aqueous microgel particles: Synthesis, properties and applications. *Soft Matter* **2014**, *10*, 9384–9398. [CrossRef]
22. Fox, T.L.; Tang, S.; Horton, J.M.; Holdaway, H.A.; Zhao, B.; Zhu, L.; Stewart, P.L. In Situ Characterization of Binary Mixed Polymer Brush-Grafted Silica Nanoparticles in Aqueous and Organic Solvents by Cryo-Electron Tomography. *Langmuir* **2015**, *31*, 8680–8688. [CrossRef]
23. He, C.; Hu, Y.; Yin, L.; Tang, C.; Yin, C. Effects of particle size and surface charge on cellular uptake and biodistribution of polymeric nanoparticles. *Biomaterials* **2010**, *31*, 3657–3666. [CrossRef]
24. Lv, S.; Liu, L.; Yang, W. Preparation of Soft Hydrogel Nanoparticles with PNIPAm Hair and Characterization of Their Temperature-Induced Aggregation. *Langmuir* **2010**, *26*, 2076–2082. [CrossRef]
25. Cui, F.; Qian, F.; Yin, C. Preparation and characterization of mucoadhesive polymer-coated nanoparticles. *Int. J. Pharm.* **2006**, *316*, 154–161. [CrossRef]
26. Rideau, E.; Dimova, R.; Schwille, P.; Wurm, F.R.; Landfester, K. Liposomes and polymersomes: A comparative review towards cell mimicking. *Chem. Soc. Rev.* **2018**, *47*, 8572–8610. [CrossRef] [PubMed]
27. Büber, E.; Schröder, T.; Scheckenbach, M.; Dass, M.; Franquelim, H.G.; Tinnefeld, P. DNA Origami Curvature Sensors for Nanoparticle and Vesicle Size Determination with Single-Molecule FRET Readout. *ACS Nano* **2023**, *17*, 3088–3097. [CrossRef] [PubMed]
28. Veneziano, R.; Moyer, T.J.; Stone, M.B.; Wamhoff, E.C.; Read, B.J.; Mukherjee, S.; Shepherd, T.R.; Das, J.; Schief, W.R.; Irvine, D.J.; et al. Role of nanoscale antigen organization on B-cell activation probed using DNA origami. *Nat. Nanotechnol.* **2020**, *15*, 716–723. [CrossRef] [PubMed]
29. Bastings, M.M.C.; Anastassacos, F.M.; Ponnuswamy, N.; Leifer, F.G.; Cuneo, G.; Lin, C.; Ingber, D.E.; Ryu, J.H.; Shih, W.M. Modulation of the Cellular Uptake of DNA Origami through Control over Mass and Shape. *Nano Lett.* **2018**, *18*, 3557–3564. [CrossRef]
30. Li, Z.; Wei, B.; Nangreave, J.; Lin, C.; Liu, Y.; Mi, Y.; Yan, H. A Replicable Tetrahedral Nanostructure Self-Assembled from a Single DNA Strand. *J. Am. Chem. Soc.* **2009**, *131*, 13093–13098. [CrossRef]
31. Sivadasan, D.; Sultan, M.H.; Madkhali, O.A.; Alsabei, S.H.; Alessa, A.A. Stealth Liposomes (PEGylated) Containing an Anticancer Drug Camptothecin: In Vitro Characterization and In Vivo Pharmacokinetic and Tissue Distribution Study. *Molecules* **2022**, *27*, 1086. [CrossRef] [PubMed]
32. Schmidt, S.; Zeiser, M.; Hellweg, T.; Duschl, C.; Fery, A.; Möhwald, H. Adhesion and Mechanical Properties of PNIPAM Microgel Films and Their Potential Use as Switchable Cell Culture Substrates. *Adv. Funct. Mater.* **2010**, *20*, 3235–3243. [CrossRef]
33. Strobl, G. *The Physics of Polymers: Concepts for Understanding Their Structures and Behaviour*, 3rd ed.; Springer: Berlin/Heidelberg, Germany, 2007.
34. de Gennes, P.G. *Scaling Concepts in Polymer Physics*, 1st ed.; Cornell University Press: New York, NY, USA, 1979.
35. Sherck, N.; Webber, T.; Brown, D.R.; Keller, T.; Barry, M.; DeStefano, A.; Jiao, S.; Segalman, R.A.; Fredrickson, G.H.; Shell, M.S.; et al. End-to-End Distance Probability Distributions of Dilute Poly(ethylene oxide) in Aqueous Solution. *J. Am. Chem. Soc.* **2020**, *142*, 19631–19641. [CrossRef]
36. Lee, H.; Venable, R.M.; MacKerell, A.D.; Pastor, R.W. Molecular Dynamics Studies of Polyethylene Oxide and Polyethylene Glycol: Hydrodynamic Radius and Shape Anisotropy. *Biophys. J.* **2008**, *95*, 1590–1599. [CrossRef] [PubMed]
37. Ahmed, Z.; Gooding, E.A.; Pimenov, K.V.; Wang, L.; Asher, S.A. UV Resonance Raman Determination of Molecular Mechanism of Poly(*N* -isopropylacrylamide) Volume Phase Transition. *J. Phys. Chem. B* **2009**, *113*, 4248–4256. [CrossRef]
38. Kubota, K.; Fujishige, S.; Ando, I. Solution Properties of Poly(N-isopropylacrylamide) in Water. *Polym. J.* **1990**, *22*, 15–20. [CrossRef]
39. Chen, H.; Meisburger, S.P.; Pabit, S.A.; Sutton, J.L.; Webb, W.W.; Pollack, L. Ionic strength-dependent persistence lengths of single-stranded RNA and DNA. *Proc. Natl. Acad. Sci. USA* **2012**, *109*, 799–804. [CrossRef] [PubMed]
40. Murphy, M.; Rasnik, I.; Cheng, W.; Lohman, T.M.; Ha, T. Probing Single-Stranded DNA Conformational Flexibility Using Fluorescence Spectroscopy. *Biophys. J.* **2004**, *86*, 2530–2537. [CrossRef]
41. Li, J.; Dao, M.; Lim, C.; Suresh, S. Spectrin-Level Modeling of the Cytoskeleton and Optical Tweezers Stretching of the Erythrocyte. *Biophys. J.* **2005**, *88*, 3707–3719. [CrossRef]
42. Garcia, H.G.; Grayson, P.; Han, L.; Inamdar, M.; Kondev, J.; Nelson, P.C.; Phillips, R.; Widom, J.; Wiggins, P.A. Biological consequences of tightly bent DNA: The other life of a macromolecular celebrity. *Biopolymers* **2007**, *85*, 115–130. [CrossRef]
43. Abels, J.; Moreno-Herrero, F.; Van Der Heijden, T.; Dekker, C.; Dekker, N. Single-Molecule Measurements of the Persistence Length of Double-Stranded RNA. *Biophys. J.* **2005**, *88*, 2737–2744. [CrossRef] [PubMed]
44. Ghavanloo, E. Persistence length of collagen molecules based on nonlocal viscoelastic model. *J. Biol. Phys.* **2017**, *43*, 525–534. [CrossRef] [PubMed]

45. Rölleke, U.; Kumari, P.; Meyer, R.; Köster, S. The unique biomechanics of intermediate filaments—From single filaments to cells and tissues. *Curr. Opin. Cell Biol.* **2023**, *85*, 102263. [CrossRef]
46. Gittes, F.; Mickey, B.; Nettleton, J.; Howard, J. Flexural rigidity of microtubules and actin filaments measured from thermal fluctuations in shape. *J. Cell Biol.* **1993**, *120*, 923–934. [CrossRef]
47. Pampaloni, F.; Lattanzi, G.; Jonáš, A.; Surrey, T.; Frey, E.; Florin, E.L. Thermal fluctuations of grafted microtubules provide evidence of a length-dependent persistence length. *Proc. Natl. Acad. Sci. USA* **2006**, *103*, 10248–10253. [CrossRef]
48. Porello, I.; Bono, N.; Candiani, G.; Cellesi, F. Advancing nucleic acid delivery through cationic polymer design: Non-cationic building blocks from the toolbox. *Polym. Chem.* **2024**, *15*, 2800–2826. [CrossRef]
49. Farshbaf, M.; Davaran, S.; Zarebkohan, A.; Annabi, N.; Akbarzadeh, A.; Salehi, R. Significant role of cationic polymers in drug delivery systems. *Artif. Cells Nanomed. Biotechnol.* **2017**, *46*, 1872–1891. [CrossRef]
50. Seror, J.; Zhu, L.; Goldberg, R.; Day, A.J.; Klein, J. Supramolecular synergy in the boundary lubrication of synovial joints. *Nat. Commun.* **2015**, *6*, 6497. [CrossRef]
51. Kim, J.U.; Matsen, M.W. Repulsion Exerted on a Spherical Particle by a Polymer Brush. *Macromolecules* **2008**, *41*, 246–252. [CrossRef]
52. Ruckenstein, E.; Li, B. Steric interactions between two grafted polymer brushes. *J. Chem. Phys.* **1997**, *107*, 932–942. [CrossRef]
53. Dietz, L.; Oberländer, J.; Mateos-Maroto, A.; Schunke, J.; Fichter, M.; Krämer-Albers, E.; Landfester, K.; Mailänder, V. Uptake of extracellular vesicles into immune cells is enhanced by the protein corona. *J. Extracell. Vesicles* **2023**, *12*, e12399. [CrossRef]
54. Zou, Y.; Ito, S.; Yoshino, F.; Suzuki, Y.; Zhao, L.; Komatsu, N. Polyglycerol Grafting Shields Nanoparticles from Protein Corona Formation to Avoid Macrophage Uptake. *ACS Nano* **2020**, *14*, 7216–7226. [CrossRef]
55. Wang, Y.; Ukwattage, V.; Xiong, Y.; Such, G.K. Advancing endosomal escape of polymeric nanoparticles: Towards improved intracellular delivery. *Mater. Horiz.* **2025**, *12*, 3622–3632. [CrossRef]
56. Vermeulen, L.M.; De Smedt, S.C.; Remaut, K.; Braeckmans, K. The proton sponge hypothesis: Fable or fact? *Eur. J. Pharm. Biopharm.* **2018**, *129*, 184–190. [CrossRef]
57. Hong, S.; Leroueil, P.R.; Janus, E.K.; Peters, J.L.; Kober, M.M.; Islam, M.T.; Orr, B.G.; Baker, J.R.; Banaszak Holl, M.M. Interaction of Polycationic Polymers with Supported Lipid Bilayers and Cells: Nanoscale Hole Formation and Enhanced Membrane Permeability. *Bioconjugate Chem.* **2006**, *17*, 728–734. [CrossRef] [PubMed]
58. Casper, J.; Schenk, S.H.; Parhizkar, E.; Detampel, P.; Dehshahri, A.; Huwyler, J. Polyethylenimine (PEI) in gene therapy: Current status and clinical applications. *J. Control. Release* **2023**, *362*, 667–691. [CrossRef]
59. Fischer, D.; Li, Y.; Ahlemeyer, B.; Krieglstein, J.; Kissel, T. In vitro cytotoxicity testing of polycations: Influence of polymer structure on cell viability and hemolysis. *Biomaterials* **2003**, *24*, 1121–1131. [CrossRef]
60. Kostyurina, E.; Allgaier, J.; Kruteva, M.; Frielinghaus, H.; Csiszár, A.; Förster, S.; Biehl, R. Passive Macromolecular Translocation Mechanism through Lipid Membranes. *J. Am. Chem. Soc.* **2022**, *144*, 15348–15354. [CrossRef] [PubMed]
61. Schneider, G.; Allgaier, J.; Fleury, J.B. Translocation of Synthetic Polymers by Lipid Membranes. WO 2018065583 A1, 12 April 2018.
62. Werner, M.; Sommer, J.U. Translocation and Induced Permeability of Random Amphiphilic Copolymers Interacting with Lipid Bilayer Membranes. *Biomacromolecules* **2015**, *16*, 125–135. [CrossRef] [PubMed]
63. Werner, M.; Sommer, J.U.; Baulin, V.A. Homo-polymers with balanced hydrophobicity translocate through lipid bilayers and enhance local solvent permeability. *Soft Matter* **2012**, *8*, 11714. [CrossRef]
64. Sommer, J.U.; Werner, M.; Baulin, V.A. Critical adsorption controls translocation of polymer chains through lipid bilayers and permeation of solvent. *EPL* **2012**, *98*, 18003. [CrossRef]
65. Cho, H.Y.; Gao, H.; Srinivasan, A.; Hong, J.; Bencherif, S.A.; Siegwart, D.J.; Paik, H.j.; Hollinger, J.O.; Matyjaszewski, K. Rapid Cellular Internalization of Multifunctional Star Polymers Prepared by Atom Transfer Radical Polymerization. *Biomacromolecules* **2010**, *11*, 2199–2203. [CrossRef]
66. Somers, K.; Wen, V.W.; Middlemiss, S.M.C.; Osborne, B.; Forgham, H.; Jung, M.; Karsa, M.; Clifton, M.; Bongers, A.; Gao, J.; et al. A novel small molecule that kills a subset of MLL-rearranged leukemia cells by inducing mitochondrial dysfunction. *Oncogene* **2019**, *38*, 3824–3842. [CrossRef]
67. Durmaz, Y.Y.; Lin, Y.; ElSayed, M.E.H. Development of Degradable, pH-Sensitive Star Vectors for Enhancing the Cytoplasmic Delivery of Nucleic Acids. *Adv. Funct. Mater.* **2013**, *23*, 3885–3895. [CrossRef]
68. Bayat, N.; McOrist, N.; Ariotti, N.; Lai, M.; Sia, K.C.; Li, Y.; Grace, J.L.; Quinn, J.F.; Whittaker, M.R.; Kavallaris, M.; et al. Thiol-Reactive Star Polymers Functionalized with Short Ethoxy-Containing Moieties Exhibit Enhanced Uptake in Acute Lymphoblastic Leukemia Cells. *Int. J. Nanomed.* **2019**, *14*, 9795–9808. [CrossRef] [PubMed]
69. Latorre, R.; Ramírez-Garcia, P.D.; Hegron, A.; Grace, J.L.; Retamal, J.S.; Shenoy, P.; Tran, M.; Aurelio, L.; Flynn, B.; Poole, D.P.; et al. Sustained endosomal release of a neurokinin-1 receptor antagonist from nanostars provides long-lasting relief of chronic pain. *Biomaterials* **2022**, *285*, 121536. [CrossRef]

70. Wang, H.; Chen, W.; Xie, H.; Wei, X.; Yin, S.; Zhou, L.; Xu, X.; Zheng, S. Biocompatible, chimeric peptide-condensed supramolecular nanoparticles for tumor cell-specific siRNA delivery and gene silencing. *Chem. Commun.* **2014**, *50*, 7806–7809. [CrossRef]
71. Wang, J.; Sun, J.; Chen, Q.; Gao, Y.; Li, L.; Li, H.; Leng, D.; Wang, Y.; Sun, Y.; Jing, Y.; et al. Star-shape copolymer of lysine-linked di-tocopherol polyethylene glycol 2000 succinate for doxorubicin delivery with reversal of multidrug resistance. *Biomaterials* **2012**, *33*, 6877–6888. [CrossRef] [PubMed]
72. Hu, J.; He, J.; Zhang, M.; Ni, P. Precise modular synthesis and a structure–property study of acid-cleavable star-block copolymers for pH-triggered drug delivery. *Polym. Chem.* **2015**, *6*, 1553–1566. [CrossRef]
73. Qiu, F.; Tu, C.; Wang, R.; Zhu, L.; Chen, Y.; Tong, G.; Zhu, B.; He, L.; Yan, D.; Zhu, X. Emission enhancement of conjugated polymers through self-assembly of unimolecular micelles to multi-micelle aggregates. *Chem. Commun.* **2011**, *47*, 9678. [CrossRef]
74. Hong, H.; Mai, Y.; Zhou, Y.; Yan, D.; Cui, J. Self-Assembly of Large Multimolecular Micelles from Hyperbranched Star Copolymers. *Macromol. Rapid Commun.* **2007**, *28*, 591–596. [CrossRef]
75. Mai, Y.; Zhou, Y.; Yan, D. Synthesis and Size-Controllable Self-Assembly of a Novel Amphiphilic Hyperbranched Multiarm Copolyether. *Macromolecules* **2005**, *38*, 8679–8686. [CrossRef]
76. Dutta, S.; Parida, S.; Maiti, C.; Banerjee, R.; Mandal, M.; Dhara, D. Polymer grafted magnetic nanoparticles for delivery of anticancer drug at lower pH and elevated temperature. *J. Colloid Interface Sci.* **2016**, *467*, 70–80. [CrossRef]
77. Paris, J.L.; Cabañas, M.V.; Manzano, M.; Vallet-Regí, M. Polymer-Grafted Mesoporous Silica Nanoparticles as Ultrasound-Responsive Drug Carriers. *ACS Nano* **2015**, *9*, 11023–11033. [CrossRef]
78. Kirchhausen, T.; Owen, D.; Harrison, S.C. Molecular Structure, Function, and Dynamics of Clathrin-Mediated Membrane Traffic. *Cold Spring Harb. Perspect. Biol.* **2014**, *6*, a016725. [CrossRef] [PubMed]
79. Champion, J.A.; Walker, A.; Mitragotri, S. Role of Particle Size in Phagocytosis of Polymeric Microspheres. *Pharm. Res.* **2008**, *25*, 1815–1821. [CrossRef] [PubMed]
80. Tabata, Y.; Ikada, Y. Effect of the size and surface charge of polymer microspheres on their phagocytosis by macrophage. *Biomaterials* **1988**, *9*, 356–362. [CrossRef]
81. Perrault, S.D.; Walkey, C.; Jennings, T.; Fischer, H.C.; Chan, W.C.W. Mediating Tumor Targeting Efficiency of Nanoparticles Through Design. *Nano Lett.* **2009**, *9*, 1909–1915. [CrossRef] [PubMed]
82. Nevozhay, D.; Rauch, R.; Wang, Z.; Sokolov, K.V. Optimal size and PEG coating of gold nanoparticles for prolonged blood circulation: A statistical analysis of published data. *Nanoscale Adv.* **2025**, *7*, 722–727. [CrossRef]
83. Discher, D.E.; Eisenberg, A. Polymer Vesicles. *Science* **2002**, *297*, 967–973. [CrossRef]
84. Klermund, L.; Poschenrieder, S.T.; Castiglione, K. Biocatalysis in Polymersomes: Improving Multienzyme Cascades with Incompatible Reaction Steps by Compartmentalization. *ACS Catal.* **2017**, *7*, 3900–3904. [CrossRef]
85. Otrin, L.; Marušič, N.; Bednarz, C.; Vidaković-Koch, T.; Lieberwirth, I.; Landfester, K.; Sundmacher, K. Toward Artificial Mitochondrion: Mimicking Oxidative Phosphorylation in Polymer and Hybrid Membranes. *Nano Lett.* **2017**, *17*, 6816–6821. [CrossRef] [PubMed]
86. Wen, P.; Dirisala, A.; Guo, H.; Liu, X.; Kobayashi, S.; Kinoh, H.; Anada, T.; Tanaka, M.; Kataoka, K.; Li, J. Engineering durable antioxidative nanoreactors as synthetic organelles for autoregulatory cellular protection against oxidative stress. *J. Control. Release* **2025**, *382*, 113683. [CrossRef]
87. Lomas, H.; Canton, I.; MacNeil, S.; Du, J.; Armes, S.; Ryan, A.; Lewis, A.; Battaglia, G. Biomimetic pH Sensitive Polymersomes for Efficient DNA Encapsulation and Delivery. *Adv. Mater.* **2007**, *19*, 4238–4243. [CrossRef]
88. Ahmed, F.; Pakunlu, R.I.; Brannan, A.; Bates, F.; Minko, T.; Discher, D.E. Biodegradable polymersomes loaded with both paclitaxel and doxorubicin permeate and shrink tumors, inducing apoptosis in proportion to accumulated drug. *J. Control. Release* **2006**, *116*, 150–158. [CrossRef]
89. Barbieri, V.; González Colsa, J.; Matias, D.; Duro Castano, A.; Thapa, A.; Ruiz-Pérez, L.; Albella, P.; Volpe, G.; Battaglia, G. Thermoplasmonic Polymersome Membranes by In Situ Synthesis. *ACS Nano* **2025**, *19*, 15331–15344. [CrossRef] [PubMed]
90. Bleher, S.; Buck, J.; Muhl, C.; Sieber, S.; Barnert, S.; Witzigmann, D.; Huwyler, J.; Barz, M.; Süss, R. Poly(Sarcosine) Surface Modification Imparts Stealth-Like Properties to Liposomes. *Small* **2019**, *15*, 1904716. [CrossRef] [PubMed]
91. Senior, J.; Delgado, C.; Fisher, D.; Tilcock, C.; Gregoriadis, G. Influence of surface hydrophilicity of liposomes on their interaction with plasma protein and clearance from the circulation: Studies with poly(ethylene glycol)-coated vesicles. *Biochim. Biophys. Acta, Biomembr.* **1991**, *1062*, 77–82. [CrossRef]
92. Woodle, M.C.; Newman, M.S.; Cohen, J.A. Sterically Stabilized Liposomes: Physical and Biological Properties. *J. Drug Target.* **1994**, *2*, 397–403. [CrossRef]
93. Sivakumaran, D.; Maitland, D.; Hoare, T. Injectable Microgel-Hydrogel Composites for Prolonged Small-Molecule Drug Delivery. *Biomacromolecules* **2011**, *12*, 4112–4120. [CrossRef]
94. Jiang, Y.; Chen, J.; Deng, C.; Suuronen, E.J.; Zhong, Z. Click hydrogels, microgels and nanogels: Emerging platforms for drug delivery and tissue engineering. *Biomaterials* **2014**, *35*, 4969–4985. [CrossRef]

95. Dave, R.; Randhawa, G.; Kim, D.; Simpson, M.; Hoare, T. Microgels and Nanogels for the Delivery of Poorly Water-Soluble Drugs. *Mol. Pharm.* **2022**, *19*, 1704–1721. [CrossRef]
96. Vinogradov, S. Colloidal Microgels in Drug Delivery Applications. *Curr. Pharm. Des.* **2006**, *12*, 4703–4712. [CrossRef] [PubMed]
97. Bysell, H.; Månsson, R.; Hansson, P.; Malmsten, M. Microgels and microcapsules in peptide and protein drug delivery. *Adv. Drug Deliv. Rev.* **2011**, *63*, 1172–1185. [CrossRef]
98. Saunders, B.R.; Laajam, N.; Daly, E.; Teow, S.; Hu, X.; Stepto, R. Microgels: From responsive polymer colloids to biomaterials. *Adv. Colloid Interface Sci.* **2009**, *147–148*, 251–262. [CrossRef]
99. Guo, P.; Liu, D.; Subramanyam, K.; Wang, B.; Yang, J.; Huang, J.; Auguste, D.T.; Moses, M.A. Nanoparticle elasticity directs tumor uptake. *Nat. Commun.* **2018**, *9*, 130. [CrossRef] [PubMed]
100. Lee, E.; Dang, L.N.; Choi, J.; Kim, H.; Bastatas, L.; Park, S. Elasticity-Driven Nanomechanical Interaction to Improve the Targeting Ability of Lipid Nanoparticles in the Malignant Tumor Microenvironment. *Adv. Sci.* **2025**, *12*, 2502073. [CrossRef] [PubMed]
101. Vanthienen, T.; Demeester, J.; Desmedt, S. Screening poly(ethyleneglycol) micro- and nanogels for drug delivery purposes. *Int. J. Pharm.* **2008**, *351*, 174–185. [CrossRef]
102. Wang, J.; Liu, Y.; Chen, R.; Zhang, Z.; Chen, G.; Chen, H. Ultralow Self-Cross-Linked Poly(*N*-isopropylacrylamide) Microgels Prepared by Solvent Exchange. *Langmuir* **2019**, *35*, 13991–13998. [CrossRef]
103. Scotti, A.; Brugnoni, M.; Lopez, C.G.; Bochenek, S.; Crassous, J.J.; Richtering, W. Flow properties reveal the particle-to-polymer transition of ultra-low crosslinked microgels. *Soft Matter* **2020**, *16*, 668–678. [CrossRef]
104. Bachman, H.; Brown, A.C.; Clarke, K.C.; Dhada, K.S.; Douglas, A.; Hansen, C.E.; Herman, E.; Hyat, J.S.; Kodlekere, P.; Meng, Z.; et al. Ultrasoft, highly deformable microgels. *Soft Matter* **2015**, *11*, 2018–2028. [CrossRef]
105. Douglas, A.M.; Fragkopoulos, A.A.; Gaines, M.K.; Lyon, L.A.; Fernandez-Nieves, A.; Barker, T.H. Dynamic assembly of ultrasoft colloidal networks enables cell invasion within restrictive fibrillar polymers. *Proc. Natl. Acad. Sci. USA* **2017**, *114*, 885–890. [CrossRef]
106. Brown, A.C.; Stabenfeldt, S.E.; Ahn, B.; Hannan, R.T.; Dhada, K.S.; Herman, E.S.; Stefanelli, V.; Guzzetta, N.; Alexeev, A.; Lam, W.A.; et al. Ultrasoft microgels displaying emergent platelet-like behaviours. *Nat. Mater.* **2014**, *13*, 1108–1114. [CrossRef]
107. Hirai, Y.; Kawaguchi, Y.; Kasahara, C.; Hirose, H.; Futaki, S. Liquid Droplet-Mediated Formulation of Lipid Nanoparticles Encapsulating Immunoglobulin G for Cytosolic Delivery. *Mol. Pharm.* **2024**, *21*, 1653–1661. [CrossRef] [PubMed]
108. Chen, K.; Liu, Y.; Duan, G.; Shi, M.; Yang, C.; Xing, R.; Yan, X. Biomolecular Condensates Based on Amino Acid for Enhancing Oral Bioavailability and Therapeutic Efficacy of Hydrophobic Drugs. *ACS Appl. Mater. Interfaces* **2024**, *16*, 58370–58378. [CrossRef] [PubMed]
109. Pyo, A.G.T.; Zhang, Y.; Wingreen, N.S. Proximity to criticality predicts surface properties of biomolecular condensates. *Proc. Natl. Acad. Sci. USA* **2023**, *120*, e2220014120. [CrossRef] [PubMed]
110. Ukmar-Godec, T.; Wegmann, S.; Zweckstetter, M. Biomolecular condensation of the microtubule-associated protein tau. *Semin. Cell Dev. Biol.* **2020**, *99*, 202–214. [CrossRef]
111. Chowdhury, P.; Saha, B.; Bauri, K.; Sumerlin, B.S.; De, P. Hydrogen Bonding-Driven Self-Coacervation of Nonionic Homopolymers for Stimuli-Triggered Therapeutic Release. *J. Am. Chem. Soc.* **2024**, *146*, 21664–21676. [CrossRef]
112. Shebanova, A.; Perrin, Q.M.; Zhu, K.; Gudlur, S.; Chen, Z.; Sun, Y.; Huang, C.; Lim, Z.W.; Mondarte, E.A.; Sun, R.; et al. Cellular Uptake of Phase-Separating Peptide Coacervates. *Adv. Sci.* **2024**, *11*, 2402652. [CrossRef]
113. Lu, T.; Hu, X.; Van Haren, M.H.I.; Spruijt, E.; Huck, W.T.S. Structure-Property Relationships Governing Membrane-Penetrating Behaviour of Complex Coacervates. *Small* **2023**, *19*, 2303138. [CrossRef]
114. Sun, Y.; Lau, S.Y.; Lim, Z.W.; Chang, S.C.; Ghadessy, F.; Partridge, A.; Miserez, A. Phase-separating peptides for direct cytosolic delivery and redox-activated release of macromolecular therapeutics. *Nat. Chem.* **2022**, *14*, 274–283. [CrossRef]
115. Panja, P.; Jana, N.R. Lipid-Raft-Mediated Direct Cytosolic Delivery of Polymer-Coated Soft Nanoparticles. *J. Phys. Chem. B* **2020**, *124*, 5323–5333. [CrossRef]
116. Son, J.; Jung, Y. Lipid coated protein condensates as stable protocells with selective uptake abilities for biomolecules. *Chem. Sci.* **2022**, *13*, 11841–11848. [CrossRef]
117. Theodorou, D.N.; Suter, U.W. Shape of unperturbed linear polymers: Polypropylene. *Macromolecules* **1985**, *18*, 1206–1214. [CrossRef]
118. Le Guillou, J.C.; Zinn-Justin, J. Critical Exponents for the n -Vector Model in Three Dimensions from Field Theory. *Phys. Rev. Lett.* **1977**, *39*, 95–98. [CrossRef]
119. Wei, Q.; Melko, R.G.; Chen, J.Z.Y. Identifying polymer states by machine learning. *Phys. Rev. E* **2017**, *95*, 032504. [CrossRef] [PubMed]
120. Schnabel, S.; Seaton, D.T.; Landau, D.P.; Bachmann, M. Microcanonical entropy inflection points: Key to systematic understanding of transitions in finite systems. *Phys. Rev. E* **2011**, *84*, 011127. [CrossRef] [PubMed]
121. Wöll, D. Fluorescence Correlation Spectroscopy Studies of Polymer Systems. In *Fluorescence Studies of Polymer Containing Systems*; Springer Series on Fluorescence; Springer International Publishing: Cham, Switzerland, 2016; Volume 16, pp. 256–297.

122. Doukas, A.K.; Likos, C.N.; Ziherl, P. Structure formation in soft nanocolloids: Liquid-drop model. *Soft Matter* **2018**, *14*, 3063–3072. [CrossRef]
123. Rajamani, S.; Truskett, T.M.; Garde, S. Hydrophobic hydration from small to large lengthscales: Understanding and manipulating the crossover. *Proc. Natl. Acad. Sci. USA* **2005**, *102*, 9475–9480. [CrossRef]
124. Willner, L.; Jucknischke, O.; Richter, D.; Farago, B.; Fetters, L.J.; Huang, J.S. Ordering Phenomena of Star Polymers in Solution by SANS. *Europhys. Lett.* **1992**, *19*, 297–303. [CrossRef]
125. Daoud, M.; Cotton, J. Star shaped polymers: A model for the conformation and its concentration dependence. *J. Phys. France* **1982**, *43*, 531–538. [CrossRef]
126. Cohen, M.; Klein, E.; Geiger, B.; Addadi, L. Organization and Adhesive Properties of the Hyaluronan Pericellular Coat of Chondrocytes and Epithelial Cells. *Biophys. J.* **2003**, *85*, 1996–2005. [CrossRef]
127. Allen, T.M.; Martin, F.J. Advantages of liposomal delivery systems for anthracyclines. *Semin. Oncol.* **2004**, *31*, 5–15. [CrossRef]
128. Bickel, T.; Marques, C.; Jeppesen, C. Grafted polymers are miniaturized pressure tools. *Comptes Rendus l'Académie Sci.—Ser. IV—Phys.* **2000**, *1*, 661–664. [CrossRef]
129. Werner, M.; Sommer, J.U. Polymer-decorated tethered membranes under good- and poor-solvent conditions. *Eur. Phys. J. E* **2010**, *31*, 383–392. [CrossRef]
130. Evans, A.R.; Turner, M.S.; Sens, P. Interactions between proteins bound to biomembranes. *Phys. Rev. E* **2003**, *67*, 041907. [CrossRef] [PubMed]
131. Bickel, T.; Jeppesen, C.; Marques, C. Local entropic effects of polymers grafted to soft interfaces. *Eur. Phys. J. E* **2001**, *4*, 33–43. [CrossRef]
132. Bickel, T.; Marques, C.; Jeppesen, C. Pressure patches for membranes: The induced pinch of a grafted polymer. *Phys. Rev. E* **2000**, *62*, 1124–1127. [CrossRef]
133. Auth, T.; Gompper, G. Fluctuation spectrum of membranes with anchored linear and star polymers. *Phys. Rev. E* **2005**, *72*, 031904. [CrossRef]
134. Auth, T.; Gompper, G. Self-avoiding linear and star polymers anchored to membranes. *Phys. Rev. E* **2003**, *68*, 051801. [CrossRef]
135. Bickel, T.; Marques, C. Scale-dependent rigidity of polymer-ornamented membranes. *Eur. Phys. J. E* **2002**, *9*, 349–352. [CrossRef]
136. Hiergeist, C.; Lipowsky, R. Elastic Properties of Polymer-Decorated Membranes. *J. Phys. II France* **1996**, *6*, 1465–1481. [CrossRef]
137. Discher, D.E.; Ahmed, F. Polymersomes. *Annu. Rev. Biomed. Eng.* **2006**, *8*, 323–341. [CrossRef]
138. Kostina, N.Y.; Rahimi, K.; Xiao, Q.; Haraszti, T.; Dedisch, S.; Spatz, J.P.; Schwaneberg, U.; Klein, M.L.; Percec, V.; Möller, M.; et al. Membrane-Mimetic Dendrimersomes Engulf Living Bacteria via Endocytosis. *Nano Lett.* **2019**, *19*, 5732–5738. [CrossRef]
139. Helfrich, W. Elastic Properties of Lipid Bilayers: Theory and Possible Experiments. *Z. Naturforsch. C* **1973**, *28*, 693–703. [CrossRef] [PubMed]
140. Gnan, N.; Rovigatti, L.; Bergman, M.; Zaccarelli, E. *In Silico* Synthesis of Microgel Particles. *Macromolecules* **2017**, *50*, 8777–8786. [CrossRef]
141. Strauch, C.; Schneider, S. Monte Carlo simulation of the ionization and uptake behavior of cationic oligomers into pH-responsive polyelectrolyte microgels of opposite charge—A model for oligopeptide uptake and release. *Soft Matter* **2024**, *20*, 1263–1274. [CrossRef]
142. Wilms, D.; Adler, Y.; Schröer, F.; Bunnemann, L.; Schmidt, S. Elastic modulus distribution in poly(*N* -isopopylacrylamide) and oligo(ethylene glycol methacrylate)-based microgels studied by AFM. *Soft Matter* **2021**, *17*, 5711–5717. [CrossRef]
143. Ninarello, A.; Crassous, J.J.; Paloli, D.; Camerin, F.; Gnan, N.; Rovigatti, L.; Schurtenberger, P.; Zaccarelli, E. Modeling Microgels with a Controlled Structure across the Volume Phase Transition. *Macromolecules* **2019**, *52*, 7584–7592. [CrossRef]
144. Boon, N.; Schurtenberger, P. Swelling of micro-hydrogels with a crosslinker gradient. *Phys. Chem. Chem. Phys.* **2017**, *19*, 23740–23746. [CrossRef] [PubMed]
145. Stieger, M.; Richtering, W.; Pedersen, J.S.; Lindner, P. Small-angle neutron scattering study of structural changes in temperature sensitive microgel colloids. *J. Chem. Phys.* **2004**, *120*, 6197–6206. [CrossRef]
146. Raßmann, N.; Trippmacher, S.; Specht, A.; Theis, K.; Rößler, T.; Wohlrab, S.; Kellnberger, R.; Salehi, S.; Bargel, H.; Helfricht, N.; et al. Determining the Elastic Modulus of Microgel Particles by Nanoindentation. *ACS Appl. Nano Mater.* **2025**, *8*, 5383–5398. [CrossRef]
147. Schulte, M.F.; Izak-Nau, E.; Braun, S.; Pich, A.; Richtering, W.; Göstl, R. Microgels react to force: Mechanical properties, syntheses, and force-activated functions. *Chem. Soc. Rev.* **2022**, *51*, 2939–2956. [CrossRef]
148. Kozlovskaya, V.; Dolmat, M.; Kharlampieva, E. Polymeric Particulates of Controlled Rigidity for Biomedical Applications. *ACS Appl. Polym. Mater.* **2021**, *3*, 2274–2289. [CrossRef]
149. Scheffold, F.; Díaz-Leyva, P.; Reufer, M.; Ben Braham, N.; Lynch, I.; Harden, J.L. Brushlike Interactions between Thermoresponsive Microgel Particles. *Phys. Rev. Lett.* **2010**, *104*. [CrossRef]
150. Scotti, A.; Schulte, M.F.; Lopez, C.G.; Crassous, J.J.; Bochenek, S.; Richtering, W. How Softness Matters in Soft Nanogels and Nanogel Assemblies. *Chem. Rev.* **2022**, *122*, 11675–11700. [CrossRef] [PubMed]

151. Hazra, N.; Ninarello, A.; Scotti, A.; Houston, J.E.; Mota-Santiago, P.; Zaccarelli, E.; Crassous, J.J. Structure of Responsive Microgels down to Ultralow Cross-Linkings. *Macromolecules* **2024**, *57*, 339–355. [CrossRef]
152. Scotti, A.; Bochenek, S.; Brugnoni, M.; Fernandez-Rodriguez, M.A.; Schulte, M.F.; Houston, J.E.; Gelissen, A.P.H.; Potemkin, I.I.; Isa, L.; Richtering, W. Exploring the colloid-to-polymer transition for ultra-low crosslinked microgels from three to two dimensions. *Nat. Commun.* **2019**, *10*, 1–8. [CrossRef]
153. Kot, M.; Nagahashi, H.; Szymczak, P. Elastic moduli of simple mass spring models. *Vis. Comput.* **2015**, *31*, 1339–1350. [CrossRef]
154. Lakes, R. Deformation mechanisms in negative Poisson's ratio materials: Structural aspects. *J. Mater. Sci.* **1991**, *26*, 2287–2292. [CrossRef]
155. Rovigatti, L.; Gnan, N.; Ninarello, A.; Zaccarelli, E. Connecting Elasticity and Effective Interactions of Neutral Microgels: The Validity of the Hertzian Model. *Macromolecules* **2019**, *52*, 4895–4906. [CrossRef]
156. Hazra, N.; Rudov, A.A.; Midya, J.; Babenyshev, A.; Bochenek, S.; Frenken, M.; Richtering, W.; Gompper, G.; Auth, T.; Potemkin, I.I.; et al. Capillary-driven self-assembly of soft ellipsoidal microgels at the air–water interface. *Proc. Natl. Acad. Sci. USA* **2024**, *121*, e2403690121. [CrossRef]
157. Liu, X.; Auth, T.; Hazra, N.; Ebbesen, M.F.; Brewer, J.; Gompper, G.; Crassous, J.J.; Sparr, E. Wrapping anisotropic microgel particles in lipid membranes: Effects of particle shape and membrane rigidity. *Proc. Natl. Acad. Sci. USA* **2023**, *120*, e2217534120. [CrossRef]
158. Burmistrova, A.; Richter, M.; Eisele, M.; Üzüm, C.; Von Klitzing, R. The Effect of Co-Monomer Content on the Swelling/Shrinking and Mechanical Behaviour of Individually Adsorbed PNIPAM Microgel Particles. *Polymers* **2011**, *3*, 1575–1590. [CrossRef]
159. Forg, S.; Guo, X.; Von Klitzing, R. Influence of Dopamine Methacrylamide on Swelling Behavior and Nanomechanical Properties of PNIPAM Microgels. *ACS Appl. Mater. Interfaces* **2024**, *16*, 1521–1534. [CrossRef] [PubMed]
160. McPhee, W.; Tam, K.C.; Pelton, R. Poly(N-isopropulacrylamide) Latices Prepared with Sodium Dodecyl Sulfate. *J. Colloid Interface Sci.* **1993**, *156*, 24–30. [CrossRef]
161. Halperin, A.; Kröger, M.; Winnik, F.M. Poly(*N*-isopropylacrylamide) Phase Diagrams: Fifty Years of Research. *Angew. Cheml Intl Edl* **2015**, *54*, 15342–15367. [CrossRef]
162. Heskins, M.; Guillet, J.E. Solution Properties of Poly(N-isopropylacrylamide). *J. Macromol. Sci.-Chem.* **1968**, *2*, 1441–1455. [CrossRef]
163. Virtanen, O.L.J.; Mourran, A.; Pinard, P.T.; Richtering, W. Persulfate initiated ultra-low cross-linked poly(N-isopropylacrylamide) microgels possess an unusual inverted cross-linking structure. *Soft Matter* **2016**, *12*, 3919–3928. [CrossRef]
164. Gao, J.; Frisken, B.J. Cross-Linker-Free *N*-Isopropylacrylamide Gel Nanospheres. *Langmuir* **2003**, *19*, 5212–5216. [CrossRef]
165. Gao, J.; Frisken, B.J. Influence of Reaction Conditions on the Synthesis of Self-Cross-Linked *N*-Isopropylacrylamide Microgels. *Langmuir* **2003**, *19*, 5217–5222. [CrossRef]
166. Varga, I.; Gilányi, T.; Mészáros, R.; Filipcsei, G.; Zrínyi, M. Effect of Cross-Link Density on the Internal Structure of Poly(*N*-isopropylacrylamide) Microgels. *J. Phys. Chem. B* **2001**, *105*, 9071–9076. [CrossRef]
167. Brugnoni, M.; Nickel, A.C.; Kröger, L.C.; Scotti, A.; Pich, A.; Leonhard, K.; Richtering, W. Synthesis and structure of deuterated ultra-low cross-linked poly(*N*-isopropylacrylamide) microgels. *Polym. Chem.* **2019**, *10*, 2397–2405. [CrossRef]
168. Schulte, M.F.; Scotti, A.; Brugnoni, M.; Bochenek, S.; Mourran, A.; Richtering, W. Tuning the Structure and Properties of Ultra-Low Cross-Linked Temperature-Sensitive Microgels at Interfaces via the Adsorption Pathway. *Langmuir* **2019**, *35*, 14769–14781. [CrossRef] [PubMed]
169. Vilgis, T.; Stapper, M. Microgels and fractal structures at interfaces and surfaces. *Eur. Phys. J. B* **1998**, *2*, 69–74. [CrossRef]
170. Schulte, M.F.; Bochenek, S.; Brugnoni, M.; Scotti, A.; Mourran, A.; Richtering, W. Stiffness Tomography of Ultra-Soft Nanogels by Atomic Force Microscopy. *Angew. Chem. Int. Ed.* **2021**, *60*, 2280–2287. [CrossRef] [PubMed]
171. Tennenbaum, M.; Anderson, C.; Hyatt, J.S.; Do, C.; Fernandez-Nieves, A. Internal structure of ultralow-crosslinked microgels: From uniform deswelling to phase separation. *Phys. Rev. E* **2021**, *103*. [CrossRef]
172. Islam, M.R.; Tumbarello, M.; Lyon, L.A. Deswelling induced morphological changes in dual pH- and temperature-responsive ultra-low cross-linked poly(N-isopropyl acrylamide)-co-acrylic acid microgels. *Colloid Polym. Sci.* **2019**, *297*, 667–676. [CrossRef] [PubMed]
173. Berndt, I.; Pedersen, J.S.; Richtering, W. Structure of Multiresponsive "Intelligent" Core-Shell Microgels. *J. Am. Chem. Soc.* **2005**, *127*, 9372–9373. [CrossRef]
174. Brugnoni, M.; Fink, F.; Scotti, A.; Richtering, W. Synthesis and structure of temperature-sensitive nanocapsules. *Colloid Polym. Sci.* **2020**, *298*, 1179–1185. [CrossRef]
175. Crassous, J.J.; Mihut, A.M.; Månsson, L.K.; Schurtenberger, P. Anisotropic responsive microgels with tuneable shape and interactions. *Nanoscale* **2015**, *7*, 15971–15982. [CrossRef]
176. Wypysek, S.K.; Centeno, S.P.; Gronemann, T.; Wöll, D.; Richtering, W. Hollow, pH-Sensitive Microgels as Nanocontainers for the Encapsulation of Proteins. *Macromol. Biosci.* **2023**, *23*, 2200456. [CrossRef]

177. Islam, M.R.; Lyon, L.A. Deswelling studies of pH and temperature-sensitive ultra-low cross-linked microgels with cross-linked cores. *Colloid Polym. Sci.* **2020**, *298*, 395–405. [CrossRef]
178. Kozhunova, E.Y.; Vyshivannaya, O.V.; Nasimova, I.R. "Smart" IPN microgels with different network structures: Self-crosslinked vs. conventionally crosslinked. *Polymer* **2019**, *176*, 127–134. [CrossRef]
179. Rudyak, V.Y.; Gavrilov, A.A.; Kozhunova, E.Y.; Chertovich, A.V. Shell–corona microgels from double interpenetrating networks. *Soft Matter* **2018**, *14*, 2777–2781. [CrossRef]
180. Bungenberg de Jong, H.G.; Kruyt, H.R. Koazervation. *Koloid Z.* **1930**, *50*, 39–48. [CrossRef]
181. Semenov, A.N.; Rubinstein, M. Thermoreversible Gelation in Solutions of Associative Polymers. 1. Statics. *Macromolecules* **1998**, *31*, 1373–1385. [CrossRef]
182. Shin, Y.; Brangwynne, C.P. Liquid phase condensation in cell physiology and disease. *Science* **2017**, *357*, eaaf4382. [CrossRef]
183. Brangwynne, C.P.; Eckmann, C.R.; Courson, D.S.; Rybarska, A.; Hoege, C.; Gharakhani, J.; Jülicher, F.; Hyman, A.A. Germline P Granules Are Liquid Droplets That Localize by Controlled Dissolution/Condensation. *Science* **2009**, *324*, 1729–1732. [CrossRef]
184. Lee, D.S.W.; Choi, C.H.; Sanders, D.W.; Beckers, L.; Riback, J.A.; Brangwynne, C.P.; Wingreen, N.S. Size distributions of intracellular condensates reflect competition between coalescence and nucleation. *Nat. Phys.* **2023**, *19*, 586–596. [CrossRef]
185. Liu, L.; Xu, Y.; Zhang, P.; You, J.; Li, W.; Chen, Y.; Li, R.; Rui, B.; Dou, H. High-Order Assembly toward Polysaccharide-Based Complex Coacervate Nanodroplets Capable of Targeting Cancer Cells. *Langmuir* **2020**, *36*, 8580–8588. [CrossRef] [PubMed]
186. Ambadi Thody, S.; Clements, H.D.; Baniasadi, H.; Lyon, A.S.; Sigman, M.S.; Rosen, M.K. Small-molecule properties define partitioning into biomolecular condensates. *Nat. Chem.* **2024**, *16*, 1794–1802. [CrossRef] [PubMed]
187. McInnes, L.; Healy, J.; Melville, J. UMAP: Uniform Manifold Approximation and Projection for Dimension Reduction. *arXiv* **2020**, arXiv:1802.03426. [CrossRef]
188. *QikProp Release 2022-4*; Schrödinger LLC: New York, NY, USA, 2021.
189. Banani, S.F.; Rice, A.M.; Peeples, W.B.; Lin, Y.; Jain, S.; Parker, R.; Rosen, M.K. Compositional Control of Phase-Separated Cellular Bodies. *Cell* **2016**, *166*, 651–663. [CrossRef]
190. Kilgore, H.R.; Young, R.A. Learning the chemical grammar of biomolecular condensates. *Nat. Chem. Biol.* **2022**, *18*, 1298–1306. [CrossRef]
191. Li, R.; Yang, X.; Chen, S.; Chen, H.; Lin, L.; Chen, Y.; Xiao, J.; Ma, Y.; Li, W. Engineering DNA Condensate Droplets as a Versatile Nanovector. *Nano Lett.* **2025**, *25*, 10225–10232. [CrossRef]
192. Kelley, F.M.; Ani, A.; Pinlac, E.G.; Linders, B.; Favetta, B.; Barai, M.; Ma, Y.; Singh, A.; Dignon, G.L.; Gu, Y.; et al. Controlled and orthogonal partitioning of large particles into biomolecular condensates. *Nat. Commun.* **2025**, *16*, 3521. [CrossRef]
193. Schmidt, H.; Putnam, A.; Rasoloson, D.; Seydoux, G. Protein-based condensation mechanisms drive the assembly of RNA-rich P granules. *eLife* **2021**, *10*, e63698. [CrossRef]
194. Zhang, Y.; Li, S.; Gong, X.; Chen, J. Toward Accurate Simulation of Coupling between Protein Secondary Structure and Phase Separation. *J. Am. Chem. Soc.* **2024**, *146*, 342–357. [CrossRef]
195. Schneider, M.W.G.; Gibson, B.A.; Otsuka, S.; Spicer, M.F.D.; Petrovic, M.; Blaukopf, C.; Langer, C.C.H.; Batty, P.; Nagaraju, T.; Doolittle, L.K.; et al. A mitotic chromatin phase transition prevents perforation by microtubules. *Nature* **2022**, *609*, 183–190. [CrossRef] [PubMed]
196. Su, X.; Ditlev, J.A.; Hui, E.; Xing, W.; Banjade, S.; Okrut, J.; King, D.S.; Taunton, J.; Rosen, M.K.; Vale, R.D. Phase separation of signaling molecules promotes T cell receptor signal transduction. *Science* **2016**, *352*, 595–599. [CrossRef] [PubMed]
197. Sanders, D.W.; Kedersha, N.; Lee, D.S.; Strom, A.R.; Drake, V.; Riback, J.A.; Bracha, D.; Eeftens, J.M.; Iwanicki, A.; Wang, A.; et al. Competing Protein-RNA Interaction Networks Control Multiphase Intracellular Organization. *Cell* **2020**, *181*, 306–324.e28. [CrossRef]
198. Nakashima, K.K.; Van Haren, M.H.I.; André, A.A.M.; Robu, I.; Spruijt, E. Active coacervate droplets are protocells that grow and resist Ostwald ripening. *Nat. Commun.* **2021**, *12*, 3819. [CrossRef]
199. Jambon-Puillet, E.; Testa, A.; Lorenz, C.; Style, R.W.; Rebane, A.A.; Dufresne, E.R. Phase-separated droplets swim to their dissolution. *Nat. Commun.* **2024**, *15*, 3919. [CrossRef] [PubMed]
200. Li, Y.; Xu, T.; Li, Y.; Wang, H. Enzyme Induced Solid-Like Condensates Formation of Engineered Peptide in Living Cells for Prostate Cancer Inhibition. *Angew. Chem. Int. Ed.* **2025**, *64*, e202504958. [CrossRef]
201. Aarts, D.G.A.L.; Dullens, R.P.A.; Lekkerkerker, H.N.W.; Bonn, D.; Van Roij, R. Interfacial tension and wetting in colloid–polymer mixtures. *J. Chem. Phys.* **2004**, *120*, 1973–1980. [CrossRef]
202. Holland, J.; Castrejón-Pita, A.A.; Tuinier, R.; Aarts, D.G.A.L.; Nott, T.J. Surface tension measurement and calculation of model biomolecular condensates. *Soft Matter* **2023**, *19*, 8706–8716. [CrossRef]
203. Wang, H.; Kelley, F.M.; Milovanovic, D.; Schuster, B.S.; Shi, Z. Surface tension and viscosity of protein condensates quantified by micropipette aspiration. *Biophys. Rep.* **2021**, *1*, 100011. [CrossRef]

204. Law, J.O.; Jones, C.M.; Stevenson, T.; Williamson, T.A.; Turner, M.S.; Kusumaatmaja, H.; Grellscheid, S.N. A bending rigidity parameter for stress granule condensates. *Sci. Adv.* **2023**, *9*, eadg0432. [CrossRef] [PubMed]
205. Alshareedah, I.; Thurston, G.M.; Banerjee, P.R. Quantifying viscosity and surface tension of multicomponent protein-nucleic acid condensates. *Biophys. J.* **2021**, *120*, 1161–1169. [CrossRef]
206. Jawerth, L.; Fischer-Friedrich, E.; Saha, S.; Wang, J.; Franzmann, T.; Zhang, X.; Sachweh, J.; Ruer, M.; Ijavi, M.; Saha, S.; et al. Protein condensates as aging Maxwell fluids. *Science* **2020**, *370*, 1317–1323. [CrossRef]
207. Kota, D.; Zhou, H.X. Macromolecular Regulation of the Material Properties of Biomolecular Condensates. *J. Phys. Chem. Lett.* **2022**, *13*, 5285–5290. [CrossRef]
208. Jawerth, L.M.; Ijavi, M.; Ruer, M.; Saha, S.; Jahnel, M.; Hyman, A.A.; Jülicher, F.; Fischer-Friedrich, E. Salt-Dependent Rheology and Surface Tension of Protein Condensates Using Optical Traps. *Phys. Rev. Lett.* **2018**, *121*, 258101. [CrossRef]
209. Caragine, C.M.; Haley, S.C.; Zidovska, A. Surface Fluctuations and Coalescence of Nucleolar Droplets in the Human Cell Nucleus. *Phys. Rev. Lett.* **2018**, *121*, 148101. [CrossRef] [PubMed]
210. Santamaria, A.; Hutin, S.; Doucet, C.M.; Zubieta, C.; Milhiet, P.E.; Costa, L. Quantifying surface tension and viscosity in biomolecular condensates by FRAP-ID. *Biophys. J.* **2024**, *123*, 3366–3374. [CrossRef]
211. Shimobayashi, S.F.; Konishi, K.; Ackerman, P.J.; Taniguchi, T.; Brangwynne, C.P. Critical capillary waves of biomolecular condensates. *bioRxiv* **2023**. [CrossRef]
212. Pickering, S.U. Emulsions. *J. Chem. Soc. Trans.* **1907**, *91*, 2001–2021. [CrossRef]
213. Oh, H.J.; Lee, Y.; Hwang, H.; Hong, K.; Choi, H.; Kang, J.Y.; Jung, Y. Size-controlled assembly of phase separated protein condensates with interfacial protein cages. *Nat. Commun.* **2025**, *16*, 1009. [CrossRef]
214. Cai, D.; Feliciano, D.; Dong, P.; Flores, E.; Gruebele, M.; Porat-Shliom, N.; Sukenik, S.; Liu, Z.; Lippincott-Schwartz, J. Phase separation of YAP reorganizes genome topology for long-term YAP target gene expression. *Nat. Cell Biol.* **2019**, *21*, 1578–1589. [CrossRef] [PubMed]
215. Wen, P.; Ke, W.; Dirisala, A.; Toh, K.; Tanaka, M.; Li, J. Stealth and pseudo-stealth nanocarriers. *Adv. Drug Deliv. Rev.* **2023**, *198*, 114895. [CrossRef]
216. Yoo, J.W.; Chambers, E.; Mitragotri, S. Factors that Control the Circulation Time of Nanoparticles in Blood: Challenges, Solutions and Future Prospects. *Curr. Pharm. Des.* **2010**, *16*, 2298–2307. [CrossRef]
217. Sheng, Y.; Chang, L.; Kuang, T.; Hu, J. PEG/heparin-decorated lipid–polymer hybrid nanoparticles for long-circulating drug delivery. *RSC Adv.* **2016**, *6*, 23279–23287. [CrossRef]
218. Est-Witte, S.E.; Shannon, S.R.; Gong, D.H.; Calabresi, K.G.; Harris, J.J.; Storm, K.; Yoo, E.J.; Isser, A.; Jani, V.P.; Livingston, N.K.; et al. Particle elasticity influences polymeric artificial antigen presenting cell effectiveness in vivo via CD8+ T cell activation, macrophage uptake, and the protein corona. *Nano Res.* **2024**, *17*, 9052–9064. [CrossRef]
219. Kierstead, P.H.; Okochi, H.; Venditto, V.J.; Chuong, T.C.; Kivimae, S.; Fréchet, J.M.; Szoka, F.C. The effect of polymer backbone chemistry on the induction of the accelerated blood clearance in polymer modified liposomes. *J. Control. Release* **2015**, *213*, 1–9. [CrossRef]
220. Son, K.; Ueda, M.; Taguchi, K.; Maruyama, T.; Takeoka, S.; Ito, Y. Evasion of the accelerated blood clearance phenomenon by polysarcosine coating of liposomes. *J. Control. Release* **2020**, *322*, 209–216. [CrossRef]
221. Mohamed, M.; Abu Lila, A.S.; Shimizu, T.; Alaaeldin, E.; Hussein, A.; Sarhan, H.A.; Szebeni, J.; Ishida, T. PEGylated liposomes: Immunological responses. *Sci. Technol. Adv. Mater.* **2019**, *20*, 710–724. [CrossRef]
222. Ishida, T.; Atobe, K.; Wang, X.; Kiwada, H. Accelerated blood clearance of PEGylated liposomes upon repeated injections: Effect of doxorubicin-encapsulation and high-dose first injection. *J. Control. Release* **2006**, *115*, 251–258. [CrossRef]
223. Müller, K.; Fedosov, D.A.; Gompper, G. Understanding particle margination in blood flow—A step toward optimized drug delivery systems. *Med. Eng. Phys.* **2016**, *38*, 2–10. [CrossRef]
224. Müller, K.; Fedosov, D.A.; Gompper, G. Margination of micro- and nano-particles in blood flow and its effect on drug delivery. *Sci. Rep.* **2014**, *4*, 4871. [CrossRef] [PubMed]
225. Anselmo, A.C.; Zhang, M.; Kumar, S.; Vogus, D.R.; Menegatti, S.; Helgeson, M.E.; Mitragotri, S. Elasticity of Nanoparticles Influences Their Blood Circulation, Phagocytosis, Endocytosis, and Targeting. *ACS Nano* **2015**, *9*, 3169–3177. [CrossRef]
226. Desai, P.; Rimal, R.; Florea, A.; Gumerov, R.A.; Santi, M.; Sorokina, A.S.; Sahnoun, S.E.M.; Fischer, T.; Mottaghy, F.M.; Morgenroth, A.; et al. Tuning the Elasticity of Nanogels Improves Their Circulation Time by Evading Immune Cells. *Angew. Chem. Int. Ed.* **2022**, *61*, e202116653. [CrossRef] [PubMed]
227. Anraku, Y.; Kishimura, A.; Oba, M.; Yamasaki, Y.; Kataoka, K. Spontaneous Formation of Nanosized Unilamellar Polyion Complex Vesicles with Tunable Size and Properties. *J. Am. Chem. Soc.* **2010**, *132*, 1631–1636. [CrossRef]
228. Merkel, T.J.; Chen, K.; Jones, S.W.; Pandya, A.A.; Tian, S.; Napier, M.E.; Zamboni, W.E.; DeSimone, J.M. The effect of particle size on the biodistribution of low-modulus hydrogel PRINT particles. *J. Control. Release* **2012**, *162*, 37–44. [CrossRef]

229. Merkel, T.J.; Jones, S.W.; Herlihy, K.P.; Kersey, F.R.; Shields, A.R.; Napier, M.; Luft, J.C.; Wu, H.; Zamboni, W.C.; Wang, A.Z.; et al. Using mechanobiological mimicry of red blood cells to extend circulation times of hydrogel microparticles. *Proc. Natl. Acad. Sci. USA* **2011**, *108*, 586–591. [CrossRef]
230. Haghgooie, R.; Toner, M.; Doyle, P.S. Squishy Non-Spherical Hydrogel Microparticles. *Macromol. Rapid Commun.* **2010**, *31*, 128–134. [CrossRef]
231. Barbul, A.; Singh, K.; Horev-Azaria, L.; Dasgupta, S.; Auth, T.; Korenstein, R.; Gompper, G. Nanoparticle-Decorated Erythrocytes Reveal That Particle Size Controls the Extent of Adsorption, Cell Shape, and Cell Deformability. *ACS Appl. Nano Mater.* **2018**, *1*, 3785–3799. [CrossRef]
232. Sosale, N.G.; Rouhiparkouhi, T.; Bradshaw, A.M.; Dimova, R.; Lipowsky, R.; Discher, D.E. Cell rigidity and shape override CD47's "self"-signaling in phagocytosis by hyperactivating myosin-II. *Blood* **2015**, *125*, 542–552. [CrossRef]
233. Goswami, R.; Jeon, T.; Nagaraj, H.; Zhai, S.; Rotello, V.M. Accessing Intracellular Targets through Nanocarrier-Mediated Cytosolic Protein Delivery. *Trends Pharmacol. Sci.* **2020**, *41*, 743–754. [CrossRef] [PubMed]
234. Du, S.; Liew, S.S.; Li, L.; Yao, S.Q. Bypassing Endocytosis: Direct Cytosolic Delivery of Proteins. *J. Am. Chem. Soc.* **2018**, *140*, 15986–15996. [CrossRef] [PubMed]
235. Vácha, R.; Martinez-Veracoechea, F.J.; Frenkel, D. Receptor-Mediated Endocytosis of Nanoparticles of Various Shapes. *Nano Lett.* **2011**, *11*, 5391–5395. [CrossRef]
236. Le Bihan, O.; Bonnafous, P.; Marak, L.; Bickel, T.; Trépout, S.; Mornet, S.; De Haas, F.; Talbot, H.; Taveau, J.C.; Lambert, O. Cryo-electron tomography of nanoparticle transmigration into liposome. *J. Struct. Biol.* **2009**, *168*, 419–425. [CrossRef] [PubMed]
237. Canton, I.; Battaglia, G. Endocytosis at the nanoscale. *Chem. Soc. Rev.* **2012**, *41*, 2718. [CrossRef]
238. Switacz, V.K.; Wypysek, S.K.; Degen, R.; Crassous, J.J.; Spehr, M.; Richtering, W. Influence of Size and Cross-Linking Density of Microgels on Cellular Uptake and Uptake Kinetics. *Biomacromolecules* **2020**, *21*, 4532–4544. [CrossRef]
239. Sun, Y.; Wu, X.; Li, J.; Radiom, M.; Mezzenga, R.; Verma, C.S.; Yu, J.; Miserez, A. Phase-separating peptide coacervates with programmable material properties for universal intracellular delivery of macromolecules. *Nat. Commun.* **2024**, *15*, 10094. [CrossRef]
240. Liang, T.; Dong, Y.; Cheng, I.; Wen, P.; Li, F.; Liu, F.; Wu, Q.; Ren, E.; Liu, P.; Li, H.; et al. In situ formation of biomolecular condensates as intracellular drug reservoirs for augmenting chemotherapy. *Nat. Biomed. Eng.* **2024**, *8*, 1469–1482. [CrossRef] [PubMed]
241. Baumgärtner, A.; Skolnick, J. Spontaneous Translocation of a Polymer across a Curved Membrane. *Phys. Rev. Lett.* **1995**, *74*, 2142–2145. [CrossRef]
242. Muthukumar, M.; Baumgaertner, A. Effects of entropic barriers on polymer dynamics. *Macromolecules* **1989**, *22*, 1937–1941. [CrossRef]
243. Polson, J.M.; Dunn, T. Evaluating the Applicability of the Fokker-Planck Equation in Polymer Translocation: A Brownian Dynamics Study. *J. Chem. Phys.* **2014**, *140*, 184904. [CrossRef]
244. Song, X.; Ma, J.; Long, T.; Xu, X.; Zhao, S.; Liu, H. Mechanochemical Cellular Membrane Internalization of Nanohydrogels: A Large-Scale Mesoscopic Simulation. *ACS Appl. Mater. Interfaces* **2021**, *13*, 123–134. [CrossRef]
245. Hoppe Alvarez, L.; Eisold, S.; Gumerov, R.A.; Strauch, M.; Rudov, A.A.; Lenssen, P.; Merhof, D.; Potemkin, I.I.; Simon, U.; Wöll, D. Deformation of Microgels at Solid–Liquid Interfaces Visualized in Three-Dimension. *Nano Lett.* **2019**, *19*, 8862–8867. [CrossRef] [PubMed]
246. Debnath, T. (Forschungszentrum Jülich, Jülich, Germany); Midya, J. (Indian Institute of Technology, Bhubaneswar, India); Gompper, G. (Forschungszentrum Jülich, Jülich, Germany). Personal communication, 2025.
247. Moy, V.T.; Jiao, Y.; Hillmann, T.; Lehmann, H.; Sano, T. Adhesion Energy of Receptor-Mediated Interaction Measured by Elastic Deformation. *Biophys. J.* **1999**, *76*, 1632–1638. [CrossRef]
248. Ozmaian, A.; Coalson, R.D.; Ozmaian, M. Adsorption of Polymer-Grafted Nanoparticles on Curved Surfaces. *Chemistry* **2021**, *3*, 382–390. [CrossRef]
249. Wang, M.; Mihut, A.M.; Rieloff, E.; Dabkowska, A.P.; Månsson, L.K.; Immink, J.N.; Sparr, E.; Crassous, J.J. Assembling responsive microgels at responsive lipid membranes. *Proc. Natl. Acad. Sci. USA* **2019**, *116*, 5442–5450. [CrossRef]
250. Forg, S.; Karbacher, A.; Ye, Z.; Guo, X.; Von Klitzing, R. Copolymerization Kinetics of Dopamine Methacrylamide during PNIPAM Microgel Synthesis for Increased Adhesive Properties. *Langmuir* **2022**, *38*, 5275–5285. [CrossRef] [PubMed]
251. Sigolaeva, L.V.; Gladyr, S.Y.; Gelissen, A.P.H.; Mergel, O.; Pergushov, D.V.; Kurochkin, I.N.; Plamper, F.A.; Richtering, W. Dual-Stimuli-Sensitive Microgels as a Tool for Stimulated Spongelike Adsorption of Biomaterials for Biosensor Applications. *Biomacromolecules* **2014**, *15*, 3735–3745. [CrossRef] [PubMed]
252. Dasgupta, S.; Auth, T.; Gompper, G. Shape and Orientation Matter for the Cellular Uptake of Nonspherical Particles. *Nano Lett.* **2014**, *14*, 687–693. [CrossRef]
253. Dasgupta, S.; Auth, T.; Gompper, G. Wrapping of ellipsoidal nano-particles by fluid membranes. *Soft Matter* **2013**, *9*, 5473–5482. [CrossRef]

254. Yi, X.; Gao, H. Cell membrane wrapping of a spherical thin elastic shell. *Soft Matter* **2015**, *11*, 1107–1115. [CrossRef]
255. Sorokina, A.S.; Gumerov, R.A.; Noguchi, H.; Potemkin, I.I. Computer Simulations of Responsive Nanogels at Lipid Membrane. *Macromol. Rapid Commun.* **2024**, *45*, 2400406. [CrossRef]
256. Midya, J.; Auth, T.; Gompper, G. Membrane-Mediated Interactions Between Nonspherical Elastic Particles. *ACS Nano* **2023**, *17*, 1935–1945. [CrossRef] [PubMed]
257. Sahu, A.K.; Malik, R.; Midya, J. Wrapping nonspherical vesicles at bio-membranes. *Soft Matter* **2025**, *21*, 4275–4287. [CrossRef] [PubMed]
258. Shen, Z.; Ye, H.; Yi, X.; Li, Y. Membrane Wrapping Efficiency of Elastic Nanoparticles during Endocytosis: Size and Shape Matter. *ACS Nano* **2019**, *13*, 215–228. [CrossRef] [PubMed]
259. Chen, L.; Li, X.; Zhang, Y.; Chen, T.; Xiao, S.; Liang, H. Morphological and mechanical determinants of cellular uptake of deformable nanoparticles. *Nanoscale* **2018**, *10*, 11969–11979. [CrossRef] [PubMed]
260. Shen, Z.; Ye, H.; Li, Y. Understanding receptor-mediated endocytosis of elastic nanoparticles through coarse grained molecular dynamic simulation. *Phys. Chem. Chem. Phys.* **2018**, *20*, 16372–16385. [CrossRef]
261. Yi, X.; Shi, X.; Gao, H. Cellular Uptake of Elastic Nanoparticles. *Phys. Rev. Lett.* **2011**, *107*, 098101. [CrossRef]
262. Hui, Y.; Yi, X.; Wibowo, D.; Yang, G.; Middelberg, A.P.J.; Gao, H.; Zhao, C.X. Nanoparticle elasticity regulates phagocytosis and cancer cell uptake. *Sci. Adv.* **2020**, *6*, eaaz4316. [CrossRef]
263. Bahrami, A.H.; Raatz, M.; Agudo-Canalejo, J.; Michel, R.; Curtis, E.M.; Hall, C.K.; Gradzielski, M.; Lipowsky, R.; Weikl, T.R. Wrapping of nanoparticles by membranes. *Adv. Colloid Interface Sci.* **2014**, *208*, 214–224. [CrossRef]
264. Dasgupta, S.; Auth, T.; Gompper, G. Nano- and microparticles at fluid and biological interfaces. *J. Phys. Condens. Matter* **2017**, *29*, 373003. [CrossRef]
265. Azadbakht, A.; Kraft, D.J. Repulsions and attractions between membrane-deforming spheres, Janus-particles, and opposite tube-like deformations in giant unilamellar vesicles. *Soft Matter* **2025**, *21*, 4730–4738. [CrossRef]
266. Spanke, H.T.; Style, R.W.; François-Martin, C.; Feofilova, M.; Eisentraut, M.; Kress, H.; Agudo-Canalejo, J.; Dufresne, E.R. Wrapping of Microparticles by Floppy Lipid Vesicles. *Phys. Rev. Lett.* **2020**, *125*, 198102. [CrossRef]
267. Van Der Wel, C.; Vahid, A.; Šarić, A.; Idema, T.; Heinrich, D.; Kraft, D.J. Lipid membrane-mediated attraction between curvature inducing objects. *Sci. Rep.* **2016**, *6*, 32825. [CrossRef]
268. Sharma, A.; Zhu, Y.; Spangler, E.J.; Carrillo, J.M.Y.; Laradji, M. Membrane-mediated dimerization of spherocylindrical nanoparticles. *Soft Matter* **2023**, *19*, 1499–1512. [CrossRef]
269. Bahrami, A.H.; Lipowsky, R.; Weikl, T.R. Tubulation and Aggregation of Spherical Nanoparticles Adsorbed on Vesicles. *Phys. Rev. Lett.* **2012**, *109*, 188102. [CrossRef]
270. Šarić, A.; Cacciuto, A. Fluid Membranes Can Drive Linear Aggregation of Adsorbed Spherical Nanoparticles. *Phys. Rev. Lett.* **2012**, *108*, 118101. [CrossRef] [PubMed]
271. Deserno, M.; Bickel, T. Wrapping of a spherical colloid by a fluid membrane. *Europhys. Lett. (EPL)* **2003**, *62*, 767–774. [CrossRef]
272. Deserno, M. Elastic deformation of a fluid membrane upon colloid binding. *Phys. Rev. E* **2004**, *69*, 031903. [CrossRef] [PubMed]
273. Kusumaatmaja, H.; Li, Y.; Dimova, R.; Lipowsky, R. Intrinsic Contact Angle of Aqueous Phases at Membranes and Vesicles. *Phys. Rev. Lett.* **2009**, *103*, 238103. [CrossRef]
274. Li, Y.; Kusumaatmaja, H.; Lipowsky, R.; Dimova, R. Wetting-Induced Budding of Vesicles in Contact with Several Aqueous Phases. *J. Phys. Chem. B* **2012**, *116*, 1819–1823. [CrossRef]
275. Mangiarotti, A.; Chen, N.; Zhao, Z.; Lipowsky, R.; Dimova, R. Wetting and complex remodeling of membranes by biomolecular condensates. *Nat. Commun.* **2023**, *14*, 2809. [CrossRef]
276. Mangiarotti, A.; Sabri, E.; Schmidt, K.V.; Hoffmann, C.; Milovanovic, D.; Lipowsky, R.; Dimova, R. Lipid packing and cholesterol content regulate membrane wetting and remodeling by biomolecular condensates. *Nat. Commun.* **2025**, *16*, 2756. [CrossRef] [PubMed]
277. Lu, T.; Liese, S.; Schoenmakers, L.; Weber, C.A.; Suzuki, H.; Huck, W.T.S.; Spruijt, E. Endocytosis of Coacervates into Liposomes. *J. Am. Chem. Soc.* **2022**, *144*, 13451–13455. [CrossRef]
278. Ferreira, T.; Kulkarni, A.; Bretscher, C.; Richter, K.; Ehrlich, M.; Marchini, A. Oncolytic H-1 Parvovirus Enters Cancer Cells through Clathrin-Mediated Endocytosis. *Viruses* **2020**, *12*, 1199. [CrossRef] [PubMed]
279. Den Otter, W.K.; Briels, W.J. The Generation of Curved Clathrin Coats from Flat Plaques. *Traffic* **2011**, *12*, 1407–1416. [CrossRef]
280. Eisentraut, M.; Sabri, A.; Kress, H. The spatial resolution limit of phagocytosis. *Biophys. J.* **2023**, *122*, 868–879. [CrossRef]
281. Richards, D.; Endres, R. The Mechanism of Phagocytosis: Two Stages of Engulfment. *Biophys. J.* **2014**, *107*, 1542–1553. [CrossRef]
282. Korn, E.D.; Weisman, R.A. Phagocytosis of latex beads by {\it Acanthamoeba}. *J. Cell Biol.* **1967**, *34*, 219–227. [CrossRef] [PubMed]
283. Yildirim, M.; Weiss, A.V.; Schneider, M. The Effect of Elasticity of Gelatin Nanoparticles on the Interaction with Macrophages. *Pharmaceutics* **2023**, *15*, 199. [CrossRef] [PubMed]
284. Jaumouillé, V.; Cartagena-Rivera, A.X.; Waterman, C.M. Coupling of $\beta 2$ integrins to actin by a mechanosensitive molecular clutch drives complement receptor-mediated phagocytosis. *Nat. Cell Biol.* **2019**, *21*, 1357–1369. [CrossRef]

285. Kruger, T.M.; Givens, B.E.; Lansakara, T.I.; Bell, K.J.; Mohapatra, H.; Salem, A.K.; Tivanski, A.V.; Stevens, L.L. Mechanosensitive Endocytosis of High-Stiffness, Submicron Microgels in Macrophage and Hepatocarcinoma Cell Lines. *ACS Appl. Bio Mater.* **2018**, *1*, 1254–1265. [CrossRef]
286. Veltman, D.M.; Williams, T.D.; Bloomfield, G.; Chen, B.C.; Betzig, E.; Insall, R.H.; Kay, R.R. A plasma membrane template for macropinocytic cups. *eLife* **2016**, *5*, e20085. [CrossRef]
287. Palomba, R.; Palange, A.L.; Rizzuti, I.F.; Ferreira, M.; Cervadoro, A.; Barbato, M.G.; Canale, C.; Decuzzi, P. Modulating Phagocytic Cell Sequestration by Tailoring Nanoconstruct Softness. *ACS Nano* **2018**, *12*, 1433–1444. [CrossRef]
288. Lee, J.K.; Guevara, M.; Akanbi, O.D.; Hoff, J.D.; Kupor, D.; Brannon, E.R.; Eniola-Adefeso, O. Deciphering neutrophil dynamics: Enhanced phagocytosis of elastic particles and impact on vascular-targeted carrier performance. *Sci. Adv.* **2025**, *11*, eadp1461. [CrossRef]
289. Gurnani, P.; Sanchez-Cano, C.; Xandri-Monje, H.; Zhang, J.; Ellacott, S.H.; Mansfield, E.D.H.; Hartlieb, M.; Dallmann, R.; Perrier, S. Probing the Effect of Rigidity on the Cellular Uptake of Core-Shell Nanoparticles: Stiffness Effects are Size Dependent. *Small* **2022**, *18*, 2203070. [CrossRef]
290. Anselmo, A.C.; Mitragotri, S. Impact of particle elasticity on particle-based drug delivery systems. *Adv. Drug Deliv. Rev.* **2017**, *108*, 51–67. [CrossRef] [PubMed]
291. Kaksonen, M.; Roux, A. Mechanisms of clathrin-mediated endocytosis. *Nat. Rev. Mol. Cell Biol.* **2018**, *19*, 313–326. [CrossRef]
292. Pelkmans, L.; Helenius, A. Endocytosis Via Caveolae. *Traffic* **2002**, *3*, 311–320. [CrossRef] [PubMed]
293. Mylvaganam, S.; Freeman, S.A.; Grinstein, S. The cytoskeleton in phagocytosis and macropinocytosis. *Curr. Biol.* **2021**, *31*, R619–R632. [CrossRef] [PubMed]
294. Uribe-Querol, E.; Rosales, C. Phagocytosis: Our Current Understanding of a Universal Biological Process. *Front. Immunol.* **2020**, *11*, 1066. [CrossRef]
295. Richards, D.M.; Endres, R.G. How cells engulf: A review of theoretical approaches to phagocytosis. *Rep. Prog. Phys.* **2017**, *80*, 126601. [CrossRef]
296. Palmulli, R.; Machesky, L.M. Is macropinocytosis more than just a passive gulp? *Curr. Opin. Cell Biol.* **2025**, *94*, 102513. [CrossRef]
297. Wu, Y.; Hu, X.; Wei, Z.; Lin, Q. Cellular Regulation of Macropinocytosis. *Int. J. Mol. Sci.* **2024**, *25*, 6963. [CrossRef]
298. Swanson, J.A.; Watts, C. Macropinocytosis. *Trends Cell Biol.* **1995**, *5*, 424–428. [CrossRef]
299. Button, B.; Cai, L.H.; Ehre, C.; Kesimer, M.; Hill, D.B.; Sheehan, J.K.; Boucher, R.C.; Rubinstein, M. A Periciliary Brush Promotes the Lung Health by Separating the Mucus Layer from Airway Epithelia. *Science* **2012**, *337*, 937–941. [CrossRef]
300. Azadi, M.; David, A.E. Enhancing Ocular Drug Delivery: The Effect of Physicochemical Properties of Nanoparticles on the Mechanism of Their Uptake by Human Cornea Epithelial Cells. *ACS Biomater. Sci. Eng.* **2024**, *10*, 429–441. [CrossRef]
301. Ursitti, J.A.; Wade, J.B. Ultrastructure and immunocytochemistry of the isolated human erythrocyte membrane skeleton. *Cell Motil. Cytoskeleton* **1993**, *25*, 30–42. [CrossRef]
302. Klein, I.A.; Boija, A.; Afeyan, L.K.; Hawken, S.W.; Fan, M.; Dall'Agnese, A.; Oksuz, O.; Henninger, J.E.; Shrinivas, K.; Sabari, B.R.; et al. Partitioning of cancer therapeutics in nuclear condensates. *Science* **2020**, *368*, 1386–1392. [CrossRef]
303. Kilgore, H.R.; Mikhael, P.G.; Overholt, K.J.; Boija, A.; Hannett, N.M.; Van Dongen, C.; Lee, T.I.; Chang, Y.T.; Barzilay, R.; Young, R.A. Distinct chemical environments in biomolecular condensates. *Nat. Chem. Biol.* **2024**, *20*, 291–301. [CrossRef]
304. Moeendarbary, E.; Harris, A.R. Cell mechanics: Principles, practices, and prospects. *WIREs Mech. Dis.* **2014**, *6*, 371–388. [CrossRef] [PubMed]
305. Lim, Z.W.; Varma, V.B.; Ramanujan, R.V.; Miserez, A. Magnetically responsive peptide coacervates for dual hyperthermia and chemotherapy treatments of liver cancer. *Acta Biomater.* **2020**, *110*, 221–230. [CrossRef] [PubMed]
306. Liu, J.; Zhorabek, F.; Zhang, T.; Lam, J.W.Y.; Tang, B.Z.; Chau, Y. Multifaceted Cargo Recruitment and Release from Artificial Membraneless Organelles. *Small* **2022**, *18*, 2201721. [CrossRef] [PubMed]
307. Leppert, A.; Feng, J.; Railaite, V.; Bohn Pessatti, T.; Cerrato, C.P.; Mörman, C.; Osterholz, H.; Lane, D.P.; Maia, F.R.N.C.; Linder, M.B.; et al. Controlling Drug Partitioning in Individual Protein Condensates through Laser-Induced Microscale Phase Transitions. *J. Am. Chem. Soc.* **2024**, *146*, 19555–19565. [CrossRef]
308. Patel, A.; Mitrea, D.; Namasivayam, V.; Murcko, M.A.; Wagner, M.; Klein, I.A. Principles and functions of condensate modifying drugs. *Front. Mol. Biosci.* **2022**, *9*, 1007744. [CrossRef]
309. Wang, J.; Abbas, M.; Huang, Y.; Wang, J.; Li, Y. Redox-responsive peptide-based complex coacervates as delivery vehicles with controlled release of proteinous drugs. *Commun. Chem.* **2023**, *6*, 243. [CrossRef] [PubMed]
310. Yoshikawa, M.; Yoshii, T.; Ikuta, M.; Tsukiji, S. Synthetic Protein Condensates That Inducibly Recruit and Release Protein Activity in Living Cells. *J. Am. Chem. Soc.* **2021**, *143*, 6434–6446. [CrossRef]
311. Chatterjee, S.; Kon, E.; Sharma, P.; Peer, D. Endosomal escape: A bottleneck for LNP-mediated therapeutics. *Proc. Natl. Acad. Sci. USA* **2024**, *121*, e2307800120. [CrossRef] [PubMed]
312. Kongkatigumjorn, N.; Smith, S.A.; Chen, M.; Fang, K.; Yang, S.; Gillies, E.R.; Johnston, A.P.R.; Such, G.K. Controlling Endosomal Escape Using pH-Responsive Nanoparticles with Tunable Disassembly. *ACS Appl. Nano Mater.* **2018**, *1*, 3164–3173. [CrossRef]

313. Zhao, F.; Shen, G.; Chen, C.; Xing, R.; Zou, Q.; Ma, G.; Yan, X. Nanoengineering of Stimuli-Responsive Protein-Based Biomimetic Protocells as Versatile Drug Delivery Tools. *Chem. Eur. J.* **2014**, *20*, 6880–6887. [CrossRef]
314. Wang, J.; Hu, L.; Zhang, H.; Fang, Y.; Wang, T.; Wang, H. Intracellular Condensates of Oligopeptide for Targeting Lysosome and Addressing Multiple Drug Resistance of Cancer. *Adv. Mater.* **2022**, *34*, 2104704. [CrossRef] [PubMed]